A Novel Method of Measuring Refractory Black Carbon Mass and Number Distributions by Inversion of CPMA-SP2 Data

by

Kurtis N. Broda

A thesis submitted in partial fulfillment of the requirements for the degree of

Master of Science

Department of Mechanical Engineering
University of Alberta

Abstract

A new method of examining mass and number distributions of nanoscale refractive black carbon (rBC) particles has been developed. This method will be useful for atmospheric scientists conducting semi-continuous measurement of atmospheric rBC. The new method uses a Centrifugal Particle Mass Analyzer (CPMA) and Single Particle Soot Photometer (SP2), coupled with a novel inversion algorithm. The CPMA classifies particles by total mass to charge ratio, and the SP2 measures the mass of rBC in each individual particle. To recover the true rBC and total particle mass and number distributions, an inversion is required which accounts for multiple charging of particles and the CPMA transfer function. The inversion solves an inverse problem characterized by a Fredholm integral equation, where the true number and mass distribution of the aerosol is unknown, however both the system response and mathematical model of the CPMA-SP2 system are known. The inverse problem was solved using iterative methods, and a two variable number distribution was used to represent number concentration as a function of both rBC and total particle mass. The inversion was tested and validated using laboratory experiments, where the CPMA-SP2 sampled from a smog chamber. Sampling populations of uncoated, coated, and mixed coated-uncoated rBC particle populations was conducted. Finally the inversion was tested on data gathered in the real world during a field campaign in Shanghai, China. The results for three cases of high, medium, and low pollution levels, showed distinct populations of rBC particles, which are a function of rBC released from different sources and having different atmospheric residence times. The real world results showed this method can give valuable insights for atmospheric scientists using semi-continuous data logging. Future work will involve packing the software into a convenient form for use by CPMA-SP2 users.

Preface

Chapter 1 and 4 are my original work, while Chapter 2 and 3 involved two separate collaborations. In Chapter 2, I assisted in experimental design and construction, and gathered data, while Dr. Gregory Schill processed the raw SP2 waveform data. Additionally: Dr. Jason Olfert assisted with experimental design, theory, and manuscript edits; Dr. Martin Irwin assisted with experiments and manuscript edits; Elijah Schnitzler assisted with experiments; Dr. Gavin McMeeking with experimental design and troubleshooting; and Dr. Wolfgang Jäger provided laboratory space. I conducted data processing, analysis, and writing. A similar version of chapter two will be submitted to the Journal of Aerosol Science and Technology with the persons listed above as co-authors.

Data shown in Chapter 3 was gathered by the University of Manchester, lead by Dr. James Allan. The raw SP2 waveform data was analyzed by Dantong Liu and Rutambhara Joshi. I conducted all subsequent analysis and writing, and Dr. Olfert provided manuscript edits.

For Vera Kobylka, in memoriam

Acknowledgements

Firstly, I would like to thank Jason for introducing me to the fields of aerosol science and data inversion, and with providing me with a fascinating research project. I am very grateful for the opportunity Jason provided for my travels to Cambridge, and his sincere desire to help his students. I always looked forward to our weekly meetings, where we discussed important topics such as biking, and sometimes even aerosol science. His advice and mentoring throughout the past two years was invaluable.

Thank you to Cambustion, especially Dr. Jonathan Symonds and Dr. Martin Irwin, for their support while I was in Cambridge. Additionally I would like to thank everyone in Dr. Olferts research group at the University of Alberta for their contributions and assistance.

Finally, thank you to all my friends and family for their encouragement and support. I would especially like to thank my parents, Norbert and Karen Broda, and my grandfather, Norman Kobylka, for their love and support. I would also like to thank my girlfriend, Dallas Tkachuk for her encouragement.

Table of Contents

List of Figures

Nomenclature

Acronyms

AMS	Aerosol Mass Spectrometer
APD	Avalanche Photo Diode
APM	Aerosol Particle Mass Analyzer
BBHG	Broad Band High Gain
BBLG	Broad Band Low Gain
BC	Black Carbon
CCN	Cloud Condensation Nuclei
CPC	Condensation Particle Counter
CPMA	Centrifugal Particle Mass Analyser
DMA	Differential Mobility Analyser
EC	Elemental Carbon
FWHM	Full Width Half Maximum
GDI	Gasoline Direct Injection
HPDI	High Pressure Direct Injection
JE	Jet Engine
LII	Laser Induced Incandescence
Nd:YAG	neodymium-doped yttrium aluminium garnet; Nd:$Y_3Al_5O_{12}$
PM	Particulate Matter
$PM_{2.5}$	Particulate Matter less than 2.5 microns in diameter

PM_{10}	Particulate Matter less than 10 microns in diameter
rBC	Refractive Black Carbon
SOA	Secondary Organic Aerosol
SMPS	Scanning Mobility Particle Sizer
SP2	Single Particle Soot Photometer
SP-AMS	Soot Particle-Aerosol Mass Spectrometer
TEM	Transmission Electron Microscopy
VOC	Volatile Organic Compound
WHO	World Health Organization

Symbols

a	ratio of measured number concentration to newest iteration
a_p	Aerosol Species
A_p	Total number of distinct aerosol species
A_c	Fraction of Earth's surface covered by clouds
B	Mechanical mobility
β	Inverse of CPMA resolution
$\hat{\beta}$	Analytical solution to integral of triangular CPMA transfer function at i^{th} setpoint
β_u	Upscatter fraction
χ	Mixing state index
χ_t	Shape factor
C_c	Cunningham slip correction factor
D_j	mobility diameter selected using a DMA
d_{p}^*	Selected mobility diameter (setpoint) on DMA
d_{p}	Mobility equivalent diameter
d_{rBC}	Volume equivelent diameter of a refractive black carbon particle
d_{ve}	Volume equivalent diameter
$\frac{\mathrm{d}M}{\mathrm{d}\log d_{\mathrm{p}}}$	Mass concentration distribution as a function of particle mobility diameter
$\frac{\mathrm{d}M}{\mathrm{d}\log m_{\mathrm{p}}}$	Total mass concentration distribution as a function of particle refractive black carbon mass
$\frac{\mathrm{d}M}{\mathrm{d}\log m_{\mathrm{rBC}}}$	Total mass concentration distribution as a function of particle refractive black carbon mass
$\frac{\mathrm{d}M_{\mathrm{rBC}}}{\mathrm{d}\log m_{\mathrm{rBC}}}$	Refractive black carbon mass concentration distribution as a function of particle refractive black carbon mass

$\frac{\mathrm{d}M_{\mathrm{rBC}}}{\mathrm{d}\log m_{\mathrm{p}}}$	Refractive black carbon mass concentration distribution as a function of total particle mass
$\frac{\mathrm{d}N}{\mathrm{d}\log d_{\mathrm{p}}}$	Number concentration distribution as a function of particle mobility diameter
$\frac{\mathrm{d}N}{\mathrm{d}\log m_{\mathrm{p}}}$	Number concentration distribution as a function of total particle mass
$\left[\frac{\mathrm{d}N}{\mathrm{d}\ln m_{\mathrm{p}}}\right]^{*}$	Number concentration distribution as a function of total particle mass at the CPMA setpoint
$\frac{\mathrm{d}N}{\mathrm{d}\log m_{\mathrm{rBC}}}$	Number concentration distribution as a function of particle refractive black carbon mass
$\frac{\mathrm{d}N_{\mathrm{nv}}}{\mathrm{d}\log d_{\mathrm{p}}}$	Number concentration distribution of non-volatile material as a function of mobility diameter
$\frac{\mathrm{d}N_{\mathrm{pv}}}{\mathrm{d}\log d_{\mathrm{p}}}$	Number concentration distribution of purely volatile material as a function of mobility diameter
$\frac{\mathrm{d}N_{\mathrm{Response}}}{\mathrm{d}\log m_{\mathrm{rBC}}}$	Number concentration distribution measured by CPMA-SP2 as a function of particle refractive black carbon mass
$\frac{\partial^2 N}{\partial\log m_{\mathrm{p}}\partial\log d_{\mathrm{p}}}$	Two variable number concentration distribution as a function of total particle mass and mobility diameter
$\frac{\partial^2 N}{\partial\log m_{\mathrm{p}}\partial\log m_{\mathrm{rBC}}}$	Two variable number concentration distribution as a function of total particle mass and refractive black carbon mass
$\frac{\partial^2 N_{\mathrm{guess}}}{\partial\log m_{\mathrm{p}}\partial\log m_{\mathrm{rBC}}}\Big\vert_{i}$	Initial guess for the i$^{\mathrm{th}}$ CPMA setpoint
D_{α}	Average per particle diversity
D_{γ}	Bulk particle diversity
D_i	Particle diversity of the i^{th}*particle*
ΔF	Change in outgoing radiative flux of Earth
$\Delta\Phi$	a finite increment in electric flux

ϵ	Correction factor
$\bar{\epsilon}$	Average Correction factor
ϵ^*	Correction factor at CPMA setpoint
$\bar{\eta}$	average percent of particles lost at j^{th} instrument setpoint
$\bar{f}$	bin average of charge fraction
f^*	Charge fraction evaluated at CPMA setpoint
f_a	Fraction of light absorbed by an atmospheric aerosol layer
f_d	Fraction of light scattered downwards by an atmospheric aerosol layer
f_{down}	Total downward transmitted fraction
f_u	Fraction of light reflected upwards by an atmospheric aerosol layer
f_t	Fraction of light transmitted by an atmospheric aerosol layer
f_{vm}	volatile mass fraction
f_{vp}	volatile particle fraction
F_o	Incoming solar flux
Γ	Kernel function, as described by Fredholm theory
$\mathbf{\Gamma}$	Kernel of a system for the entire range of instrument setpoints
i	Instrument setpoint
j	The geometric midpoint of the j^{th} bin
k	Iteration count for Twomey loop
L	distance between DMA aerosol entrance and sampling entrance
λ	Ratio of DMA flows
m_{p}	Total particle mass
m_{p}^*	CPMA setpoint

$\tilde{m}_{\mathrm{p}}$	Ratio of particle mass to CPMA setpoint mass
$m_{\mathrm{p}_{j\pm1/2}}$	edges of the j$^{\mathrm{th}}$ bin of rBC masses
m_{rBC}	Refractive black carbon mass
M	Total mass concentration
M_{rBC}	Refractive black carbon mass concentration
μ	Viscosity
N	Number concentration
N_p	Number of aerosol particles
N_{SP2}	Number concentration measured by directly measuring using the single particle soot photometer
N^*	Number concentration at the CPMA setpoint
ω	Single scattering albedo
ω_{crit}	Critical albedo
Ω	Transfer function
$\bar{\Omega}$	bin average of transfer function
p	unknown quantity to be determined, as described by Fredholm theory
p_a	Mass fraction of a species in the population
p_i	Mass fraction of the i^{th} particle
Φ	Number of charge states
q_{a}	Aerosol flow rate through DMA
q_{m}	main oulet flow rate
q_{s}	sampling flowrate through DMA
$\mathbf{Q}$	Unknown particle distribution
r_a	radius of the DMA's charged center rod
r_b	inner radius of DMA casing

R	Response of a system, as described by Fredholm theory
R_m	CPMA resolution
R_s	Albedo of Earth's surface
t_{c}	Time counting particles using a DMA
T_a	Fractional atmospheric transmittance
τ	Optical depth
V	Voltage difference
Z	Electrical mobility
Z_{p}	Electrical Mobility of a single particle
Z_{p}^*	Mobility evaluated at d_{p}^*

Chapter 1

Introduction

1.1 Refractive Black Carbon

The battle for clean air in cities is not a new one, in 1952 London experienced "the Great Smog," where the air was filled with toxic pollutants released from coal combustion. It is estimated the thick, sulfuric "pea-soup" mixture which choked the city over the period of 4 days resulted in about 12,000 deaths and many more people becoming ill. The great smog resulted in a public and governmental push to reduce pollutants so such an event would not repeat itself (Davis, 2002). Recently, air pollution, especially resulting from combustion of fossil fuels, has been shown to be a significant contributor to climate change and increased human morbidity (Pachauri et al., 2015). One of the most egregious culprits of climate change is black carbon (BC), a carbonaceous aerosol. Significant scientific efforts have been made to understand the structure, life-cycle, and properties of BC. Understanding and mitigating BC emissions is an important step to increasing air quality and reducing harmful effects of rBC on humans and the environment (Pachauri et al., 2015).

A definition of Black carbon was given by Petzold et al. (2013) and Bond et al. (2013), namely it is i) strongly absorbing in the visible light spectrum, ii) refractory, meaning the vaporization temperature is relatively high, iii) insoluble in water and

the organic solvents which may be present in atmospheric aerosol, iv) an aggregate of spheroidal primary particles between 10 and 50 nm in diameter, and v) is mostly comprised of sp^2 bonded carbon atoms. An additional term for a material similar to BC which is used in this thesis is refractive black carbon (rBC). Specifically, this term will be used when discussing measurement of aerosol with a single particle soot photometer (SP2) (Stephens et al., 2003). The term rBC is specific to SP2 measurement, and is defined as an insoluable carbonaceous aerosol with a vaporization temperature around 4000K (Schwarz et al., 2010). There is no consensus as to whether BC is totally equivalent to rBC, technically rBC is a subset of BC. However the definitions are nearly identical, therefore it is likely that most BC is also rBC (Andreae and Gelencsér, 2006).

It is important to distinguish rBC and BC from other working definitions of carbon byproducts of combustion. An analogous term for BC is soot (Pachauri et al., 2015), however this term refers to any dark product of combustion composed at least partly of carbon, which may or may not be strongly light absorbing. Therefore, rBC and BC is a subset of soot, and not all soot is of concern to climate scientists. Some governmental and supra-national organizations such as the World Health Organization (WHO) or European Environmental agency use the term black carbon (BC) to mean any particulate matter (PM) composed of char, soot, black carbon, or elemental carbon. This difference is regrettable, since it is often confusing as to what substance exactly BC is referring to. Another classification of carbon particles is elemental carbon (EC), which is defined as pure carbon formed by crystals 2-3 nm in diameter, with several carbon graphite-like layers (Petzold et al., 2013; Seinfeld and Pandis, 2016). The term light absorbing carbon was suggested by Bond and Bergstrom (2006), and is operationally identical to the definition given for rBC. However, the term light absorbing carbon never gained wide acceptance, and the usage of rBC is preferred, which was recommended by the same author in her later work (Bond et al., 2013).

Additionally, other compositions of carbonaceous particles exist that are not relevant to atmospheric scientists, but have aided understanding of BC's properties, such as Carbon Black, Amorphous Carbon, Coal, Graphite, and Tar (Bond and Bergstrom, 2006).

Emissions of rBC particles may be anthropogenic (*i.e.* originating from human activity) or non-anthropogenic. Significant anthropogenic sources include diesel engines (Maricq, 2007), coal fired power plants, biofuel cooking, and human caused vegetation fires (Bond et al., 2013). Figure 1.11a shows Global BC emission apportionment by source of emission. The error bars are large on the estimates of BC emissions, probably because it is difficult to quantify BC emissions from wildfires and residential solid fuel use. As seen in Figure 1.11b, global BC emissions can also be analyzed on a geographic basis, with emission source represented by colored bars. From these plots we can see in North America and Europe, diesel engines make up approximately half of the 380 and 470 Gigagrams per year of rBC emissions respectively (Bond et al., 2013). If society is to seriously curb the emission of rBC particles, emission reduction or reduction in use of diesel engines should be a focus area.

When released from a combustion source, BC is generally observed as fractal-like aggregates of primary particles (Dastanpour and Rogak, 2014). Figure 1.2 shows transmission electron microscopy (TEM) images of BC collected from four combustion sources, a gasoline direct injection car engine (GDI), high pressure direct natural gas injection car engine (HPDI), an aviation gas turbine (JE), and a laminar inverted burner, where the scale bar represents 100 nm. Looking closely at the TEM images, the primary particles can be distinguished, and they can range from 10 nm in diameter to over 50 nm, with diameter being defined as the average of two measurements across the approximately spheroidal primary particles. The shape of BC aggregates can be defined by the fractal dimension, which value is a measure of the complexity of the shape (Hinds, 1999). A fractal dimension of 1 would be a perfectly straight line, and a

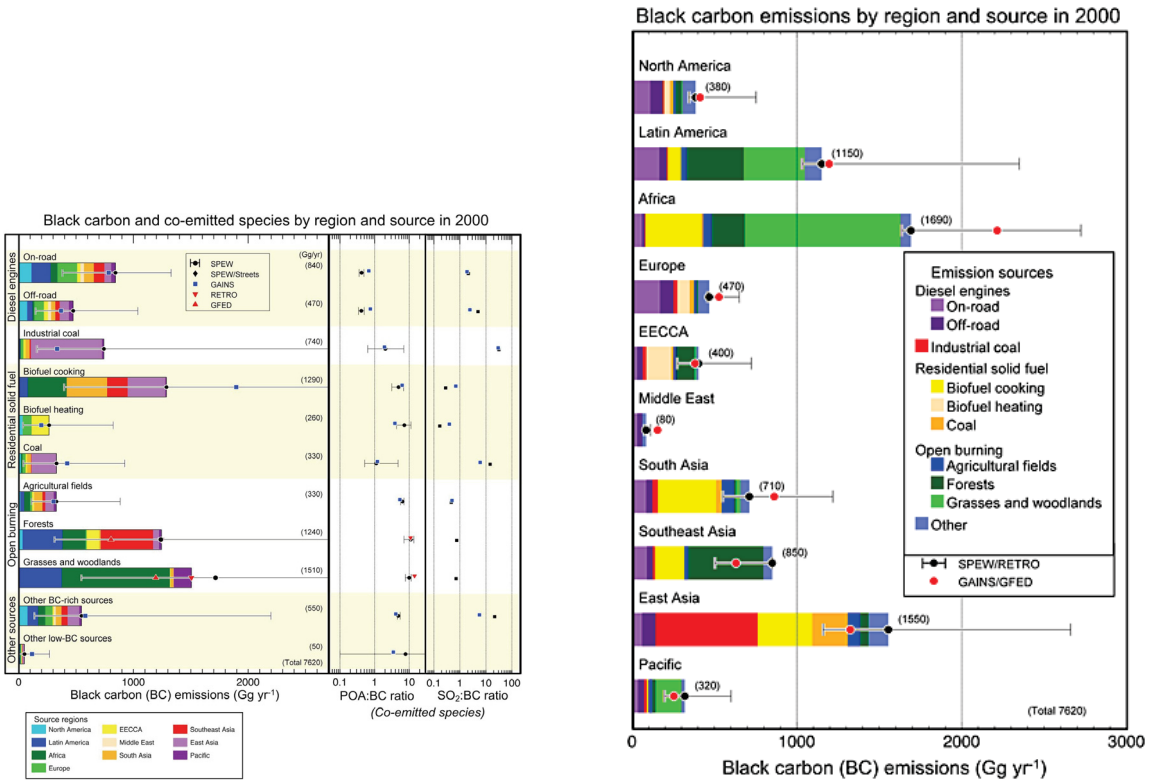

Figure 1.1: Two ways of quantifying where BC emissions come from are: a) BC emitted by source, and, b) BC emitted by region (Bond et al., 2013).

fractal dimension of 3 would indicate a sphere. A fractal-like BC particle is expected to have a value near 2 (Sorensen, 2011).

1.2 Coating of BC particles with secondary organic aerosol

Refractive BC is generally observed as coated with non-BC material, and a visualization of the coating process is shown in Figure 1.3. The BC particles acquire a coating of non-BC material either at the source of emission, in the atmosphere from coagulation with secondary organic aerosol, or from condensation reactions (Riemer et al., 2004; Schnaiter et al., 2005; Moosmüller et al., 2009). At the source, the acquisition of coating is from organic material (*e.g.* unburned engine oil) and other byproducts of combustion (*e.g.* sulphuric acid (Maricq, 2007)). The BC particles can be fur-

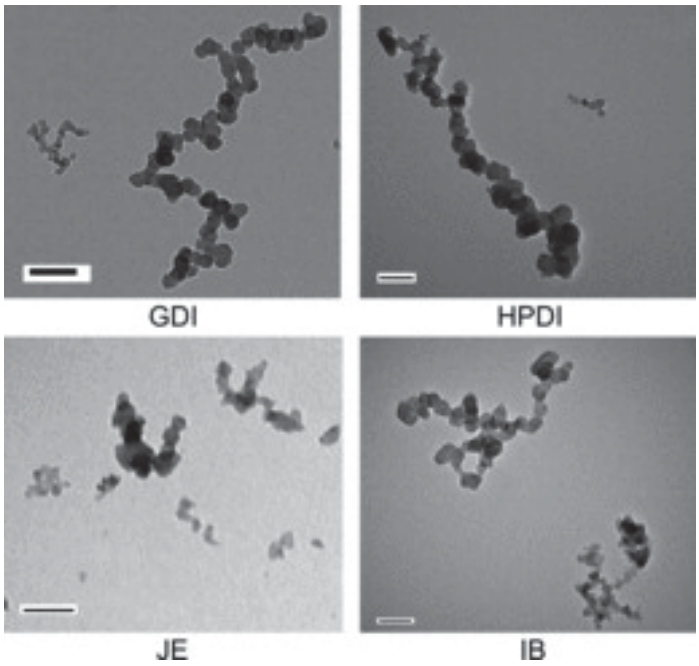

Figure 1.2: TEM images of BC emitted from four different combustion sources (Dastanpour and Rogak, 2014)

ther coated in the atmosphere by coagulation of secondary organic aerosols (SOA's), which are formed by photo-oxidation reactions of volatile organic compounds. Alternatively, these products of photo-oxidation could directly condense onto BC particles instead of forming SOA's. After residing in the atmosphere the fractal morphology collapses into a more spherical shape, and after several days in the atmosphere coated BC particles are near-spherical (Schnitzler et al., 2014; Gustafsson and Ramanathan, 2016).

Secondary organic aerosols are produced in the atmosphere via a complex interaction of light, volatile organic compounds (VOC's), and radicals. The aerosols are "secondary" because they are not released directly from a source, but form in the atmosphere. The raw material for secondary organic material is provided by VOC's which are released from a variety of sources both natural and anthropogenic, and combustion sources produce approximately 13% of the yearly total (Hallquist et al., 2009). The two main atmospheric oxidants are the hydroxyl radical (OH), ozone (O_3), and

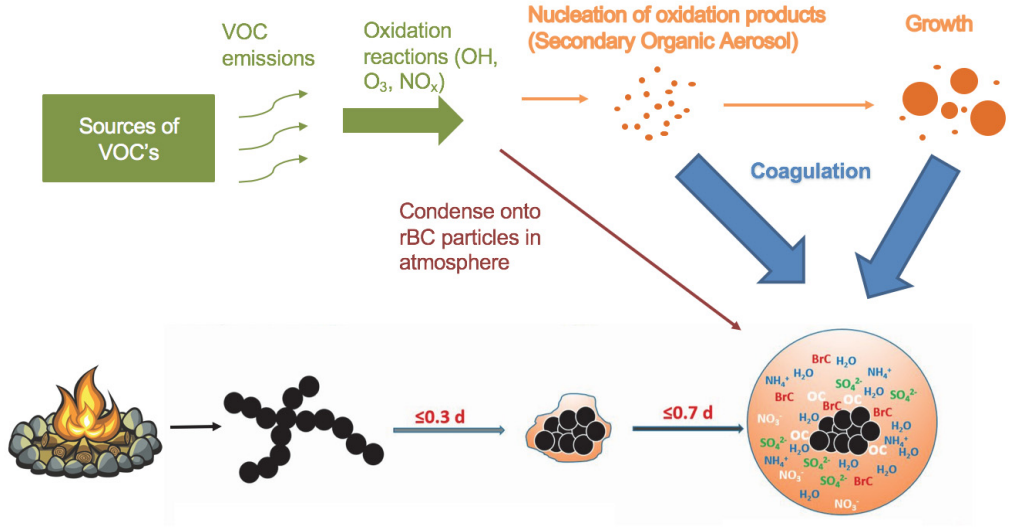

Figure 1.3: A visual representation of how BC can acquire coating, adapted from Gustafsson and Ramanathan (2016)

the nitrate radical (NO_3). Oxidation of an organic molecule yields functional groups, for example, hydroxyl (–OH), carbonyl (–C=O), or nitrooxy ($–ONO_2$). These functional groups then can form low vapour pressure products which are less volatile than their reactants, which tend to condense onto existing particulate mater (Seinfeld and Pandis, 2016). Alternatively, the products could nucleate, however, thermodynamically, the compounds are more likely to condense onto particulate matter if it exists. The secondary organic aerosol then may further coagulate with coated or uncoated BC particles which increases their coating thickness.

1.3 Motivation

Refractive black carbon can have negative effects on the atmosphere and human health. It is known to contribute to climate change and to negatively affect cardiovascular health in humans (World Health Organization, 2012; Pachauri et al., 2015).

1.3.1 Effect of Aerosol on Climate change

The observed mean surface temperature of the earth has increased by 0.85 K (0.65 to 1.06 with a 90% confidence interval) between 1880 and 2010 (Pachauri et al., 2015). The latest Intergovernmental Panel on Climate Change reaffirmed it is extremely likely (95–100% confidence) the majority of this warming is due to human caused effects (Pachauri et al., 2015). Furthermore, it is extremely likely at least half of the observed warming between 1951–2010 of approximately 0.65 K is human caused. This warming effect due to human activity is referred to as either climate change or global warming. The net warming of Earth has caused increased frequency of extreme weather events, decreased quality and quantity of freshwater, and additional negative impacts on natural and human systems. It is expected these negative effects to increase in magnitude and frequency with further global mean surface temperature increase (Pachauri et al., 2015). The key driver of human caused climate change is from the combined effects of increased concentrations of greenhouse gases, along with other anthropogenic sources. One very significant contributor to climate change is aerosols from anthropogenic sources (Pachauri et al., 2015).

Aerosols affects climate through "indirect" and "direct" effects. The effect of a substance on climate change is characterized by its "radiative forcing," which is defined as the area normalized net downward difference in irradiance in Earth's energy balance due to the presence of a substance (Seinfeld and Pandis, 2016). The main indirect effect of aerosols is a change in cloud density and lifecycle. Particles can act as cloud concentration nuclei (CCN), where particles entering a cloud act as nucleation sites. Under some conditions, CCN entering a cloud results in more numerous water droplets with a smaller mean diameter (Seinfeld and Pandis, 2016). More droplets increases the surface area of the cloud, which causes more incoming solar radiation to be reflected back into the atmosphere (Dusek et al., 2006). Thus, the indirect effects

of some aerosol is generally a negative radiative forcing (*i.e.* a net global cooling effect) (Seinfeld and Pandis, 2016).

Direct effects of aerosols involve particles absorbing and scattering solar radiation. Whether a particle absorbs or scatters light is a function of its material properties, characterized by its refractive index. The refractive index is a measure of the absorbing and scattering components of a material relative to the surrounding medium. However, it is often more convenient to characterize materials based on single scattering albedo, ω, which is dependent on refractive index (Seinfeld and Pandis, 2016). Single scattering albedo is the ratio of the scattering efficiency to extinction efficiency. The single scattering albedo has a range of 0–1, where material with $\omega = 0$ would absorb all incoming light, and a material with $\omega = 1$ would scatter all incoming light. Many aerosols have single scattering albedo close to 1, such as water, salt, and organics (Seinfeld and Pandis, 2016). Material with a single scattering albedo of 0 do not exist, however, aerosols such as BC have an albedo less than 1 and therefore both scatter and absorb light. The direct effect of an aerosol layer in the atmosphere can be demonstrated by a simple model. For an aersool layer, the fraction of light reflected upward, f_u, absorbed, f_a, scattered downwards, f_d, and transmitted, f_t, can be shown to be a function of optical depth, τ, and upscatter fraction β_u (Seinfeld and Pandis, 2016),

$$f_u = (1 - e^{-\tau})\omega\beta_u, \tag{1.1}$$

$$f_a = (1 - \omega)(1 - e^{-\tau}), \tag{1.2}$$

$$f_d = \omega(1 - \beta_u)(1 - e^{-\tau}), \tag{1.3}$$

$$f_t = e^{-\tau}. \tag{1.4}$$

Therefore, the total downward transmitted fraction is,

$$f_{down} = e^{-\tau} + \omega(1 - \beta_u)(1 - e^{-\tau}) \tag{1.5}$$

The light transmitted and scattered downward will be absorbed or reflected by the earth. Therefore, the equations can again be written for light coming from the opposite direction. Considering this effect, and effects of cloud cover, the change in outgoing radiative flux due to an atmoshperic aerosol layer can be shown to be Seinfeld and Pandis (2016),

$$\Delta F = F_o(1 - A_c)T_a^2 \left[\left(f_u + \frac{f_{down}^2 R_s}{1 - R_s f_u} \right) - R_s \right], \tag{1.6}$$

where F_o is incoming solar flux, A_c is the fraction of Earth's surface covered by clouds, T_a is the fractional atmospheric transmittance, and R_s is the average albedo of Earth's surface. Thus, this equation can demonstrate that the primary parameter which determines if an aerosol causes a positive or negative forcing effect is its single scattering albedo (Seinfeld and Pandis, 2016). Setting this equation to $\Delta F = 0$, the critical albedo, ω_{crit}, can be solved for, where $\omega > \omega_{\text{crit}}$ results in global cooling and $\omega < \omega_{\text{crit}}$ results in global warming. Assuming approximate global values of $\tau << 1$, $R_s = 0.15$, $\beta_u = 0.29$, the critical albedo is approximately 0.6 (Seinfeld and Pandis, 2016). However, when average surface albedo approches 1, such as over a flat and snowy area, the critical albedo approaches 1 Seinfeld and Pandis (2016).

Aerosol direct effects are further complicated when particles are a mixture of species. For example, a BC particle coated with organic material will have unique scattering and absorption behavior (Cappa et al., 2012). For example, in Figure 1.4, the albedo of an ammonium sulfate and BC mixture is a non-linear function of mass composition, especially for an internal mixture. The degree of mixing can be

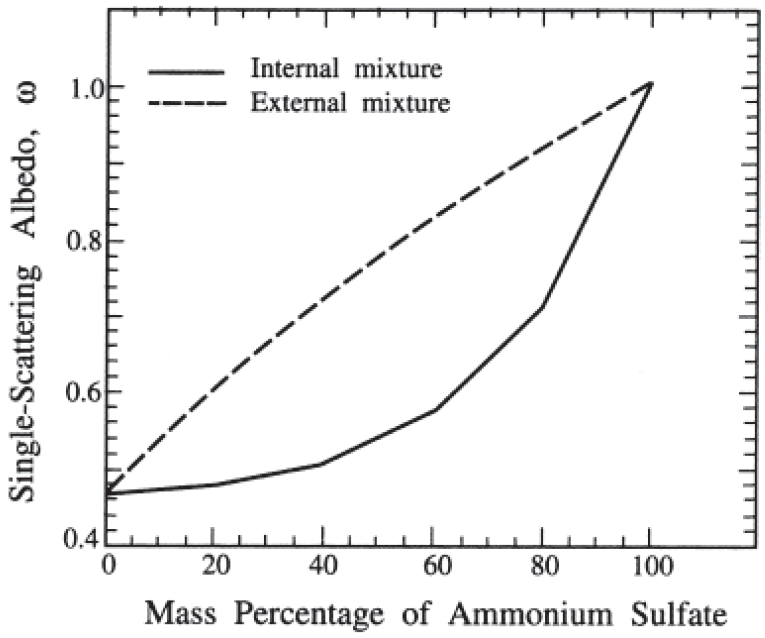

Figure 1.4: Single scattering albedo for internal and external mixtures of $(NH_4)_2SO_4$ and BC as a function of mass percentage (Seinfeld and Pandis, 2016).

characterized by the mixing state, formally defined by Riemer and West (2013). A particle population is said to be fully externally mixed when all particles are pure, and fully internally mixed when every particle in a population has identical mass fractions of constituent components in the population. With atmospheric BC a fully externally mixed population would consist of pure BC particles with no organic coating. A fully internally mixed population would consist of BC particles with organic coating, and each particle had identical mass fractions of BC and organic coating (Riemer and West, 2013).

1.3.2 Effect of Black Carbon on Climate Change

As discussed in Section 1.3.1, aerosols have an important role in Climate Change. A significant aerosol with large climate change effects is BC, it is likely the second most influential anthropogenic climate changing compound behind carbon dioxide (Bond et al., 2013). A recent estimate of direct radiative forcing of atmospheric BC in

the industrial era is +0.71 W m^{-2}, with a 90% confidence interval of $(+0.08, +1.27)$ W m^{-2}. If indirect effects such as cloud lifecycle changes are included in the radiative forcing estimate, the forcing value increases to +1.1 W m^{-2} with a 90% confidence interval of $(+0.17, +2.1)$ W m^{-2}. (Bond et al., 2013). Thus it is likely that BC has a significant global warming effect, second only to carbon dioxide. However the theoretical error of the radiative forcing estimate for BC is relatively high at 90%. This is mostly due to uncertainties induced by the acquisition of coatings.

The mixing state of BC with organic components can greatly affect its radiative forcing value, and internal mixing with organic material probably increases radiative forcing by up to a factor of 2 (Jacobson, 2001; Schnaiter et al., 2005; Moosmüller et al., 2009; Lack and Cappa, 2010; Cappa et al., 2012). This is due to direct and indirect effects. Direct effects can be attributed to "lensing" of internally mixed BC particles (Bond and Bergstrom, 2006). The lensing effect refers to when light is refracted when progressing to a medium of a different density, in this case the organic coating surrounding BC. Because the light progresses from a medium of lower density to a medium of higher density, it is refracted towards the interior of the particle (Young and Freedman, 2008), in this case occupied by an absorbing BC core. Therefore, due to lensing, the BC absorbs a greater quantity of radiation than if it was uncoated (Bond and Bergstrom, 2006). Indirect effects of BC mixing state involves change in cloud life-cycle (McMeeking et al., 2011). The acquisitions of coatings tends to reduce cloud life-cycle time, and, because clouds have a net cooling effect, this causes an additional increase in radiative forcing (Koch and Del Genio, 2010).

1.3.3 Human health

Developing causal relationships between BC and effects on human health is challenging for two main reasons. Firstly, other air pollutants are often present besides BC, and secondly, there is high variation in concentration across space and time,

especially within cities (World Health Organization, 2012). For example, the concentration of BC is higher near roads, and depends on traffic volume which is a function of time (*i.e.* around rush hour has higher BC concentrations than the middle of the night) (Henderson et al., 2007). Some negative health effects attributed to BC may be partly because of other PM, especially that which is less than 2.5 microns in diameter ($PM_{2.5}$) in the atmosphere (World Health Organization, 2012). Determining health effects of BC is still an active area of research, however it is likely that BC exposure does cause negative outcomes to humans health (World Health Organization, 2012).

Evidence of negative human health effects is provided by toxicological studies of short term BC exposure and statistics based epidemiological results. The first methodology, toxicological studies, generally exposed people to BC particle concentrations between 100-350 μg m^{-3} for up to two hours (Gong Jr et al., 2003; Solomon et al., 2003; Mills et al., 2005, 2008; Riddervold et al., 2011; World Health Organization, 2012). The source of the BC was diesel engines, and ethical concerns limited the test population to healthy individuals or people with mild asthma. Most studies conducted have not made a distinction between BC, EC and PM. (Gong Jr et al., 2003; Solomon et al., 2003; Mills et al., 2005, 2008; Riddervold et al., 2011; World Health Organization, 2012). However some work has showed that pure BC does not produce short-term negative vascular or cardiovascular effects, and it is potentially the non-BC coating which causes toxicity (Frampton et al., 2006; Mills et al., 2011; Biswas et al., 2009; World Health Organization, 2012).

The second methodology, epidemiological studies, focuses on statistical methods of parsing the effect of BC from other PM. Since BC tends to vary spatially, health outcomes of populations living near BC sources (and thus the PM is comprised of a high proportion of BC) can be compared to populations exposed to PM with low concentrations of BC. These studies are effective where data is available, however expensive equipment, difficult calibration, and restrictions on access to medical records

due to medical privacy laws are limiting (World Health Organization, 2012). Overall, it is accepted that BC is a health-relevant component of PM, and morbidity is a function of PM exposure and duration (Janssen et al., 2011). It has been estimated a 10 μg m^{-3} increase in BC concentration results in a more significant increase in cardiovascular morbidity and general mortality than a similar concentration increase in PM_{10}, and perhaps the same for $PM_{2.5}$ (Cakmak et al., 2009b,a; World Health Organization, 2012). Ranking the relative impact of BC relative to other known harmful PM components such as metals or sulfates is challenging, however BC is likely one of the most harmful (World Health Organization, 2012). It is clear that BC has negative effects on human health, however a big question which requires further research is if the magnitude of BC health effects is altered due to non-BC coating acquisition (World Health Organization, 2012).

1.4 Description of selected aerosol science instrumentation

The study of the physical characteristics of BC and its effects on climate and human health is reliant on instrumentation. Three aerosol science instruments are frequently referenced in this thesis and are therefore described in this section, namely the: Single Particle Soot Photometer (SP2), Differential Mobility Analyzer (DMA), and the Centrifugal Particle Mass Analyzer (CPMA).

1.4.1 Single particle soot photometer

A detailed description of the SP2 can be found in Stephens et al. (2003), and is summarized here. The SP2 measures two quantities, the rBC particle mass via Laser Induced Incandescence (LII) and the optical scattering diameter via light scattering. As seen in the SP2 schematic shown in Figure 1.5, the nozzle directs rBC particles through a Nd:YAG (neodymium-doped yttrium aluminium garnet; Nd:$Y_3Al_5O_{12}$) intra-cavity

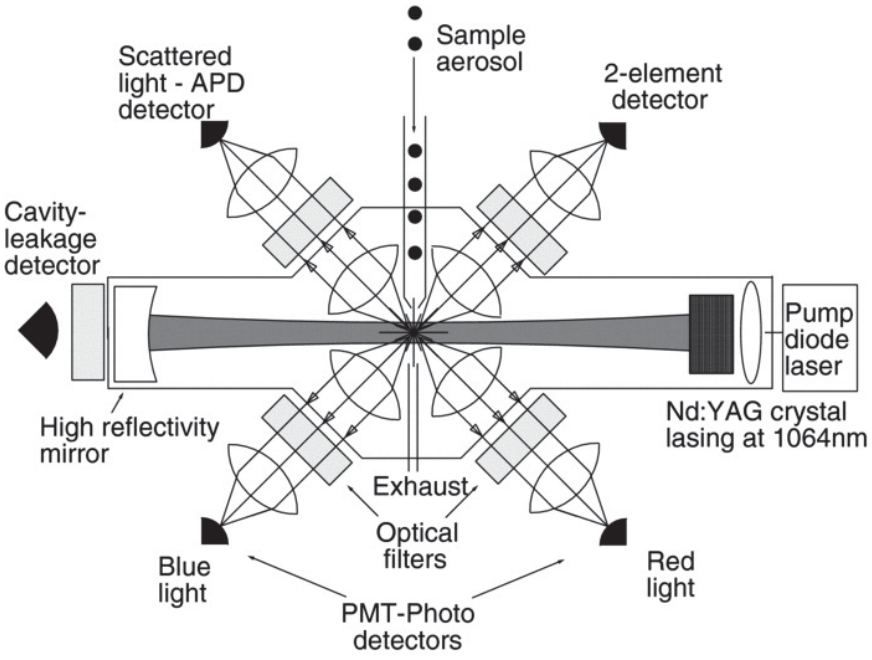

Figure 1.5: Schematic of the SP2 (Moteki and Kondo, 2007).

laser beam, with a wavelength of 1064 nm. Light scattered and incandescent from the particles is measured by avalanche photodiodes (APD's), which converts light to electricity using the photoelectric effect. A compound lens assembly directs light to a single APD to form a detection "channel." There are four channels, one for scattered light with a wavelength of 1064 nm and three incandescence channels. Two incandescence channels measure light with a wavelength at 300-800 nm, and one measures infared light with a wavelength of 1400-1700 nm. The mirror is reflective, and has a leakage transmission of 15 ppm, which allows measurement of intracavity power.

When the particles enter the laser cavity, some of the laser light is absorbed by the particles, which increases their temperature inducing vaporization of their coating, and some of the light is scattered. The increase in temperature causes the rBC core to emit blackbody radiation. This scattered and incandescent radiation is measured by photo-diodes, and the peak of the blackbody radiation signal (or sometimes referred to as the LII signal) is correlated to the rBC mass of a particle on

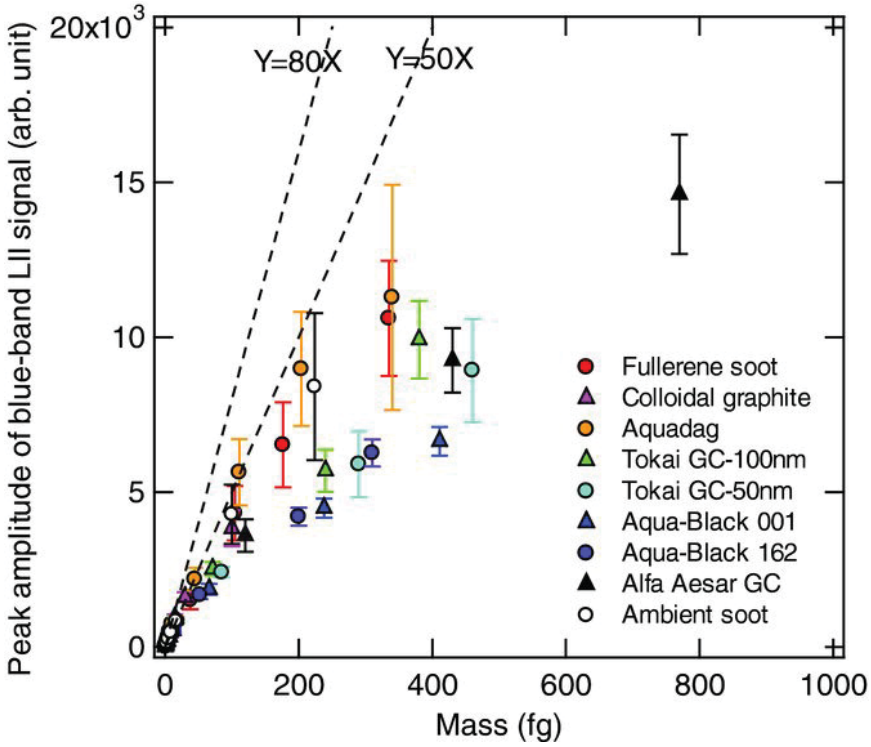

Figure 1.6: LII signal as a function of rBC particle mass (Moteki and Kondo, 2010).

a particle by particle basis (Stephens et al., 2003). The correlation is conducted based on information obtained during calibration of LII amplitude to particles of a known rBC mass. As seen in Figure 1.6, the maximum peak amplitude of the LII signal for ambient rBC has a linear relationship up to approximately 75 fg (Moteki and Kondo, 2010). Importantly, the LII response for rBC closely agrees with various common calibration aerosols for the linear region, and it is along this region where valid results can be obtained. For calibration, a monodisperse in mass aerosol is required, or a mobility monodisperse aerosol with a known mass-mobility relationship.

Laboratory tests have shown a coated internally mixed rBC particle will have the same LII–rBC mass relationship as an uncoated rBC particle (Moteki and Kondo, 2007). This indicates the particles will still vaporize under a relatively thick coating before exiting the laser cavity. In Figure 1.7, a monodisperse aerosol with a spherical rBC core of either 110 nm or 200 nm mobility diameter was passed through the SP2.

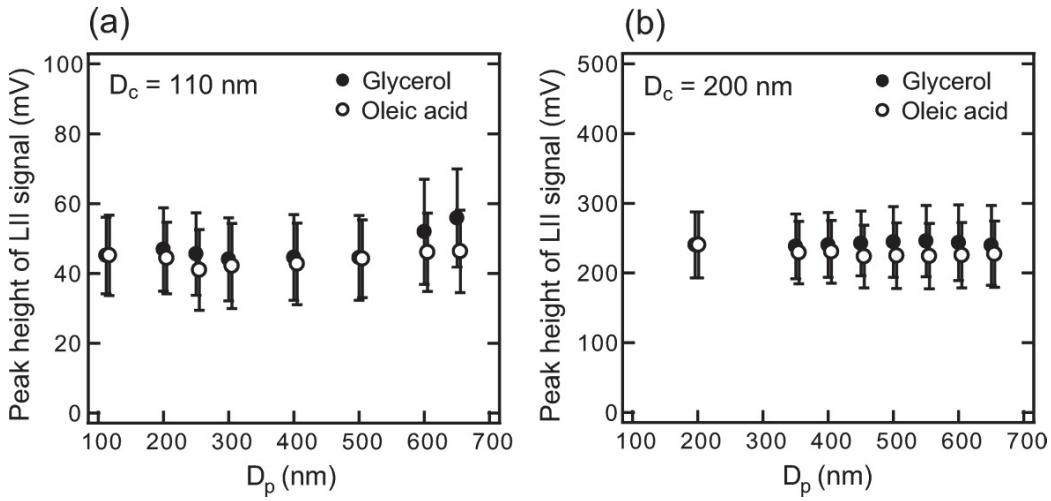

Figure 1.7: Maximum LII signal height as a function of total particle diameter (Moteki and Kondo, 2007).

The aerosol was coated with Glycerol or Oleic acid, and coating thickness was varied. The peak of the LII signal did not change significantly as coating mass increased, indicating LII signal peak is independent of coating thickness for the range of coating tested (Moteki and Kondo, 2007). Therefore SP2 users can say with some certainty the mass of rBC can be obtained accurately for a coated rBC particle. Not tested is whether fractal-like particles (*i.e.* instead of the spherical rBC particles tested in Moteki and Kondo (2007)) with coating would have a coating-independent LII signal. Additionally, the coatings were created in a laboratory, and it is unknown if the oleic acid and glycerol coatings have similar thermodynamic and optical properties to organic coating seen in the atmosphere. Further work is required to investigate these variances.

1.4.2 Differential mobility analyzer

The DMA classifies particles by electrical mobility. Electrical mobility, Z, is the terminal velocity of a particle of Φ charges in an electric field of unit strength. Mathematically this is defined as,

$$Z = \frac{\Phi e C_c(d_\mathrm{p})}{3\pi\mu d_\mathrm{p}}, \tag{1.7}$$

where Φ is the number of charges, e is the elementary charge constant, μ is the viscosity of the gas, d_p is the mobility equivalent diameter, and $C_c(d_\mathrm{p})$ is the Cunningham slip correction factor evaluated at the particles mobility equivalent diameter. Mobility equivalent diameter, commonly referred to as mobility diameter, is the diameter of a sphere with the same terminal velocity in a uniform electric field as a spherical reference particle. Mathematically the mobility diameter is defined as (DeCarlo et al., 2004),

$$d_\mathrm{p} = \frac{C_c(d_\mathrm{p}) d_{ve} \chi_t}{C_c(d_{ve})}, \tag{1.8}$$

where χ_t is the shape factor, and d_{ve} is the volume equivalent diameter of the particle. Volume equivalent diameter is defined as the diameter of a particle if it was a perfect sphere with no void spaces.

A diagram of one half of the classification region of the DMA is shown in Figure 1.8. The full classification region has an inner cylindrical rod with an outer casing, and an air gap in between the rod and casing. Upstream of the classification chamber, a polydisperse aerosol first passes through an impactor which removes particles with a aerodynamic diameter greater than a chosen cut-off. Downstream of the impactor, but still upstream of the classification chamber, the particles are passed through a neutralizer which is long enough so the aerosol has a sufficient residence time to acquire a Boltzmann distribution of charge states.

The aerosol enters the classification region in a laminar flow region adjacent to the interior of the casing. Interior to the laminar flow region is a flow of particle free air, called the sheath flow. A voltage difference is applied between the rod and casing, and near the bottom of the rod is a gap allowing airflow to pass. When a particle

enters the classification region, it reaches terminal velocity nearly instantaneously, and as a particle traverses the classifier, electrical force pulls particles of the opposite charge of the central rod towards it. If the mass-mobility relationship is correctly assumed, particles of the selected electrical mobility travel a parabolic path ending by entering the gap in the bottom of the charged rod. Particles with a larger electrical mobility traverse a parabolic arc and land above the air gap, while particles with a smaller electrical mobility travel further than the air gap and are filtered out. Thus, only particles within a small mobility range around the desired particle mobility successfully transverse the classifier into the gap. The gap leads to the outlet of the instrument, where a monodisperse aerosol with respect to mobility is provided for the application (Hinds, 1999).

1.4.3 Centrifugal particle mass analyzer

The CPMA classifies particles by mass-to-charge ratio by balancing electrical and centrifugal force, with a schematic of the CPMA shown in Figure 1.9. The user can operate the CPMA by either selecting a single mass setpoint to allow through the classifier, or programming a range of masses for the CPMA to step through sequentially. The sequence of classifying through a low to high mass setpoint range is called a scan. Regarding the construction of the CPMA, the classification region is comprised of two coaxial rotating cylindrical electrodes with a voltage difference applied between them. The polydisperse aerosol enters through a gap at the start of the classification region and a second gap at the end of the classification region is where the monodisperse aerosol exits. When the CPMA is in operation, a particle enters the classification region, and the rotating electrodes impart a centrifugal force while the voltage difference causes an electrical force. Each electrode rotates in the same direction at a slightly different constant angular velocity. Therefore, particles of the selected mass-to-charge ratio with an opposite charge of the inner cylinder

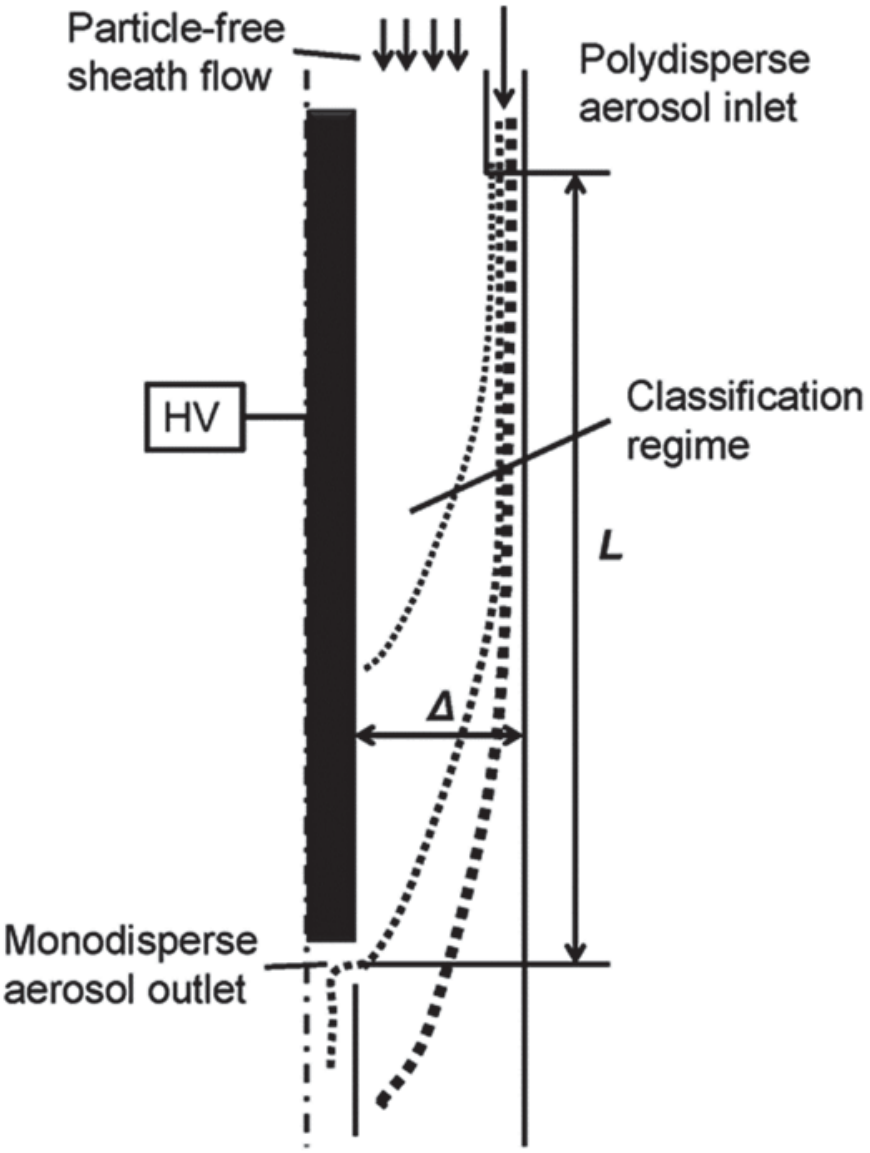

Figure 1.8: A schematic demonstrating the operating principal of a Differential Mobility Analyzer (Zhang and Chen, 2014)

successfully transverses the classifier, and all other particles impact and adhere to the walls (Olfert and Collings, 2005).

There are three important characteristics the user needs to be aware of when using the CPMA. Firstly, although the user selects a mass to classify, the CPMA actually sorts by mass-to-charge ratio and does not produce a true mass monodisperse aerosol. Along with particles of the selected mass and one charge, particles of twice the desired mass with two charges, up to the maximum number of charges in the aerosol, will also successfully transverse the classifier. Assuming a Boltzmann charge distribution, depending on particle size, the proportion of multiply charged particles may be significant. Therefore the presence of multiple charges may require some post-processing to remove these multiple charged particles depending on the application. Secondly, at low rotational speeds, such as when classifying relatively large particles, neutral particles of very high mass may not be classified out, and pass through the classifier. This is undesirable, however these large particles are generally obvious when post-processing. Finally, particles with a mass-to-charge ratio slightly above and below the desired value pass through the classifier. The probability of a particle of a selected mass-to-charge ratio traversing the classifier is characterized by a distribution, known as a transfer function, which is explained in detail in Section A.4.

1.5 Current methods of measuring rBC mass in particles

Measuring characteristics of atmospheric rBC are vital if atmospheric scientists are to accurately determine the effects of rBC on climate change. Current methods of measuring rBC and coating mass of atmospheric particles containing rBC include: i) waveform analysis using the Single Particle Soot Photometer (SP2), ii) denuder-CPMA-DMA, and iii) Soot Particle Aerosol Mass Spectrometer (SP-AMS).

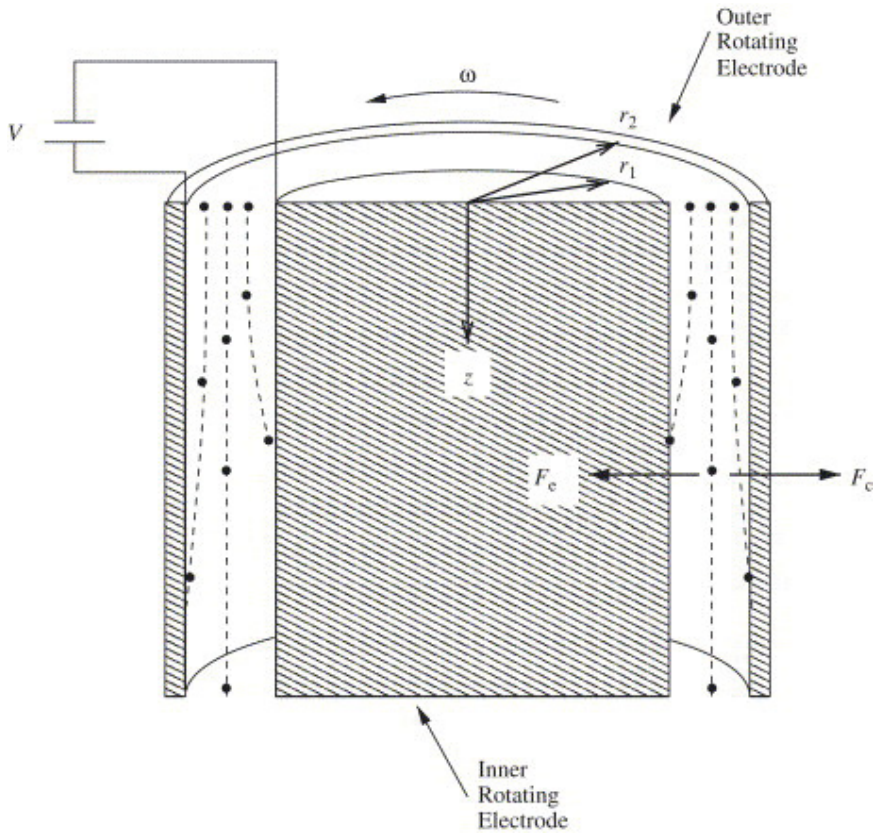

Figure 1.9: A Schematic demonstrating the operating principal of the Centrifugal Particle Mass Analyzer (Olfert and Collings, 2005)

1.5.1 Analysis of scattering and incandescence waveforms using single particle soot photometer

To infer thickness of organic coating on rBC particles the SP2 scattering signal is compared to the LII signal. As seen in Figure 1.10 when a rBC particle is coated there is a time lag between the occurrence of the peak of the scattering and LII signal. The time lag occurs because the coating must be vaporized before the rBC core begins vaporization. This signal can be related to the thickness of the coating of the rBC particle, by comparing to analogous time lags during calibration (Moteki and Kondo, 2007).

There are several challenges associated with using an SP2-only method. It requires calibration of the LII and scattering signal to rBC particles of a known coating thickness, generally a rBC mass standard (*e.g.* fullerene soot, aquadag) coated with oleic acid or some equivalent organic material. Calibrating this method requires further research, since there have been no studies comparing whether an rBC mass standard coated with oleic acid exhibit similar scattering and incandescence characteristics to that of atmospheric rBC coated in volatile organic material. It has yet to be determined whether calibration conducted with a spherical rBC core with oleic acid is representative of actual atmospheric rBC, where the rBC core is fractal. A serious limitation of this method is the scattering and incandescence detectors have different ranges, the scattering channel has a mass-equivalent range of 200—430 nm, while the incandescence channel has a range of 70—500 nm, assuming an rBC density of 1.8 g cm^{-3}. Therefore the scattering channel severely limits the utility of this method, potentially precluding measurement of the complete range of coated rBC particles.

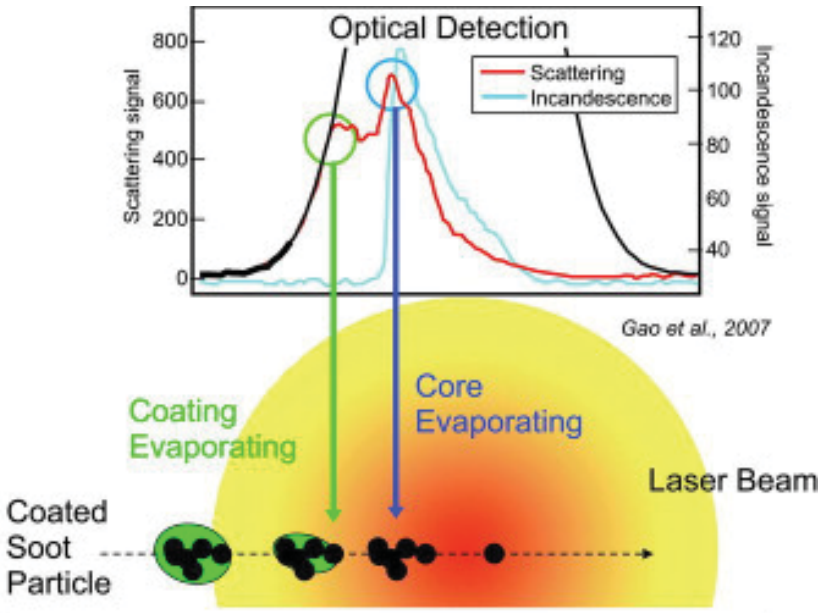

Figure 1.10: Visual representation of the SP2 theory, adapted from Onasch et al. (2012)

1.5.2 Population mixing state using DMA-CPMA

A method was introduced by Dickau et al. (2016) to quantify the mixing state of an aerosol when the aerosol particles were external or internal mixtures of volatile and non-volatile material. This method could be used to gather one variable population metrics for an external mixture of BC particles and volatile organic material. Population mixing state is calculated using three experiments using various combinations of a DMA, CPMA, denuder, and condensation particle counter (CPC). A denuder is a device which strips the organic coating from a core of non-organic material. In this case an aerosol stream entered a tube which was heated to about 350°. A CPC is an instrument which determines the number concentration of particles with a diameter between 10–3000 nm, and concentrations up to 10^4 cm^{-3} with an accuracy of approximately ±10%.

The method described in Dickau et al. (2016) is summarized below. Firstly the number mobility distribution, $\frac{\mathrm{d}N}{\mathrm{d}\log d_\mathrm{p}}$, is determined via an SMPS, which consists

of a DMA and CPC. Secondly, using a DMA, denuder with bypass, and CPC, the the number of particles which are purely volatile at a selected mobility diameter, $f_{\mathrm{vp}}(d_{\mathrm{p}})$, are determined. Thirdly, the volatile mass fraction, f_{vm} across the range of masses observed in the sample is determined using a DMA, hot and cold denuder, CPMA, and CPC. The number distribution of non-volatile material as a function of mobility diameter, $\frac{\mathrm{d}N_{\mathrm{nv}}}{\mathrm{d}\log d_{\mathrm{p}}} = (1 - f_{\mathrm{vp}})\frac{\mathrm{d}N}{\mathrm{d}\log d_{\mathrm{p}}}$, the number distribution of purely volatile material, $\frac{\mathrm{d}N_{\mathrm{pv}}}{\mathrm{d}\log d_{\mathrm{p}}} = (f_{\mathrm{vp}})\frac{\mathrm{d}N}{\mathrm{d}\log d_{\mathrm{p}}}$, and the mass distribution of volatile material, $\frac{\mathrm{d}M_{\mathrm{pv}}}{\mathrm{d}\log d_{\mathrm{p}}} = m_{\mathrm{pv}}(f_{\mathrm{vp}})\frac{\mathrm{d}N}{\mathrm{d}\log d_{\mathrm{p}}}$, can be determined. If this method was applied to atmospheric BC measurements, the coating on BC particles would be the volatile material.

There are two main challenges with this method. Firstly, it takes several hours to complete, making it difficult to use for atmospheric science measurements. Any time-dependent effects would be essentially averaged out. Secondly, BC is not distinguishable from other PM, a distinction that SP2 or SP2-like methods can make.

1.5.3 Soot particle aerosol mass spectrometer

The SP-AMS is used to obtain a mass distribution of rBC, organic components, and sulfates as a function of vacuum aerodynamic diameter. Additionally it can provide emissions characterization of combustion sources (Onasch et al., 2012). It is analogous to the combination of two instruments, an Aerosol Mass Spectrometer (AMS) and an SP2. A schematic along with sample results are shown in Figure 1.11. An aerosol stream enters an inlet nozzle and is drawn into the vacuum chamber. In the vacuum chamber, time of flight spectroscopy is used to measure vacuum aerodynamic diameter, where vacuum aerodynamic diameter refers to measurement of aerodynamic diameter in the free-molecular regime (DeCarlo et al., 2004). Downstream of the time of flight spectrometer, refractory particles such as rBC are vaporized using a Nd:YAG

laser and non-refractory particles are vaporized using a tungsten plate heated to approximately 600°C. The scattering and incandescence signals of refractory particles are measured, analogous to the process described for the SP2 in Section 1.4.1. Mass spectroscopy is used to determine chemical properties of both the refractory vaporized using the ND:YAG laser and non-refractory material vaporized on the tungsten plate. After data processing, the SP-AMS returns an average mass distribution as a function of vacuum aerodynamic diameter for an ensemble of particles (Jayne et al., 2000; Onasch et al., 2012).

There are several challenges associated with using the SP-AMS. It is it is very expensive and non-portable, costing up to over one million Canadian dollars and weighing over one hundred kilograms. Additionally, it is unclear the exact rBC and organic coating mass range to which the instrument can effectively conduct measurements with reasonable error. The mass range of rBC which the instrument can measure may be outside that usually seen in the atmosphere, resulting in missing and incomplete data (Dickau et al., 2016).

1.6 Inverse problems

Generally, scientists want to know the mass or number distribution of an aerosol as a function of some physical or chemical property. However, the distribution of particles cannot be measured directly, and an inversion is required to calculate population distributions from physical measurements. This results in what is called an inverse problem, and an inversion is required to mathematically estimate the true mass or number distribution. The solution of inverse problems is an active area of research in the aerosol science community (Kandlikar and Ramachandran, 1999).

The need for data inversion can be demonstrated by considering a CPMA-SP2 system measuring either uncoated or coated rBC particles. When a CPMA and

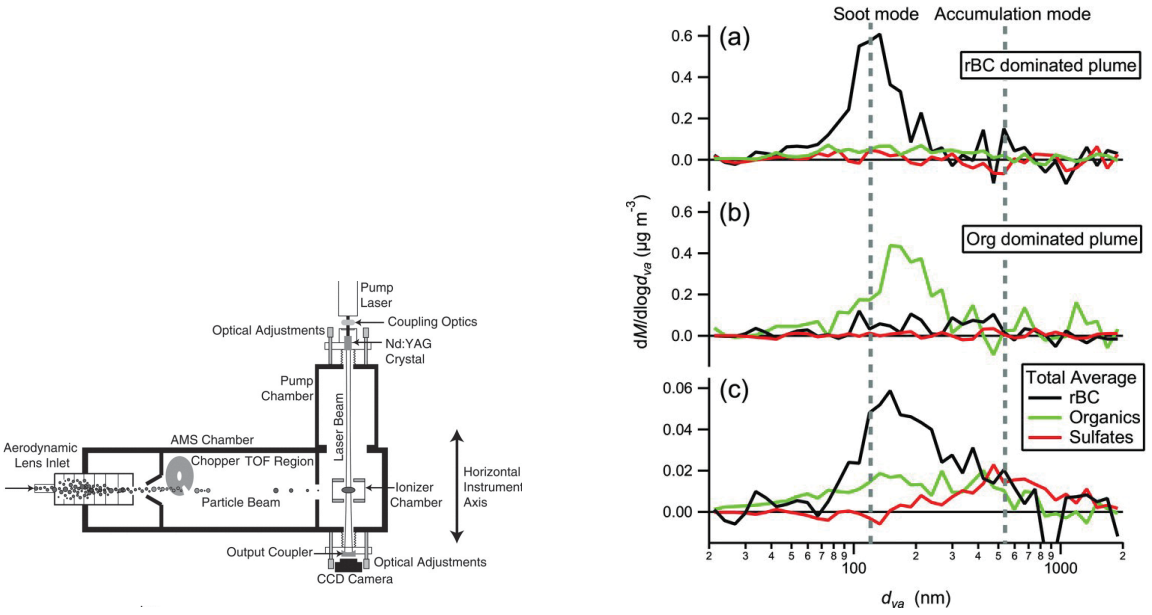

(a) (b)

Figure 1.11: a) schematic of the soot particle aerosol mass spectormeter, and b) sample results from ambient air measurements over a busy street for a case of rBC dominated PM and organic material dominated PM (Onasch et al., 2012).

SP2 are connected in series, the SP2 measures the mass of rBC in each CPMA classified particle. The raw data for a CPMA-SP2 system is shown in Figure 1.12 for bare, uncoated rBC and for coated rBC. The raw data is known as the response of the instrument, and such a distribution is measured for each CPMA setpoint. The response of the CPMA-SP2 system for bare, uncoated particles (Figure 1.12a) has distinct peaks with medians at integer multiples of the CPMA setpoint. This behaviour is due to the CPMA sorting by mass-to-charge ratio, since particles with twice the mass and two charge states are also let through. For coated particles (Figure 1.12b), the charge states blend together, and cannot be distinguished visually. Additionally, the CPMA has some error, a distribution of particles are let through the classifier rather than particles of exactly the selected mass-to-charge ratio. This distribution is described by the transfer function, defined as the probability of a particle of a certain mass passing through the classifier. To recreate the number

distribution from the response of the CPMA-SP2, system an inversion is required which accounts for the CPMA transfer function and multiple charging.

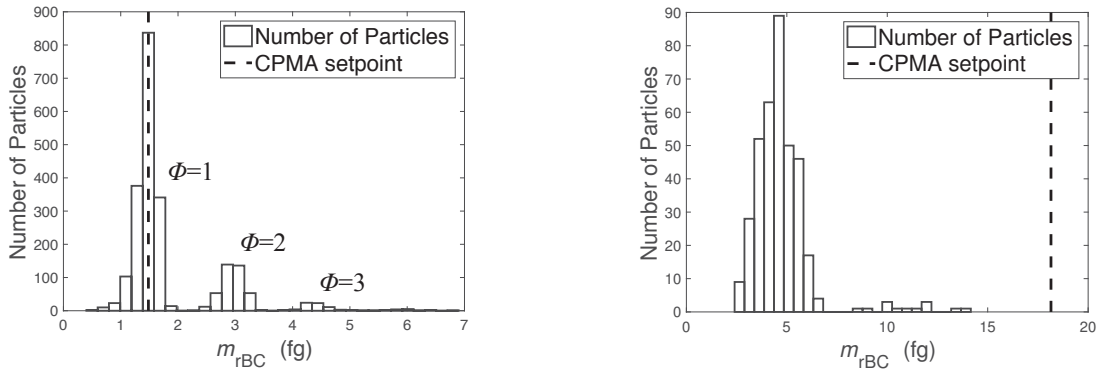

Figure 1.12: Raw data from a CPMA-SP2 system at a single CPMA setpoint for a) uncoated, bare rBC particles, and b) coated rBC particles

The response of an instrument can be related to the desired number distribution by solving an inverse problem, and a set of inverse problems which describe stepped aerosol science instrumentation are Fredholm integral equations. A Fredholm integral equation is mathematically defined as (Kandlikar and Ramachandran, 1999),

$$R(x) = \int_a^b \Gamma(x, y) p(y) \mathrm{d}y, \tag{1.9}$$

where $R(x)$ is the response of the system (*i.e.* the observed or measured data), $\Gamma(x, y)$ is the kernel function which describes the relationship between the response and the model parameters, and $p(y)$ is the unknown quantity which cannot be directly measured. Applying Fredholm theory to the CPMA-SP2 system, $R(x)$ is the distribution described in Figure 1.12, $\Gamma(x, y)$ is the kernel function specific to the CPMA-SP2 system, and $p(y)$ is the number distribution of the aerosol as a function of either rBC mass or total particle mass.

1.6.1 Solving one variable inverse problems analytically

Using simplifying assumptions, some inverse problems can be solved analytically. Recovery of a number distribution for a DMA using an analytical model has been previously described (Stolzenburg and McMurry, 2008). Using a similar method an analytical solution to the number distribution can be calculated for a CPMA-SP2 system where the SP2 acts as a simple counter of particle mass. The CPMA is assumed to have a triangular CPMA transfer function, and all particles are assumed to have a single charge. In reality, the CPMA transfer function is non-triangular and particles assume a Boltzmann charge distribution when passed through a neutralizer. Therefore this analytical solution is more for demonstration purposes, and assuming other transfer function models or multiple charging is discussed in Chapter 2. Variables for this derivation are defined as follows: β is the inverse of the CPMA resolution in mass space; f^* is the charge fraction evaluated at the set point and a charge state of 1; and variables with a * indicate they are evaluated at the CPMA set point (*e.g.* m_{p}^* is the mass setpoint of the CPMA, compared to m_{p} which is particle mass). CPMA resolution is the full width half maximum of the triangular transfer function.

The analytical solution is developed as follows: when the CPMA is held at one mass setpoint, the number concentration of rBC particles measured by the SP2 is,

$$N^* = \int \mathrm{d}N^* = \sum_{\Phi=1}^{\Phi} \int \epsilon(m_{\mathrm{p}}) f(m_{\mathrm{p}}, \Phi) \Omega(m_{\mathrm{p}}, m_{\mathrm{p}}^*, B, \Phi) \mathrm{d}N, \tag{1.10}$$

where

$$\mathrm{d}N = \frac{\mathrm{d}N}{\mathrm{d}\ln m_{\mathrm{p}}} \mathrm{d}\ln m_{\mathrm{p}} = \frac{\mathrm{d}N}{\mathrm{d}\ln m_{\mathrm{p}}} \frac{\mathrm{d}m_{\mathrm{p}}}{m_{\mathrm{p}}}. \tag{1.11}$$

Assuming the efficiency, charge fractions, and distribution are constant over the range of the transfer function, and that the fraction of multiply-charged particles is zero, this can be simplified to:

$$N^* = \epsilon^* f^* \left[\frac{\mathrm{d}N}{\mathrm{d}\ln m_\mathrm{p}}\right]^* \int \Omega(m_\mathrm{p}, m_\mathrm{p}^*, B, \Phi = 1)\frac{\mathrm{d}m_\mathrm{p}}{m_\mathrm{p}}. \tag{1.12}$$

With the assumptions of single charging, a unique relationship between size and mass, and the distribution is approximately uniform over the width of the transfer function, we can eliminate charge and size dependency and assume a triangular transfer function in mass space:

$$\Omega(m_\mathrm{p}^*, \beta, m_\mathrm{p}) = \begin{cases} \dfrac{m_\mathrm{p} - (1-\beta)m_\mathrm{p}^*}{\beta m_\mathrm{p}^*} & \text{if } (1-\beta)m_\mathrm{p}^* < m_\mathrm{p} < m_\mathrm{p}^*, \\ \dfrac{(1+\beta)m_\mathrm{p}^* - m_\mathrm{p}}{\beta m_\mathrm{p}^*} & \text{if } m_\mathrm{p}^* < m_\mathrm{p} < (1+\beta)m_\mathrm{p}^* \end{cases} \tag{1.13}$$

and $\Omega = 0$ elsewhere.

Then, defining $\tilde{m}_\mathrm{p} = \dfrac{m_\mathrm{p}}{m_\mathrm{p}^*}$, the integral can be evaluated,

$$\begin{aligned} \int \Omega \frac{\mathrm{d}m_\mathrm{p}}{m_\mathrm{p}} = \int_{1-\beta}^{1} \frac{\tilde{m}_\mathrm{p} - (1-\beta)}{\beta}\frac{\mathrm{d}\tilde{m}_\mathrm{p}}{\tilde{m}_\mathrm{p}} + \int_{1}^{1+\beta} \frac{(1+\beta) - \tilde{m}_\mathrm{p}}{\beta}\frac{\mathrm{d}\tilde{m}_\mathrm{p}}{\tilde{m}_\mathrm{p}} \\ = (1+\frac{1}{\beta})\ln(1+\beta) - (1-\frac{1}{\beta})\ln(1-\beta). \end{aligned} \tag{1.14}$$

This equation is valid for $\beta < 1$. For brevity define this integral as $\hat{\beta}$,

$$\int \Omega \,\mathrm{d}\ln m_\mathrm{p} = (1+\frac{1}{\beta})\ln(1+\beta) - (1-\frac{1}{\beta})\ln(1-\beta) = \hat{\beta}, \tag{1.15}$$

where $\hat{\beta} \approx \beta$ when $\beta << 1$.

Therefore,

$$N^* = \epsilon^* f^* \left[\frac{\mathrm{d}N}{\mathrm{d}\ln m_\mathrm{p}}\right]^* \hat{\beta} \tag{1.16}$$

$$\left[\frac{\mathrm{d}N}{\mathrm{d}\ln m_{\mathrm{p}}}\right]^{*} = \frac{N^{*}}{\epsilon^{*} f^{*} \hat{\beta}} \approx \frac{N^{*}}{\epsilon^{*} f^{*} \beta}. \tag{1.17}$$

This is analogous to Stolzenburgs' equation for the DMA. For high resolution, we get:

$$\left[\frac{\mathrm{d}N}{\mathrm{d}\ln m_{\mathrm{p}}}\right] = \frac{N^{*}}{\epsilon^{*} f^{*} \beta} \approx \frac{R_m N^{*}}{\epsilon^{*} f^{*}}, \tag{1.18}$$

where $R_{\mathrm{m}} = \dfrac{1}{\beta}$. This shows the distribution over the natural logarithm of mass is approximately equal to the number concentration measured at the set point, multiplied by the resolution. Conversion to logarithm with base of 10 is possible by conducting the same analysis above, but with logarithms with base of 10. Change of logarithm basis from base 10 to base e can be conducted using,

$$\left[\frac{\mathrm{d}N}{\mathrm{d}\log m_{\mathrm{p}}}\right]^{*} \frac{1}{\ln 10} = \left[\frac{\mathrm{d}N}{\mathrm{d}\ln m_{\mathrm{p}}}\right]^{*}. \tag{1.19}$$

An example of the solution is shown in Figure 1.13, where $\dfrac{\mathrm{d}N}{\mathrm{d}\log m_{\mathrm{p}}}$ is a function of total particle mass.

1.6.2 Solving one variable inverse problems numerically

Section 1.6.1 discussed solving inverse problems analytically, assuming particles are singly charged and the CPMA has a triangular transfer function. These assumptions are not necessarily representative of real world instrumentation behaviour. Assuming multiple charging and non-triangular transfer functions has been demonstrated for scanning mobility particle sizer measurements (SMPS), which consists of a DMA and CPC in series. Discussion of an SMPS inversion introduces terminology and concepts central to this thesis and analogies can be drawn between inversion of SMPS data and the CPMA-SP2 inversion developed in Chapter 2. The DMA sorts particles by mobility, the result of DMA classification being an aerosol which is near-monodisperse in electrical mobility. The DMA steps through a range of mobility diameters and

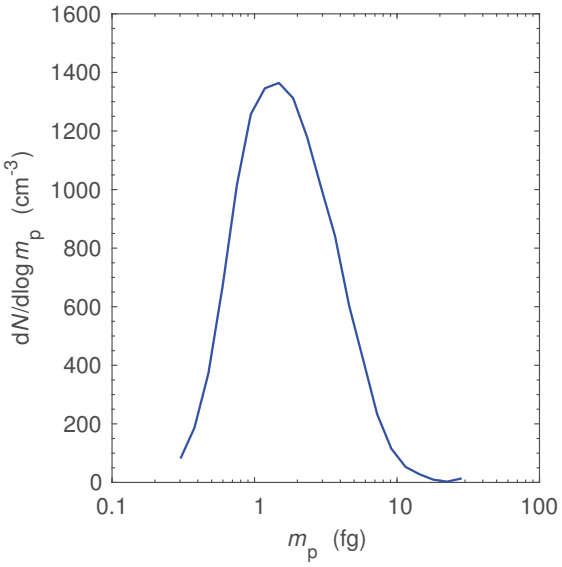

Figure 1.13: Number distribution as a function of total particle mass solved for using analytical solution to a Fredholm integral assuming a triangular CPMA transfer function and singly charged particles

the CPC measures the number of particles at the DMA selected mobility diameter. Analogous to a CPMA-SP2 system described in Section 1.6.1, the SMPS has an instrument response. Some particles will have more than one charge, meaning that particles of half the mobility as selected but with two charge states will be let through the DMA. The presence of multiply charged particles and the transfer function needs to be accounted for via inversion to properly calculate the distribution of particles in the aerosol sample. For an SMPS, $R(x)$ is the mean number of particles measured at a particular mobility diameter and $p(y)$ is the number distribution $\dfrac{\mathrm{d}N}{\mathrm{d}\log d_\mathrm{p}}$. The distribution represents the concentration of particles, $\mathrm{d}N$, between a mobility diameter of d_p and $d_\mathrm{p} + \mathrm{d}\log d_\mathrm{p}$. The Kernal function for an SMPS is defined for i data points (*i.e.* number of setpoints or channels) and j solution elements (Collins et al., 2002),

$$\Gamma_{i,j} = q_a t_c \log\left(\frac{D_{j+\frac{1}{2}}}{D_{j-\frac{1}{2}}}\right)\bar{\eta}(D_j)\sum_{\Phi=0}^{\Phi_{\max}}\bar{f}(D_j,\Phi)\bar{\Omega}(Z(D_j,\Phi),Z_i,\mathrm{Pe}(D_j)), \tag{1.20}$$

where q_a is the aerosol flow rate, t_c is the time counting particles, $\bar{\eta}(D_j)$ is the average percentage of particles lost in the DMA, $\bar{f}(D_j, \Phi)$ is the average probability of a particle of certain diameter and charge number existing, and $\bar{\Omega}(Z(D_j, \Phi), Z_i, \mathrm{Pe}(D_j))$ is the transfer function of the DMA. The transfer function of the DMA is defined as the probability of a single particle transversing the DMA (Knutson and Whitby, 1975),

$$\Omega = \frac{1}{q_a}\max\left[0, \min\left(q_a, q_s, \left[\frac{1}{2}\left(q_a + q_s\right) - \left|2\pi Z_p \Delta\Phi + \frac{1}{2}\left(q_m + q_c\right)\right|\right]\right)\right], \tag{1.21}$$

where q_s is the sampling flow rate, Z_p is the particle electrical mobility, $\Delta\Phi$ is a finite increment in electric flux, and q_m is the main outlet flow rate. The finite increment in electric flux can be approximated using,

$$\Delta\Phi = \frac{LV}{\ln\frac{b}{a}}, \tag{1.22}$$

where L is the distance between the DMA aerosol entrance and DMA sampling entrance, V is the voltage difference, r_a is the radius of the DMA's charged center rod, and r_b is the inner radius of the casing. A reasonable lognormal approximation to the transfer function has also been developed by Stolzenburg and McMurry (2008). Knowing the transfer function and kernal, equation 2.2 can be rewritten as a system of equations for all DMA diameter setpoints as,

$$\mathbf{R} = \mathbf{Q}\boldsymbol{\Gamma}, \tag{1.23}$$

where $\mathbf{R}$ is the response of the SMPS, in this case the vector of measured number concentrations, and $\mathbf{Q}$ is the unknown distribution, in this case the aerosol number distribution vector $\dfrac{\mathrm{d}N}{\mathrm{d}\log d_\mathrm{p}}$. These equations can be solved numerically.

As an aside, similar to the CPMA-SP2 counter analysis, an approximation of the solution was derived analytically by Stolzenburg and McMurry (2008) assuming all particles have a single charge and the transfer function is triangular,

$$\left.\frac{\mathrm{d}N}{\mathrm{d}\log d_\mathrm{p}}\right|_{d_\mathrm{p}^*} = \frac{N(V)a^*}{\left[\frac{q_a}{q_s}\lambda\left(1+\delta\right)\right) f\left(d_\mathrm{p}^*, 1\right)\eta\left(d_\mathrm{p}^*\right)\Big]}, \tag{1.24}$$

where Z_p^* is the electrical mobility of the centroid of the transfer function at selected diameter d_p^*, N is the number concentration measured by the CPC, λ is the ratio of DMA flows $\frac{q_s+q_a}{q_m+q_c}$. Assumption of an inversion includes that the size distribution varies little over each bin, and the detector response and charging probability are slowly varying with respect to the diameter of the particle (Kulkarni et al., 2011). If this solution is to be found using multiple charging, then a numeric solution is required, as described in Section 1.6.4.

1.6.3 Two variable inverse problems

Previous research has focused on solving inverse problems for recovery of one variable number based distributions (*i.e.* $\frac{\mathrm{d}N}{\mathrm{d}\log m_\mathrm{p}}$, $\frac{\mathrm{d}N}{\mathrm{d}\log d_\mathrm{p}}$). Recently it has been shown by Rawat et al. (2016) that two variable number distributions can provide unique insights. Specifically the two variable distribution, $\frac{\partial^2 N}{\partial m_\mathrm{p}\partial d_\mathrm{p}}$, was used to identify populations of particles in an aerosol, as seen in Figure 1.14, where d_p is the mobility diameter of particle. Thus, the term $\partial^2 N$ represents the number concentration of particles with a total particle mass between m_p and $m_\mathrm{p}+\mathrm{d}m_\mathrm{p}$ and mobility diameter between d_p and $d_\mathrm{p}+\mathrm{d}d_\mathrm{p}$. This distribution is analogous to one-variable distributions that are often used in aerosol science to describe count or mass distributions (e.g. $\frac{\mathrm{d}N}{\mathrm{d}\log d_\mathrm{p}}$ or $\frac{\mathrm{d}M}{\mathrm{d}\log d_\mathrm{p}}$). Data was gathered using a DMA, Aerosol Particle Mass Analyzer (APM), and CPC in series where the DMA sorted particles by mobility, the APM classified particles by mass-to-charge ratio, and the CPC measured the average

number of particles. The APM is similar to the CPMA. The result after inversion was a number distribution both as a function of mobility diameter and particle mass, and accounted for the APM transfer function and multiply charged particles.

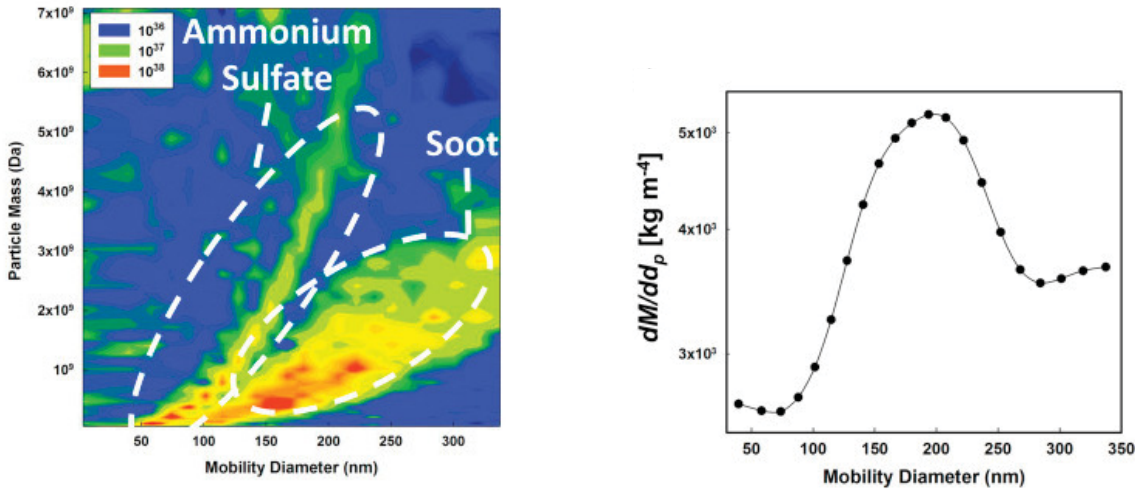

(a) (b)

Figure 1.14: From Rawat et al. (2016) a) A two variable number concentration distribution as a function of mobility diameter and total particle mass for soot and ammonium sulfate aerosols b) A one variable distribution

An additional advantage of the two variable distribution is it can be integrated in the total particle mass or mobility diameter (*i.e.* x or y) direction to derive one variable distributions. For example, a two variable distribution such as that in Rawat et al. (2016) can be integrated to find how mass or number varies with mobility diameter. Because most aerosol populations have lognormal size and mass characteristics, henceforth the distributions will be described in their lognormally normalized form:

$$\frac{\mathrm{d}N}{\mathrm{d}\log d_\mathrm{p}} = \int_0^\infty \frac{\partial^2 N}{\partial \log m_\mathrm{p} \partial \log d_\mathrm{p}} \mathrm{d}\log m_\mathrm{p} \tag{1.25}$$

$$\frac{\mathrm{d}M}{\mathrm{d}\log d_\mathrm{p}} = \int_0^\infty m_\mathrm{p} \frac{\partial^2 N}{\partial \log m_\mathrm{p} \partial \log d_\mathrm{p}} \mathrm{d}\log m_\mathrm{p}. \tag{1.26}$$

The solution to the two variable distribution still involves solving an inverse problem, only the unknown distribution is a matrix because it is a function of two variables. Solving for the two variable distribution for a DMA-APM-CPC system is possible by solving the system of equations as described by Rawat et al. (2016),

$$N_{i,j} = \sum_{z=1}^{\infty} \int_0^{\infty} \int_0^{\infty} \Gamma_{i,j}(Z, d_{\mathrm{p}}, m_{\mathrm{p}}) \frac{\partial^2 N}{\partial \log m_{\mathrm{p}} \partial \log d_{\mathrm{p}}} \mathrm{d}\log m_{\mathrm{p}} \mathrm{d}\log d_{\mathrm{p}}, \tag{1.27}$$

which can again be represented in matrix form and the two variable distribution solved for using iterative methods similar to a one variable distribution.

1.6.4 Numerical methods of solving inversion problems

The previous two sections have demonstrated how to apply Fredholm theory to derive a system of equations relating the number distribution, kernel function, and instrument response. A numerical scheme is required to solve for the number distribution. At first glance, it would appear that standard methods of solving systems of linear equations could be used. However, these methods cannot be used because the equations are dependent on one another, therefore, the kernel function is nearly singular. Non-standard methods of solving the inversion are required. Methods which may be used to generally solve an inverse problem are: I) Least-squares solution II) Non-negative least squares regression III) Tikhonov regularization and VI) the Twomey method (Kandlikar and Ramachandran, 1999). The most popular of these methods will be discussed in context to their applicability for solving the system,

$$\mathbf{R} = \mathbf{Q}\boldsymbol{\Gamma}, \tag{1.28}$$

where Γ is the kernel function, $\mathbf{Q}$ is the unknown distribution of particles to be calculated, and R is the instrument response (*e.g.* variable measured by the instrument). Least squares and non-negative least squares regression (also known as constrained least squares) involves minimizing the error of the residual. A major problem with least squares and non-negative least squares solutions is the final solution is highly dependent on the initial guess, and these methods are therefore not commonly used for inverse problems. Another method commonly utilized for solution of inverse problems is Tikhonov regularization. This method solves a minimization problem. There has been several studies on Tikhonov regularization, and it can be optimized based on the instrument being studied (Tikhonov et al., 1995). Different variations of Tikhonov regularization have been proposed such as zeroth order regularization, L-curve minimization (Hansen, 1992; Hansen and OLeary, 1993), and generalized cross-validation (Wahba, 1977; Golub et al., 1979). A disadvantages of Tikhonov regularization is it is complicated, and although possible to implement for one variable inverse problems, it would be very difficult to implement for two variable distributions. Another iterative and non-linear approach to solving inverse problems is the Twomey method (Twomey, 1975), and is simpler to conceptualize and implement. It is commonly used for solving inverse problems related to aerosol instrumentation. In a Twomey algorithm, to solve for a new iteration of the solution, each element of the old solution is multiplied by a correction factor. Initially, an initial guess needs to be provided. Using the inversion of one variable SMPS data as an example, the Twomey method can be applied to SMPS data where the new solution is given using,

$$\left.\frac{\mathrm{d}N}{\mathrm{d}\log d_\mathrm{p}}\right|^{k+1}(d_j) = \left[1 + a_i^k \Gamma_i(Z, d_j)\right] \left.\frac{\mathrm{d}N}{\mathrm{d}\log d_\mathrm{p}}\right|^{k}, \tag{1.29}$$

where a is the ratio of measured number concentration $N_{i,\mathrm{measured}}$ for each channel over the per channel number concentration calculated by integration for the new iteration

of the solution, N_i^k,

$$a_i^k = \frac{N_{i,\text{measured}}}{N_i^k}. \tag{1.30}$$

A disadvantage of the Twomey method is it induces oscillations in the solution, and the oscillations generally increase with the number of iterations. It is possible to reduce the unwanted oscillations by smoothing the initial guess and final iteration of the solution by a moving average (Markowski, 1987). Additionally, the Twomey method is computationally intensive. Despite these disadvantages, its relative simplicity means this method is commonly used for solving inverse problems.

Finally, techniques using Bayesian statistics, such as those described in Symonds et al. (2007), can be used to recover number distributions. However, they are more suited to recovery of data from very noisy instruments, and are not applicable to the CPMA-SP2 method developed here.

1.7 Research Overview and Implications

In this research, a CPMA-SP2 inversion is developed which measures rBC mass and coating mass distribution. A theoretical basis for the methodology is presented which accounts for multiple charging and the transfer function of the CPMA. The results of the inversion result in a two variable number distribution being a function of rBC mass and total particle mass. This thesis is comprised of four chapters. Chapter 2 discusses the development, theory, and validation of the SP2-CPMA measurement methodology. Chapter 3 describes the results of using this method to measure rBC particle mass distributions in China. Lastly, Chapter 4 summarizes and discusses the results and presents conclusions.

References

Andreae, M. and Gelencsér, A. (2006). Black carbon or brown carbon? the nature of light-absorbing carbonaceous aerosols. *Atmospheric Chemistry and Physics*, 6(10):3131–3148.

Biswas, S., Verma, V., Schauer, J. J., Cassee, F. R., Cho, A. K., and Sioutas, C. (2009). Oxidative potential of semi-volatile and non volatile particulate matter (PM) from heavy-duty vehicles retrofitted with emission control technologies. *Environmental science & technology*, 43(10):3905–3912.

Bond, T. C. and Bergstrom, R. W. (2006). Light absorption by carbonaceous particles: An investigative review. *Aerosol science and technology*, 40(1):27–67.

Bond, T. C., Doherty, S. J., Fahey, D. W., Forster, P. M., Berntsen, T., Deangelo, B. J., Flanner, M. G., Ghan, S., Karcher, B., Koch, D., Kinne, S., Kondo, Y., Quinn, P. K., Sarofim, M. C., Schultz, M. G., Schulz, M., Venkataraman, C., Zhang, H., Zhang, S., Bellouin, N., Guttikunda, S. K., Hopke, P. K., Jacobson, M. Z., Kaiser, J. W., Klimont, Z., Lohmann, U., Schwarz, J. P., Shindell, D., Storelvmo, T., Warren, S. G., and Zender, C. S. (2013). Bounding the role of black carbon in the climate system: A scientific assessment. *Journal of Geophysical Research Atmospheres*, 118(11):5380–5552.

Cakmak, S., Dales, R. E., Gultekin, T., Vidal, C. B., Farnendaz, M., Rubio, M. A., and Oyola, P. (2009a). Components of particulate air pollution and emer-

gency department visits in chile. *Archives of environmental & occupational health*, 64(3):148–155.

Cakmak, S., Dales, R. E., and Vida, C. B. (2009b). Components of particulate air pollution and mortality in chile. *International Journal of Occupational and Environmental Health*, 15(2):152–158.

Cappa, C. D., Onasch, T. B., Massoli, P., Worsnop, D. R., Bates, T. S., Cross, E. S., Davidovits, P., Hakala, J., Hayden, K. L., Jobson, B. T., and others (2012). Radiative absorption enhancements due to the mixing state of atmospheric black carbon. *Science*, 337(6098):1078–1081.

Collins, D. R., Flagan, R. C., and Seinfeld, J. H. (2002). Improved inversion of scanning dma data. *Aerosol Science & Technology*, 36(1):1–9.

Dastanpour, R. and Rogak, S. N. (2014). Observations of a Correlation Between Primary Particle and Aggregate Size for Soot Particles. *Aerosol Science and Technology*, 48(10):1043–1049.

Davis, D. L. (2002). A look back at the london smog of 1952 and the half century since. *Environmental health perspectives*, 110(12):A734.

DeCarlo, P. F., Slowik, J. G., Worsnop, D. R., Davidovits, P., and Jimenez, J. L. (2004). Particle morphology and density characterization by combined mobility and aerodynamic diameter measurements. Part 1 Theory. *Aerosol Science and Technology*, 38(12):1185–1205.

Dickau, M., Olfert, J., Stettler, M. E. J., Boies, A., Momenimovahed, A., Thomson, K., Smallwood, G., and Johnson, M. (2016). Methodology for quantifying the volatile mixing state of an aerosol. *Aerosol Science and Technology*, 50(8):759–772.

Dusek, U., Frank, G. P., Hildebrandt, L., Curtius, J., Schneider, J., Walter, S., Chand, D., Drewnick, F., Hings, S., Jung, D., Borrmann, S., and Andreae, M. O. (2006). Size matters more than chemistry for cloud-nucleating ability of aerosol particles. *Science*, 312(5778):1375–1378.

Frampton, M. W., Stewart, J. C., Oberdörster, G., Morrow, P. E., Chalupa, D., Pietropaoli, A. P., Frasier, L. M., Speers, D. M., Cox, C., Huang, L.-S., and others (2006). Inhalation of ultrafine particles alters blood leukocyte expression of adhesion molecules in humans. *Environmental Health Perspectives*, pages 51–58.

Golub, G. H., Heath, M., and Wahba, G. (1979). Generalized cross-validation as a method for choosing a good ridge parameter. *Technometrics*, 21(2):215–223.

Gong Jr, H., Linn, W. S., Sioutas, C., Terrell, S. L., Clark, K. W., Anderson, K. R., and Terrell, L. L. (2003). Controlled exposures of healthy and asthmatic volunteers to concentrated ambient fine particles in Los Angeles. *Inhalation toxicology*, 15(4):305–325.

Gustafsson, . and Ramanathan, V. (2016). Convergence on climate warming by black carbon aerosols. *Proceedings of the National Academy of Sciences*, 113(16):201603570.

Hallquist, M., Wenger, J. C., Baltensperger, U., Rudich, Y., Simpson, D., Claeys, M., Dommen, J., Donahue, N. M., George, C., Goldstein, A. H., and others (2009). The formation, properties and impact of secondary organic aerosol: current and emerging issues. *Atmospheric Chemistry and Physics*, 9(14):5155–5236.

Hansen, P. C. (1992). Analysis of discrete ill-posed problems by means of the L-curve. *SIAM review*, 34(4):561–580.

Hansen, P. C. and OLeary, D. P. (1993). The use of the L-curve in the regularization of discrete ill-posed problems. *SIAM Journal on Scientific Computing*, 14(6):1487–1503.

Henderson, S. B., Beckerman, B., Jerrett, M., and Brauer, M. (2007). Application of land use regression to estimate long-term concentrations of traffic-related nitrogen oxides and fine particulate matter. *Environmental Science & Technology*, 41(7):2422–2428. PMID: 17438795.

Hinds, W. C. (1999). *Aerosol technology: Properties, behavior, and measurement of airborne particles. 1999*. Wiley: New York.

Jacobson, M. Z. (2001). Strong radiative heating due to the mixing state of black carbon in atmospheric aerosols. *Nature*, 409(6821):695–697.

Janssen, N. A. H., Hoek, G., Simic-Lawson, M., Fischer, P., Van Bree, L., Ten Brink, H., Keuken, M., Atkinson, R. W., Anderson, H. R., Brunekreef, B., and others (2011). Black Carbon as an Additional Indicator of the Adverse Health Effects of Airborne Particles Compared with PMˆ sub 10ˆ and PMˆ sub 2.5ˆ. *Environmental health perspectives*, 119(12):1691.

Jayne, J. T., Leard, D. C., Zhang, X., Davidovits, P., Smith, K. A., Kolb, C. E., and Worsnop, D. R. (2000). Development of an aerosol mass spectrometer for size and composition analysis of submicron particles. *Aerosol Science and Technology*, 33(1-2):49–70.

Kandlikar, M. and Ramachandran, G. (1999). Inverse methods for analysing aerosol spectrometer measurements: a critical review. *Journal of Aerosol Science*, 30(4):413–437.

Knutson, E. O. and Whitby, K. T. (1975). Aerosol classification by electric mobility: apparatus, theory, and applications. *Journal of Aerosol Science*, 6(6):443–451.

Koch, D. and Del Genio, A. (2010). Black carbon semi-direct effects on cloud cover: review and synthesis. *Atmospheric Chemistry and Physics*, 10(16):7685–7696.

Kulkarni, P., Baron, P. A., and Willeke, K. (2011). *Aerosol measurement: principles, techniques, and applications*. John Wiley & Sons.

Lack, D. A. and Cappa, C. D. (2010). Impact of brown and clear carbon on light absorption enhancement, single scatter albedo and absorption wavelength dependence of black carbon. *Atmospheric Chemistry and Physics*, 10(9):4207–4220.

Maricq, M. M. (2007). Chemical characterization of particulate emissions from diesel engines: A review. *Journal of Aerosol Science*, 38(11):1079–1118.

Markowski, G. R. (1987). Improving Twomey's algorithm for inversion of aerosol measurement data. *Aerosol science and technology*, 7(2):127–141.

McMeeking, G. R., Morgan, W. T., Flynn, M., Highwood, E. J., Turnbull, K., Haywood, J., and Coe, H. (2011). Black carbon aerosol mixing state, organic aerosols and aerosol optical properties over the United Kingdom. *Atmospheric Chemistry and Physics*, 11(17):9037–9052.

Mills, N. L., Miller, M. R., Lucking, A. J., Beveridge, J., Flint, L., Boere, A. J. F., Fokkens, P. H., Boon, N. A., Sandstrom, T., Blomberg, A., and others (2011). Combustion-derived nanoparticulate induces the adverse vascular effects of diesel exhaust inhalation. *European heart journal*, page ehr195.

Mills, N. L., Robinson, S. D., Fokkens, P. H. B., Leseman, D. L. A. C., Miller, M. R., Anderson, D., Freney, E. J., Heal, M. R., Donovan, R. J., Blomberg, A., and

others (2008). Exposure to concentrated ambient particles does not affect vascular function in patients with coronary heart disease. *Environmental health perspectives*, 116(6):709.

Mills, N. L., Törnqvist, H., Robinson, S. D., Gonzalez, M., Darnley, K., MacNee, W., Boon, N. A., Donaldson, K., Blomberg, A., Sandstrom, T., and others (2005). Diesel exhaust inhalation causes vascular dysfunction and impaired endogenous fibrinolysis. *Circulation*, 112(25):3930–3936.

Moosmüller, H., Chakrabarty, R. K., and Arnott, W. P. (2009). Aerosol light absorption and its measurement: A review . *Journal of Quantitative Spectroscopy and Radiative Transfer*, 110(11):844 – 878.

Moteki, N. and Kondo, Y. (2007). Effects of Mixing State on Black Carbon Measurements by Laser-Induced Incandescence. *Aerosol Science and Technology*, 41(4):398–417.

Moteki, N. and Kondo, Y. (2010). Dependence of Laser-Induced Incandescence on Physical Properties of Black Carbon Aerosols: Measurements and Theoretical Interpretation. *Aerosol Science and Technology*, 44(8):663–675.

Olfert, J. S. and Collings, N. (2005). New method for particle mass classificationthe Couette centrifugal particle mass analyzer . *Journal of Aerosol Science*, 36(11):1338 – 1352.

Onasch, T. B., Trimborn, A., Fortner, E. C., Jayne, J. T., Kok, G. L., Williams, L. R., Davidovits, P., and Worsnop, D. R. (2012). Soot Particle Aerosol Mass Spectrometer: Development, Validation, and Initial Application. *Aerosol Science and Technology*, 46(7):804–817.

Pachauri, R. K., Meyer, L., Plattner, G.-K., Stocker, T., and others (2015). *IPCC, 2014: Climate Change 2014: Synthesis Report. Contribution of Working Groups I, II and III to the Fifth Assessment Report of the Intergovernmental Panel on Climate Change*. IPCC.

Petzold, A., Ogren, J. A., Fiebig, M., Laj, P., Li, S.-M., Baltensperger, U., Holzer-Popp, T., Kinne, S., Pappalardo, G., Sugimoto, N., et al. (2013). Recommendations for reporting" black carbon" measurements. *Atmospheric Chemistry and Physics*, 13(16):8365–8379.

Rawat, V. K., Buckley, D. T., Kimoto, S., Lee, M. H., Fukushima, N., and Hogan, C. J. (2016). Two dimensional size-mass distribution function inversion from differential mobility analyzer-aerosol particle mass analyzer (DMA-APM) measurements. *Journal of Aerosol Science*, 92:70–82.

Riddervold, I. S., Bønløkke, J. H., Mølhave, L., Massling, A., Jensen, B., Grønborg, T. K., Bossi, R., Forchhammer, L., Kjærgaard, S. K., and Sigsgaard, T. (2011). Wood smoke in a controlled exposure experiment with human volunteers. *Inhalation toxicology*, 23(5):277–288.

Riemer, N., Vogel, H., and Vogel, B. (2004). Soot aging time scales in polluted regions during day and night. *Atmospheric Chemistry and Physics*, 4(7):1885–1893.

Riemer, N. and West, M. (2013). Quantifying aerosol mixing state with entropy and diversity measures. *Atmospheric Chemistry and Physics*, 13(22):11423–11439.

Schnaiter, M., Linke, C., Mhler, O., Naumann, K.-H., Saathoff, H., Wagner, R., Schurath, U., and Wehner, B. (2005). Absorption amplification of black carbon internally mixed with secondary organic aerosol. *Journal of Geophysical Research: Atmospheres*, 110(D19):n/an/a.

Schnitzler, E. G., Dutt, A., Charbonneau, A. M., Olfert, J. S., and Jäger, W. (2014). Soot aggregate restructuring due to coatings of secondary organic aerosol derived from aromatic precursors. *Environmental Science & Technology*, 48(24):14309 – 14316.

Schwarz, J. P., Spackman, J. R., Gao, R. S., Perring, A. E., Cross, E., Onasch, T. B., Ahern, A., Wrobel, W., Davidovits, P., Olfert, J., and others (2010). The detection efficiency of the single particle soot photometer. *Aerosol Science and Technology*, 44(8):612–628.

Seinfeld, J. H. and Pandis, S. N. (2016). *Atmospheric chemistry and physics: from air pollution to climate change*. John Wiley & Sons.

Solomon, C., Balmes, J., Jenkins, B. M., and Kleinman, M. (2003). The effect of smoke from burning vegetative residues on airway inflammation and pulmonary function in healthy, asthmatic, and allergic individuals. *Final report to the California Air Resources Board and the California Environmental Protection Agency*.

Sorensen, C. (2011). The mobility of fractal aggregates: a review. *Aerosol Science and Technology*, 45(7):765–779.

Stephens, M., Turner, N., and Sandberg, J. (2003). Particle identification by laser-induced incandescence in a solid-state laser cavity. *Appl. Opt.*, 42(19):3726–3736.

Stolzenburg, M. R. and McMurry, P. H. (2008). Equations Governing Single and Tandem DMA Configurations and a New Lognormal Approximation to the Transfer Function. *Aerosol Science and Technology*, 42(6):421–432.

Symonds, J. P. R., Reavell, K. S. J., Olfert, J. S., Campbell, B. W., and Swift, S. J. (2007). Diesel soot mass calculation in real-time with a differential mobility spectrometer. *Journal of Aerosol Science*, 38(1):52–68.

Tikhonov, A. N., Goncharsky, A. V., Stepanov, V. V., and Yagola, A. G. (1995). *Numerical methods for the solution of ill-posed problems*, volume 328. Springer Science & Business Media.

Twomey, S. (1975). Comparison of constrained linear inversion and an iterative nonlinear algorithm applied to the indirect estimation of particle size distributions. *Journal of Computational Physics*, 18(2):188 – 200.

Wahba, G. (1977). Practical approximate solutions to linear operator equations when the data are noisy. *SIAM Journal on Numerical Analysis*, 14(4):651–667.

World Health Organization (2012). *Health effects of black carbon*. WHO.

Young, H. D. and Freedman, R. A. (2008). *University Physics: with modern physics*. Pearson: San Fancisco.

Zhang, J. and Chen, D. (2014). Differential Mobility Particle Sizers for Nanoparticle Characterization. *Journal of Nanotechnology in Engineering and Medicine*, 5(2):20801.

Chapter 2

A Novel Inversion Method to Determine the Mass Distribution of Non-Refractory Coatings on Refractory Black Carbon using a Centrifugal Particle Mass Analyzer and Single Particle Soot Photometer

2.1 Introduction

Aerosols containing refractory black carbon (rBC) particles in the atmosphere have important climate impacts due to their ability to absorb and scatter light. Refractive black carbon aerosols are the second most influential anthropogenic climate changing compound, however, the magnitude of the impact of rBC on climate change is highly uncertain (Bond et al., 2013). A major source of this uncertainty is due to coating of non-rBC compounds onto rBC, changing the particles absorption and scattering characteristics (aerosol direct effects on radiative forcing) and influences on cloud life-cycle (semi-direct and indirect effects on radiative forcing) (Menon et al., 2002; Ramanathan and Carmichael, 2008). Acquisition of non-rBC coating can occur at the source of emission (*e.g.* from unburned fuel or engine oil condensed on soot

emitted from engines (Maricq, 2007), or from secondary organic aerosol condensing or coagulating with the rBC (Schnaiter et al., 2005; Moosmüller et al., 2009; Riemer et al., 2004). On a single particle, the mass ratio of non-rBC to rBC may vary, which is referred to as mass fraction. The non-rBC coatings are generally organic compounds and measuring the mass distribution on atmospheric rBC is important for understanding the effect of coating on climate. To reduce uncertainty on the effect of rBC on climate forcing, it is desirable to quantify mass and number distribution characteristics of an aerosol population containing rBC particles.

The most common methodology to determine coating characteristics of atmospheric rBC particles is to infer it using a single particle soot photometer (SP2; Droplet Measurement Technologies, Boulder, CO). SP2 methodologies are explained in detail el(Moteki and Kondo, 2007; Shiraiwa et al., 2007; Sedlacek et al., 2012; McMeeking et al., 2010, 2011; Schwarz et al., 2008), and briefly in Section 2.2.1. Bare rBC particles passing through an SP2 Nd:YAG laser produce incandescence and scattering signals with near-simultaneous peak intensities. Particles with a non-rBC coating undergo a delay on the onset of the LII peak signal as organic particle coating must be vaporized before the rBC core begins to incandesce. Therefore the non-rBC coating mass is inferred by correlating the difference in time of the scattering and incandescence signal peaks to coating mass. Another approach relies on sizing rBC-containing particles optically and estimating coating amount using assumed morphology and refractive indices (Gao et al., 2007). Inferring the coating mass using peak time differencing can be difficult because the time to vaporize organic coating depends on physical and thermodynamic characteristics (Moteki and Kondo, 2007; Bambha et al., 2013) which may be challenging to quantify for atmospheric rBC. Further, these methods for estimating coating thickness is constrained by the sensitivity of the SP2's scattering detector, which can resolve particles in the range of 200-430 nm in diameter.

We present here an improvement to an alternative method to measure the mass of non-rBC coating on populations of refractory black carbon (rBC) particles using a tandem CPMA-SP2 system (Liu et al., 2017). The CPMA (Centrifugal Particle Mass Analyzer; Cambustion Ltd, UK) classifies particles by their mass to charge ratio (Olfert and Collings, 2005), and the SP2 detects the mass of rBC in each individual particle (Stephens et al., 2003; Slowik et al., 2007). In coupling the two instruments, the advantages of this method over SP2-only methods are i) coating mass information can be obtained over a much wider range of rBC particle mass compared to SP2 only methods (restricted in the SP2 by the sensitivity to light scattered by rBC), ii) coating mass is measured directly: no assumptions for coating density or refractive index are needed, and iii) it does not require assumptions of a core-shell morphology. The CPMA does not limit the range of particles measured as its classification range is 0.2 ag to 1050 fg (or a volume equivalent diameter, d_{rBC}, of 6 to 1030 nm assuming an rBC density of 1.8 g/cm^3). Regarding the SP2, only the incandescence channel is used, which has a detection range of approximately 0.3 – 117 fg rBC (or a volume equivalent diameter, d_{rBC}, of 70 to 500 nm assuming an rBC density of 1.8 g/cm^3). The detection efficiency, the number concentration detected versus the actual concentration present, may be less than 100% for rBC particles below 0.9 fg (Laborde et al., 2012), but if the laser power is tuned the efficiency can be greater than 80% down to 0.3 fg (Liu et al., 2017). Furthermore, Moteki and Kondo (2007) have shown that the incandescence signal is independent of coating thickness up to 650 nm (where coating thickness is defined as total optical diameter of the particle minus the rBC core optical diameter), thus the CPMA-SP2 can measure a wide range of coating mass fractions for different rBC core masses.

In previous work, the CPMA-SP2 system was used to calculate the average coating mass on a population of rBC particles (Liu et al., 2017). For each CPMA setpoint, the average mass of rBC particles was determined using an SP2, and divided by the

total particle mass (*i.e.* CPMA setpoint). This method assumes the CPMA transfer function is very narrow, and that the proportion of multiply charged particles which cannot be removed by inspection is small. However, in the atmosphere, a population of rBC particles has a wide range of coating mass (*i.e.* some particles in the population may have very little coating while some particles may have considerable amounts), and may have a significant proportion of multiple charge states.

The distribution of the coating material on the rBC particles can be described using a two-variable distribution described by $\frac{\partial^2 N}{\partial \log m_\mathrm{p} \partial \log m_\mathrm{rBC}}$; where m_rBC is the mass of an individual rBC particle and m_p is the mass of an individual particle. Thus, the term $\partial^2 N$ represents the number concentration of particles with a rBC particle mass between m_rBC and $m_\mathrm{rBC} + \mathrm{d}m_\mathrm{rBC}$ and total particle mass between m_p and $m_\mathrm{p} + \mathrm{d}m_\mathrm{p}$. This distribution is analogous to one-variable distributions that are often used in aerosol science to describe count or mass distributions (e.g. $\frac{\mathrm{d}N}{\mathrm{d}\log d_\mathrm{p}}$ or $\frac{\mathrm{d}M}{\mathrm{d}\log d_\mathrm{p}}$). A two-variable distribution of mobility and mass has been previously demonstrated for a differential mobility analyzer - aerosol particle mass analyzer (DMA-APM) system (Rawat et al., 2016).

A useful property of the two variable distribution is it can be integrated to derive one variable distributions of the total aerosol population, for example, total mass concentration distribution as a function of total particle mass can be obtained,

$$\frac{\mathrm{d}M}{\mathrm{d}\log m_\mathrm{p}} = \int \frac{\partial^2 N}{\partial \log m_\mathrm{p} \partial \log m_\mathrm{rBC}} m_\mathrm{p} \partial \log m_\mathrm{rBC}. \tag{2.1}$$

Additionally, other distributions can be derived; i) mass concentration distribution as a function of rBC particle mass $\left(\frac{\mathrm{d}M}{\mathrm{d}\log m_\mathrm{rBC}}\right)$ ii) rBC mass concentration distribution as a function of total particle mass $\left(\frac{\mathrm{d}M_\mathrm{rBC}}{\mathrm{d}\log m_\mathrm{p}}\right)$ and iii) rBC mass concentration distribution as a function of rBC particle mass $\left(\frac{\mathrm{d}M_\mathrm{rBC}}{\mathrm{d}\log m_\mathrm{rBC}}\right)$. Similarly,

the total mass concentration, M, and total number concentration, N, can be calculated through double integration of the two variable distribution. Note that since the SP2 only measures particles containing rBC, the total mass concentration refers to the total mass concentration of particles containing rBC, and N refers to the total number concentration of particles containing rBC. As the CPMA is an aerosol classifier, and not a single-particle instrument, a data inversion process is required to determine the two-variable distribution. Additionally, the CPMA-SP2 inversion presented in this paper mathematically accounts for multiple charging. In the subsequent sections a data inversion routine is developed for the CPMA-SP2 system resulting in a two-variable distribution. The inversion routine is tested and validated experimentally using rBC particles coating by secondary organic aerosol in a smog chamber.

2.2 Experimental Methods

2.2.1 CPMA-SP2 system

The CPMA is an aerosol instrument which classifies particles based on their mass-to-charge ratio. The principal of operation is based on balanced rotational and electrical forces between two rotating coaxial cylinders. The probability of a particle making its way through the entirety of the CPMA is described by the instrument 'transfer function'. The transfer function of the CPMA is approximately triangular and can described by its resolution, which is the inverse of the normalized full width half maximum (FWHM) of the transfer function (e.g. a resolution of 5 results in a triangular transfer function with a FWHM of 20% of the mass setpoint). During step-scan operations, the CPMA sequentially changes rotational speed and electrode voltage potential to select a chosen quantity of mass setpoints between a range of user-selected values.

The SP2 operates by drawing an aerosol stream through a Nd:YAG intra-cavity laser ($\lambda = 1064$ nm). The absorbing particles are vaporized and the scattered and incandescent light are measured by avalanche photo-diodes and photomultiplier tubes, respectively. The scattered light signal is related to a nominal optical scattering diameter, and incandescent detectors relate the peak of the incandescent signal to rBC mass (Stephens et al., 2003; Moteki and Kondo, 2010). Calibration of the SP2 is conducted by correlating peak incandescent signal to rBC mass, and was conducted using a CPMA-SP2 system using bare, uncoated rBC particles, where rBC produced from the inverted burner was mass selected using the CPMA. Supplementary information section S1 shows the calibration of rBC mass for the SP2 and efficiency of the SP2.

2.2.2 Experimental Procedure

The inversion was tested using smog chamber experiments, where rBC particles with a range of secondary organic coating mass were sampled using the CPMA-SP2 system. The experimental setup is shown in Figure 2.1. Refractory BC particles were produced from an inverted methane diffusion flame, similar to that described in Ghazi and Olfert (2013). The flow rate of fuel and air was 1.6 and 17.4 standard L min^{-1} respectively (with reference temperature and pressure of 0 °C and 101.325 kPa, respectively), resulting in a global equivalence ratio of approximately 0.85. The particles were subsequently passed at 1 L min^{-1} through a 25 cm diffusion drier, consisting of a mesh tube surrounded by anhydrous calcium sulfate; a thermodenuder at 350°C with a heated section of 25 cm with $\frac{1}{4}$ inches diameter tubing; a tube of activated carbon 91 cm long and diameter of $\frac{1}{4}$ inches; and a counter-flow parallel plate denuder (similar to that described in Ruiz et al. (2006)) prior to entering the chamber. The purpose of the diffusion drier was to remove water from the aerosol phase. The thermodenuder partitioned any organic material on the particles to the vapor phase,

which either condensed onto the walls of the cooling section of the denuder or adsorbed onto the activated carbon following the denuder. The counter-flow parallel plate denuder removed trace gases which may have remained after these processes. The smog chamber has been previously described by Parsons et al. (2011), it has a volume of 1.8 m^{-3}, perfluoroalkoxy film walls, and twenty-four 34 W black lights arranged on the top and opposite walls of the inside of the chamber.

The smog chamber was filled to a concentration of approximately 10,000 cm^{-3}, verified with a Scanning Mobility Particle Sizer (SMPS; TSI Inc) connected directly to the smog chamber (not shown in experimental diagram). A precursor hydrocarbon, *p*-xylene (Fisher, 99.9%), was injected into the chamber with the lights off. Particle mass growth (i.e. coating) does not occur with the lights off due to the absence of shortwave radiation. The uncoated, bare rBC particles were sampled using the CPMA-SP2, with the SP2 recording the mass and time of CPMA-classified rBC on a single particle basis. During sampling using the CPMA-SP2, the CPMA was sequentially stepped over a mass range from 0.3 to 28 fg, and the SP2 measured the mass of rBC comprising individual CPMA-classified particles. Each setpoint was held for 30 seconds, and the CPC measured particle concentration for reference. A valve downstream of the neutralizer and upstream of the CPMA was fitted to bypass the CPMA, so that the aerosol could also be measured by the SP2 alone. Before each CPMA scan the CPMA was bypassed and the SP2 sampled directly from the chamber, this data is required to correct the inversion process as described in Section 2.3. After one scan of the bare rBC particles, hydrogen peroxide was introduced into the chamber, and the lights turned on. Photolysis of the hydrogen peroxide produced hydroxyl radicals, which reacted with the *p*-xylene precursor. The secondary organic material condensed onto the bare rBC over a period of 7 hours, and the lights irradiated the chamber for the rest of the experiment. Over the period of coating growth, the CPMA-SP2 system sampled the aerosol from the smog chamber using the same parameters and setpoint

time. After 7 hours, fresh rBC was injected into the chamber resulting in a co-existing populations of both bare and coated rBC particles. This mixed population was sampled using the same technqiue. The polydisperse particle distribution was charge-neutralized before sampling, by a Kr-85 radioactive source. A condensation particle counter (CPC, Model 3771, TSI, USA) was set to a flow rate of 1.0 L min^{-1} and the SP2 was set to a flow rate of 0.12 L min^{-1}, resulting in a total flow through the CPMA of 1.12 L min^{-1}.

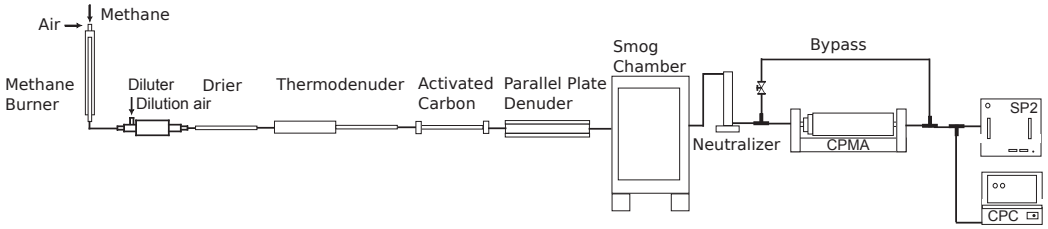

Figure 2.1: Experimental set-up

Figure 2.1 shows the output of the SP2 when a CPMA is operated upstream at a single setpoint. For a single CPMA setpoint the output of the SP2 can be envisaged as an rBC mass distribution, hereafter referred to as the response of the system. For a neutralized stream of uncoated rBC particles as seen in Figure 2.2a, charge states are clearly visible—doubly charged particles of twice the mass have the same mass-to-charge ratio as singly charged particles of the setpoint mass. The first 3 charge states, $\Phi = 1, 2, 3$, are clearly visible, and the CPMA set-point is equal to the median of the singly charged particle distribution. As seen in Figure 2.2b, for coated particles, the rBC distribution blends together. The multiply charged particles are still present but they are not distinguishable from each other as particles of the same total particle mass (as classified by the CPMA) comprise a wide range of rBC mass. However, because the charge distribution and CPMA resolution is known for a neutralized stream of particles, an inversion can be used to account for the multiple charge states in order to accurately reconstruct the mass and number distributions

of coated particles.

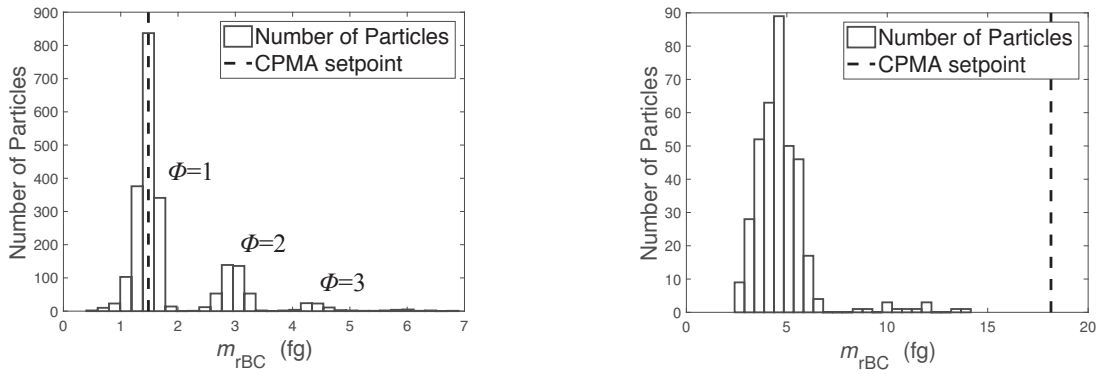

Figure 2.2: Number-mass histogram of particles at a particular CPMA setpoint counted by the SP2 a) for uncoated and bare rBC particles at a CPMA setpoint of 1.87 fg b) for coated particles at a CPMA setpoint of 18.15 fg

2.3 Inversion of CPMA-SP2 data

An inversion is the process of solving an inverse problem, where parameters which cannot be directly measured or observed are inferred. A subset of inverse problems are Fredholm integral equations which are applicable to data acquired from aerosol science instrumentation such as DMA-CPC systems or cascade impactors. The unknown quantity desired to be known for aerosol instrumentation is generally the number or mass distribution entering the instrument. Development of inversions for DMA and tandem-DMA data is analogous to the development of a CPMA-SP2 inversion and has been discussed previously (Hagen and Alofs, 1983; Collins et al., 2002; Stolzenburg and McMurry, 2008; Kulkarni et al., 2011). The general form of the Fredholm integral equation is,

$$R(x) = \int_a^b \Gamma(x, y) p(y) \mathrm{d}y, \tag{2.2}$$

where $R(x)$ is the response of the system (*i.e.* the observed or measured data), $\Gamma(x, y)$ is the kernel function which describes the relationship between the response and the model parameters, and $p(y)$ is an unknown quantity which cannot be directly measured. Applying Fredholm integral theory to a CPMA-SP2 system, the two variable distribution (*i.e.* the unknown variable) $\frac{\partial^2 N}{\partial \log m_{\mathrm{p}} \partial \log m_{\mathrm{rBC}}}$ can be related to the response and kernel of the CPMA-SP2 system for the i^{th} setpoint assuming the distribution and charge fraction are approximately constant over the width of the transfer function,

$$\left.\frac{\mathrm{d}N_{\mathrm{Response}}}{\mathrm{d}\log m_{\mathrm{rBC}}}\right|_i = \left.\frac{\partial^2 N}{\partial \log m_{\mathrm{p}} \partial \log m_{\mathrm{rBC}}}\right|_i \bar{\epsilon}(m_{\mathrm{p}}) \sum_{\Phi=1}^{\Phi_{\max}} \bar{f}(d_{\mathrm{p}}, \Phi) \int_0^{\infty} \Omega(m_{\mathrm{p}}, B, \Phi) \mathrm{d}\log m_{\mathrm{p}}, \tag{2.3}$$

where $\mathrm{d}\log m_{\mathrm{p}} = \frac{1}{m_{\mathrm{p}}}\mathrm{d}m_{\mathrm{p}}$, $\bar{\epsilon}(m_{\mathrm{p}})$ is a correction factor, $\bar{f}(d_{\mathrm{p}}, \Phi)$ is charge fraction, and $\Omega(m_{\mathrm{p}}, B, \Phi)$ is the CPMA transfer function. Unlike in Rawat et al. (2016), where a two variable distribution for a DMA-APM-CPC system is calculated, the response of the CPMA-SP2 system is a number distribution with respect to m_{rBC} rather than the number concentration of particles. The number distribution $\left.\frac{\mathrm{d}N_{\mathrm{Response}}}{\mathrm{d}\log m_{\mathrm{rBC}}}\right|_i$ is constructed from single particle measurements of rBC particle mass by the SP2 at CPMA setpoint i (*e.g.* taking data in the form of Figure 2.2a and converting it into a number distribution). The bins, which are the range of edges for histogram bins of $\left.\frac{\mathrm{d}N_{\mathrm{Response}}}{\mathrm{d}\log m_{\mathrm{rBC}}}\right|_i$, have geometric midpoints equal to the CPMA setpoints.

The CPMA transfer function, $\Omega(m_{\mathrm{p}}, B, \Phi)$, describes the probability of a particle with a particular mass-to-charge ratio passing through the classifier. The transfer function is a function of the mechanical mobility, B, of a particle, and its number of charges, Φ. There are several models of transfer function available, and the diffusive function similar to that seen in Olfert and Collings (2005) is used for all calculations because it is the most accurate and is not computationally intensive.

Like a SMPS, the CPMA-SP2 inversion assumes a charge distribution of neutralized aerosol (Wang and Flagan, 1990). Charge fraction, $f(d_{\mathrm{p}}, \Phi)$, describes the proportion of particles of a particular size and charge state calculated using the Wiedensohler equations (Wiedensohler, 1988). A study by Gopalakrishnan et al. (2015) showed the assumptions of the Wiedensohler equations may not be representative in all cases, especially for non-spherical particles. However, the Wiedensohler equations are still commonly used in modelling neutralized aerosols due to their simplicity. The maximum number of charges, Φ_{max}, is specified for the inversion and typically is chosen to be 3, since a negligible number of particles exist with higher charge states for the size range investigated in this study. Selection of higher number of charge states increases solution time.

Determining mobility equivalent diameter requires assumptions of particle mobility diameter and density. Both are required to calculate the charge fraction and the CPMA transfer function. The mobility diameter and density assumption affects the amplitude of the two variable distribution, and to a lesser extent, the width. The amplitude is primarily affected, rather than the width, because these assumptions affect the shape of the CPMA transfer function, which describes how many particles pass through the CPMA. A wider transfer function results in the two variable distribution having a higher concentration (*i.e.* increased amplitude). Additionally, just like all aerosol science instrumentation, diffusion and other mechanistic processes cause losses of particles within the CPMA again affecting the amplitude of the two variable distribution. The amplitude of the two variable distribution can be corrected by introducing the correction factor, ϵ. The correction factor is determined using the data from the direct SP2 sampling performed during CPMA bypass measurements following each CPMA-SP2 scan. The mass dependency of $\epsilon(m_{\mathrm{p}})$ was ignored, since the SP2 can only measure rBC mass, not total particle mass, and it is not possible to determine the correction factor as a function of total particle mass. Thus the av-

erage correction factor will be determined, represented by $\bar{\epsilon}$. The correction factor is determined by calculating the total number concentration of the SP2 sampling alone (*i.e.* bypassing the CPMA), and dividing by the number concentration calculated by the two variable CPMA-SP2 data (*i.e.* using the inversion),

$$\bar{\epsilon} = \frac{N_{\mathrm{SP2}}}{N}, \tag{2.4}$$

where N is the total number concentration of the two-variable distribution and N_{SP2} is the number concentration of particles through direct SP2 measurement (*i.e.* no CPMA upstream of the SP2) over the same m_{rBC} range as the two-variable distribution. This assumes the CPMA scan range is high enough so it covers the vast majority of total particle masses.

The entire set of CPMA setpoints can be represented by an ill-conditioned positively constrained system of equations,

$$\mathbf{R} = \mathbf{Q}\mathbf{\Gamma}, \tag{2.5}$$

where $\mathbf{Q}$ is the two variable number distribution, $\dfrac{\partial^2 N}{\partial \log m_{\mathrm{p}} \partial \log m_{\mathrm{rBC}}}$, and $\mathbf{R}$ is the number distribution of the response. Similar to the kernel function developed by Collins et al. (2002) for scanning DMA data, the kernel function, $\Gamma_{i,j}$, represents the response of the instrument with a trapezoidal rule approximation for the i^{th} instrument response and the j^{th} solution element of the known number distribution of m_{rBC}. Ignoring the correction factor, $\bar{\epsilon}$, for now, the kernel can be represented as,

$$\Gamma_{i,j} = \sum_{\Phi=1}^{\Phi_{\max}} \bar{f}(m_{\mathrm{p}}, \Phi) \int_{m_{\mathrm{p}(j-1/2)}}^{m_{\mathrm{p}(j+1/2)}} \Omega(m_{\mathrm{p}}, B, \Phi) \mathrm{d} \log m_{\mathrm{p}}, \tag{2.6}$$

where the terms $m_{\mathrm{p}(j+1/2)}$ and $m_{\mathrm{p}(j-1/2)}$ represent the edges of the j$^{\mathrm{th}}$ bin of rBC masses, where the bin edges are the geometric midpoint between adjacent bin midpoints. To

solve Equation 2.5 for the unknown two variable number distribution, a Twomey algorithm (Twomey, 1975) was used. This algorithm was selected because it is easy to implement and generally stable, albeit computationally expensive. Briefly, the Twomey method works by first approximating the two variable distribution with an initial guess. The initial guess is calculated by taking the response of the CPMA-SP2 system at the i$^{\text{th}}$ CPMA setpoint, and dividing by the charge fraction assuming all particles were singly charged and by the variable $\hat{\beta}$. The variable $\hat{\beta}$ is the analytical solution to the integral of a triangular CPMA transfer function assuming a single charge and is described in detail in section S3.1. Bins with an rBC mass greater than total mass are set to zero because are they are physically impossible, and the initial guess is calculated using,

$$\left.\frac{\partial^2 N_{\text{guess}}}{\partial \log m_{\text{p}} \partial \log m_{\text{rBC}}}\right|_i = \frac{\left.\frac{\mathrm{d}N_{\text{Response}}}{\mathrm{d}\log m_{\text{rBC}}}\right|_i}{\bar{f}(m_{\text{p},i}, \Phi = 1)\hat{\beta}}, \tag{2.7}$$

where $\left.\frac{\partial^2 N_{\text{guess}}}{\partial \log m_{\text{p}} \partial \log m_{\text{rBC}}}\right|_i$ is the initial guess for the i$^{\text{th}}$ CPMA setpoint, and $\left.\frac{\mathrm{d}N_{\text{Response}}}{\mathrm{d}\log m_{\text{rBC}}}\right|_i$ is the response of the CPMA-SP2 system at the i$^{\text{th}}$ CPMA setpoint.

The Twomey algorithm then iteratively calculates: i) a theoretical response by multiplying the guess of the two variable distribution by Gamma, ii) a correction factor for each element of the two variable distribution based on the actual and theoretical response, iii) the new two variable distribution by multiplying element-by-element the old two variable distribution by the correction factor to resolve a new guess of the two variable distribution. This sequence is iterated until the total number concentration of the two variable solution approaches that which was originally measured by the CPMA-SP2 within 5%. After solving for the two variable distribution, the amplitude is corrected by multiplying by the correction factor, $\bar{\epsilon}$.

For low rBC concentrations, smoothing may be desirable. For the smog cham-

ber experiments, smoothing was not conducted because concentrations were relatively high and the distribution of rBC particles was narrow. For broad distributions and/or distributions with a low concentration of rBC particles, the initial guess can be smoothed via an averaging algorithm until roughness increases or 10 iterations are reached. The smoothing algorithm is similar to that used by Markowski (Markowski, 1987) in smoothing one variable distributions recovered using a Twomey algorithm. Roughness was defined as the average of the second derivative of the two variable distribution. Iterating the Twomey algorithm induces noise into the solution. Therefore, after the final iteration is calculated the solution is smoothed until it reaches the roughness of the smoothed initial guess. The smoothing algorithm was designed to preserve the total number distribution.

Further information on the inversion is given in the supplementary information. Section S2 gives detailed information on the Twomey algorithm and solving the two variable distribution. Section S3 explores model validation in three ways. First, an analytical solution for number concentration distribution is developed for the CPMA-SP2 system assuming a triangular transfer function and one charge state. The numerical solution with the aforementioned assumptions is shown to be identical to the analytical model. Second, the corrected one variable number concentration distribution of uncoated particles is shown to be nearly identical to direct SP2 measurement. Third, an incorrect mobility is assumed, and shown to result in the same distribution as a more reasonable assumption. This demonstrates mobility only changes distribution amplitude as expected, which can be corrected using the correction factor, $\bar{\epsilon}$. Section S4 explains in more detail why the diffusion transfer function was selected for the model.

2.4 Results and Discussion

Results from the inversion, specifically for coated, uncoated, and a mixed population of coated and uncoated particles are presented in this section. Additional results are available in section S5 of the supplementary information.

2.4.1 Two variable number concentration distributions

A two variable number distribution, $\frac{\partial^2 N}{\partial \log m_{\mathrm{p}} \partial \log m_{\mathrm{rBC}}}$, a function of rBC particle mass and total particle mass are shown in Figure A.9 for populations of a) uncoated, b) coated, and c) mixture of coated and uncoated particles. The color represents the magnitude of the two variable distribution, and the units are in number of particles squared per cm^6. The size of each rectangle represents the limits of the histogram bins used in the inversion. The geometric center of each bin corresponds to the i^{th} CPMA setpoint mass in the total mass and rBC mass direction (because rBC bins were chosen to correspond to each CPMA setpoint). The white dotted line represents where particles are uncoated (i.e. $m_{\mathrm{p}} = m_{\mathrm{rBC}}$). Particles to the left of the white dotted line of unity slope are physically impossible because the rBC particle mass exceeds that of the total particle mass of the particle, but could occur if the particle had a stronger incandescence response compared to the material used to calibrate the SP2. Smoothing was conducted for the latter two cases, but was not conducted for uncoated particles as the distribution is narrow. In Figure 2.3a the multiple charge states are not visible for the two variable distribution of uncoated, bare rBC particles. This is because inversion charge-corrects the distribution by removing particles with an rBC particle mass greater than total particle mass, then adjusting the amplitude to account for removing these particles.

The two variable distribution for bare, uncoated rBC particles seen in Figure 2.3a exists along a line with slope equal to one. This is because the particles are

not coated and thus the total particle mass is equal to the mass of rBC. When the particles grew an organic coating as seen in Figure 2.3b, the distribution shifted towards a higher total particle mass. The distribution does not increase in the rBC particle mass direction since the rBC particle mass does not increase. The widening of the distribution is due to the particle-to-particle variation in the condensational growth rate of secondary organic aerosol, which creates a distribution of total particle mass for particles of a given rBC particle mass. When fresh uncoated rBC particles are added to the smog chamber as seen in Figure 2.3c, the two distinct populations of coated and uncoated particles can be observed. The fresh particles do not fall on the one to one line because the measurement was taken 45 minutes after injecting the new particles, and thus a coating had started to develop. This time delay was intentional in order to allow the particles to completely spatially mix with the coated particles.

2.4.2 One Variable Number Distribution

Direct integration of the two variable number concentration distribution, $\frac{\partial^2 N}{\partial \log m_{\mathrm{p}} \partial \log m_{\mathrm{rBC}}}$, in the total particle mass or rBC particle mass domains (*i.e.* the x and y directions) yields $\frac{\mathrm{d}N}{\mathrm{d}\log m_{\mathrm{p}}}$ or $\frac{\mathrm{d}N}{\mathrm{d}\log m_{\mathrm{rBC}}}$. The number distribution for uncoated and coated particles can be seen in Figure 2.4. Note that the data is only shown for particles greater than 0.9 fg due to counting efficiency loss of the SP2 below that limit. This results in the left side of the number distribution being cut off. For uncoated particles, the distribution of $\frac{\mathrm{d}N}{\mathrm{d}\log m_{\mathrm{p}}}$ should have an amplitude equal to $\frac{\mathrm{d}N}{\mathrm{d}\log m_{\mathrm{rBC}}}$, however, $\frac{\mathrm{d}N}{\mathrm{d}\log m_{\mathrm{p}}}$ has a slightly higher amplitude. This could be for several reasons. Firstly, the distribution is very narrow, and the initial guess returns a more broad distribution than expected. Since the initial guess is slightly broader than expected, the solution distribution is also broad. Secondly, calibration error of

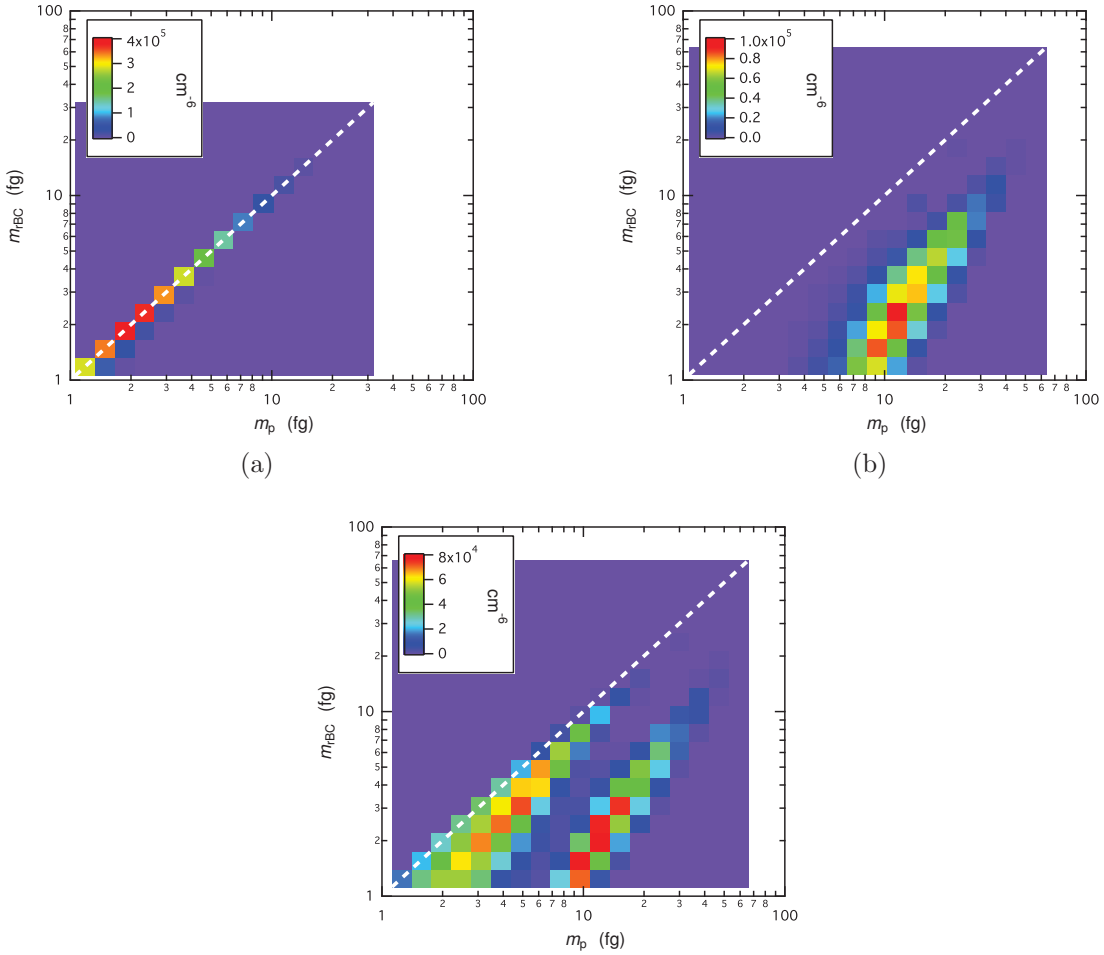

Figure 2.3: Histogram representation of two variable distributions, $\frac{\partial^2 N}{\partial \log m_{\mathrm{p}} \partial \log m_{\mathrm{rBC}}}$, for a) uncoated, bare rBC particles, b) coated rBC particles which have undergone photooxidation with p-xylene under UV lights for 7 hours, c) mixture of coated and uncoated rBC distributions. The white dashed line represents where $m_{\mathrm{rBC}} = m_{\mathrm{p}}$

the SP2 (or small amounts of coating on the rBC when the SP2 is calibrated) would result in a small shift in the distribution.

The number distributions for coated particles is seen in Figure 2.4b. For coated particles $\frac{\mathrm{d}N}{\mathrm{d}\log m_{\mathrm{rBC}}}$ has a median greater than $\frac{\mathrm{d}N}{\mathrm{d}\log m_{\mathrm{p}}}$ due to increased mass of the coating as expected. Comparing $\frac{\mathrm{d}N}{\mathrm{d}\log m_{\mathrm{rBC}}}$ for coated and uncoated particles, the distribution is similar except the median of the coated case is lower than that of the

uncoated case. This is due to the particle losses in the chamber due to diffusion to the walls.

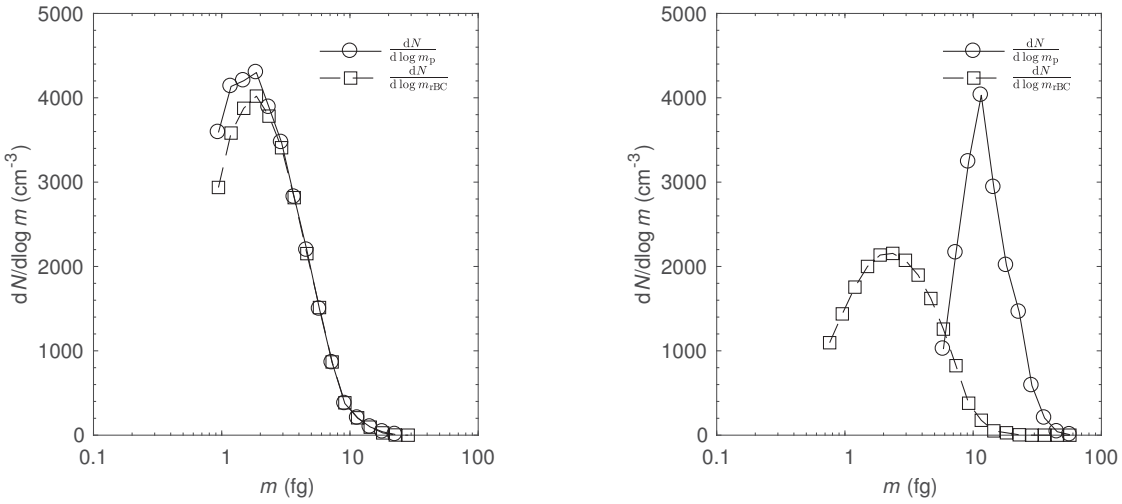

Figure 2.4: Number distributions of a) uncoated rBC particles and, b) coated rBC particles.

2.4.3 One variable mass concentration distributions

One variable mass distributions can be recovered by integration of $\frac{\partial^2 N}{\partial \log m_{\mathrm{p}} \partial \log m_{\mathrm{rBC}}}$ along either the m_{rBC} or m_{p} domains and multiplying by either rBC particle mass or total particle mass (*e.g.* Equation 1). The mass distributions can be in terms of total particle mass concentration or rBC mass concentration. As seen in Figure 2.5a, for uncoated rBC particles the rBC mass concentration distribution and total mass concentration distribution are approximately equal. This is because there is no coating on the particles and total particle mass is equivalent to rBC particle mass. As seen in Figure 2.5b for coated particles, the mass distributions as a function of rBC particle mass have approximately the same median as the uncoated case. This reflects the organic coating growth via photo-oxidation with *p*-xylene does not change the rBC particle mass in the chamber. The coated one variable mass distribution shows the

difference in total particle mass ($\frac{\mathrm{d}M}{\mathrm{d}\log m_{\mathrm{rBC}}}$) and rBC particle mass ($\frac{\mathrm{d}M_{\mathrm{rBC}}}{\mathrm{d}\log m_{\mathrm{rBC}}}$) concentration distributions, the difference in amplitude is proportional to the coating mass at a particular rBC particle mass. This figure shows a trend of smaller particles having a higher coating ratio compared to larger particles. This is expected and has been observed in particles emitted from gasoline engines (Momenimovahed and Olfert, 2015), diesel engines (Ristimäki et al., 2007), diffusion flames (Dickau et al., 2016), and premixed flames (Ghazi and Olfert, 2013).

Finally, for the case with fresh rBC particles added, the two populations of coated and lightly coated particles could be clearly resolved when plotting mass concentration distribution versus total particle mass (Figure A.12c). Viewing the same population as a function of rBC particle mass, the populations can no longer be clearly distinguished because the rBC mass concentration distribution between the coated and uncoated particles have approximately the same median (Figure A.12d).

2.4.4 Mass Concentration as a Function of Time

An SP2 used alone can directly resolve the mass concentration of rBC particles. However the SP2 cannot resolve the total mass concentration of particles containing rBC. The addition of the CPMA allows determination of total mass concentration of particles containing rBC. The total mass concentration and rBC mass concentration can be calculated through integrating the one variable mass concentration distributions,

$$M = \int_0^\infty \frac{\mathrm{d}M}{\mathrm{d}\log m_{\mathrm{p}}}\,\mathrm{d}\log m_{\mathrm{p}} \tag{2.8}$$

$$M_{\mathrm{rBC}} = \int_0^\infty \frac{\mathrm{d}M_{\mathrm{rBC}}}{\mathrm{d}\log m_{\mathrm{p}}}\,\mathrm{d}\log m_{\mathrm{p}}. \tag{2.9}$$

As seen in Figure 2.6, plotting the total mass concentration and rBC mass concen-

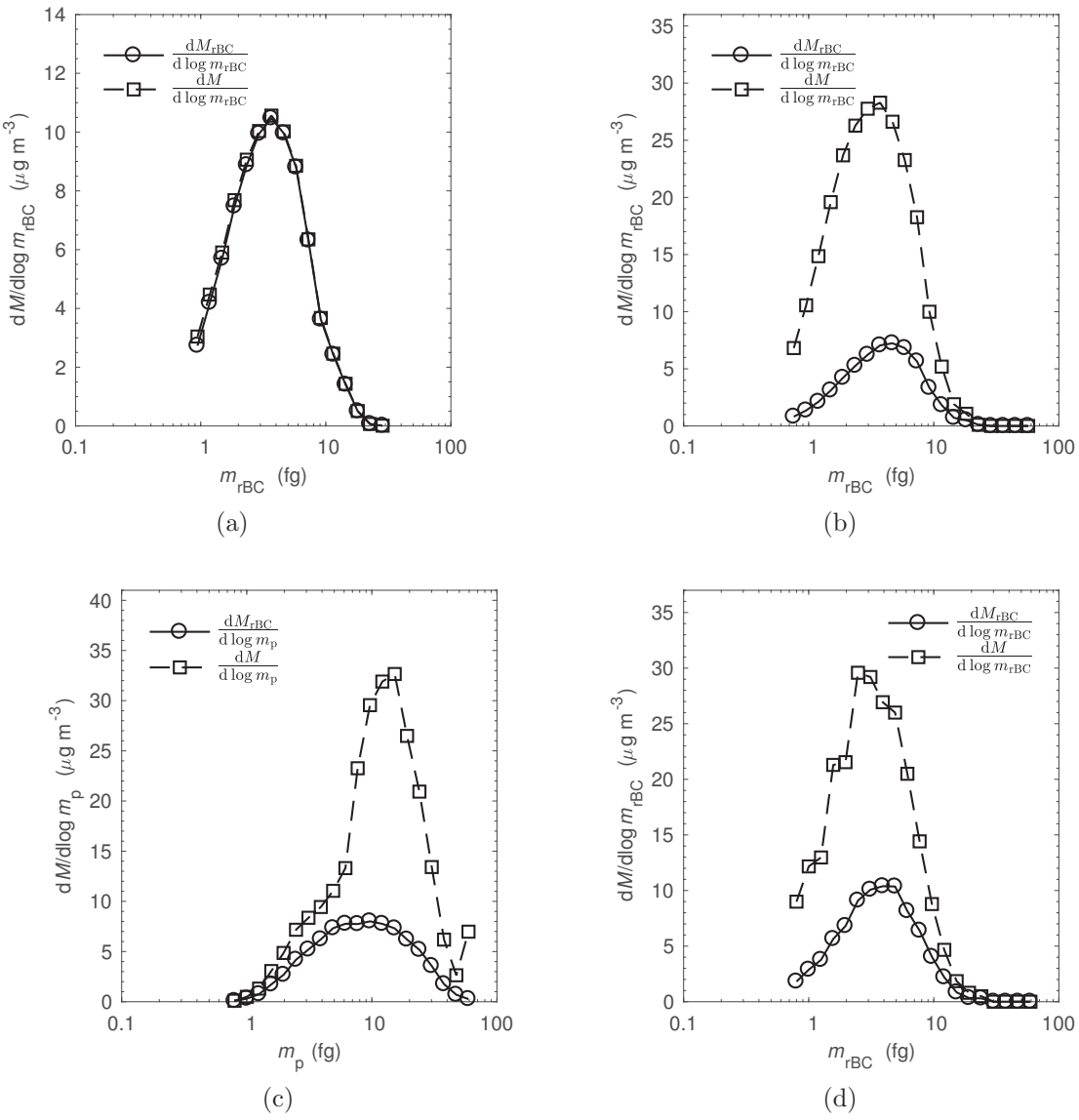

Figure 2.5: Single variable mass distribution functions $\frac{dM}{d\log m}$ for a) uncoated particles as a function of rBC particle mass b) coated particles as a function of rBC particle mass c) mixture of coated and uncoated populations as a function of total particle mass d) mixture of coated and uncoated populations as a function of rBC particle mass

tration as a function of time for the smog chamber experiments shows the total mass concentration of particles is increasing. This is due to growth of organic coating due to photo-oxidation of *p*-xylene. The rBC mass concentration decreases as a function

of time due to diffusion losses to the smog chamber walls. When fresh, uncoated rBC particles are added to the chamber for the final SP2-CPMA scan, the rBC mass concentration increases with an associated increase in total mass concentration as expected. It is expected that the total mass concentration is under-sampled due to the efficiency of the SP2 below masses of 1 fg. Therefore the absolute values of mass concentration are not necessarily accurate, but the trends are useful to demonstrate the inversion method. In smog chamber experiments, all particles contained rBC, and M is close to the actual total mass concentration. Used for ambient sampling, this method would return the total mass concentration of particles containing rBC, different from the total mass concentration of all particles.

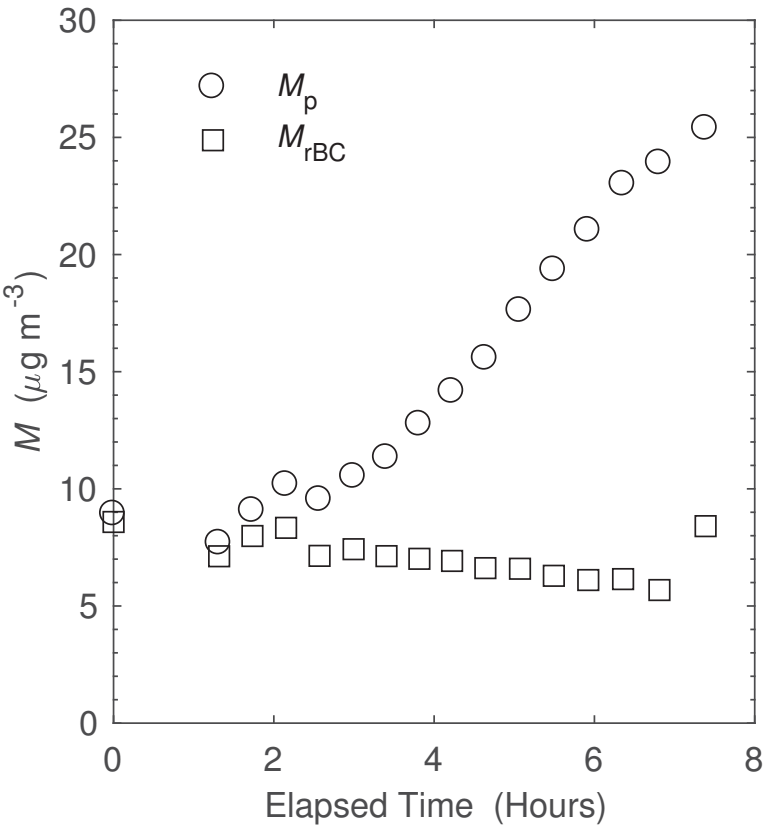

Figure 2.6: Total mass concentration measured by the CPMA-SP2 system as a function of time from when the UV lights in the smog chamber were turned on resulting in coating growth on bare rBC particles via photooxidation with p-xylene

2.5 Conclusion

A CPMA-SP2 inversion algorithm has been developed which calculates a two variable distribution describing particle number concentrations as a function of rBC particle mass and total particle mass. The inversion method solves a Fredholm integral equation using a Twomey algorithm, resulting in a charge-corrected two variable distribution. It was demonstrated that one variable distribution functions, useful to demonstrate coating distribution properties, could be obtained simply from the two variable distributions. The inversion was tested using smog chamber experiments where a significant coating was grown on bare rBC particles over a period of several hours via photo-oxidation with *p*-xylene. It was shown that in a mixed uncoated and coated aerosol the two populations could be clearly distinguished using a two-variable distribution. Similar to SMPS measurements, the CPMA-SP2 inversion makes assumptions about charge state. Additional assumptions include assuming that efficiency correction can effectively account for errors in estimating the mass-mobility relationship and losses in the CPMA. From the two-variable distribution, one-variable mass and number distributions can be calculated through integration, which are a function of rBC or total particle mass. Total particle concentration and mass concentration can be obtained from double integration of the two variable distribution.

References

Bambha, R. P., Dansson, M. A., Schrader, P. E., and Michelsen, H. A. (2013). Effects of volatile coatings on the laser-induced incandescence of soot. *Applied Physics B*, 112(3):343–358.

Bond, T. C., Doherty, S. J., Fahey, D. W., Forster, P. M., Berntsen, T., Deangelo, B. J., Flanner, M. G., Ghan, S., Karcher, B., Koch, D., Kinne, S., Kondo, Y., Quinn, P. K., Sarofim, M. C., Schultz, M. G., Schulz, M., Venkataraman, C., Zhang, H., Zhang, S., Bellouin, N., Guttikunda, S. K., Hopke, P. K., Jacobson, M. Z., Kaiser, J. W., Klimont, Z., Lohmann, U., Schwarz, J. P., Shindell, D., Storelvmo, T., Warren, S. G., and Zender, C. S. (2013). Bounding the role of black carbon in the climate system: A scientific assessment. *Journal of Geophysical Research Atmospheres*, 118(11):5380–5552.

Collins, D. R., Flagan, R. C., and Seinfeld, J. H. (2002). Improved inversion of scanning dma data. *Aerosol Science & Technology*, 36(1):1–9.

Dickau, M., Olfert, J., Stettler, M. E. J., Boies, A., Momenimovahed, A., Thomson, K., Smallwood, G., and Johnson, M. (2016). Methodology for quantifying the volatile mixing state of an aerosol. *Aerosol Science and Technology*, 50(8):759–772.

Gao, R., Schwarz, J., Kelly, K., Fahey, D., Watts, L., Thompson, T., Spackman, J., Slowik, J., Cross, E., Han, J.-H., et al. (2007). A novel method for estimat-

ing light-scattering properties of soot aerosols using a modified single-particle soot photometer. *Aerosol Science and Technology*, 41(2):125–135.

Ghazi, R. and Olfert, J. S. (2013). Coating Mass Dependence of Soot Aggregate Restructuring due to Coatings of Oleic Acid and Dioctyl Sebacate. *Aerosol Science and Technology*, 47(2):192–200.

Gopalakrishnan, R., McMurry, P. H., and Christopher J. Hogan, J. (2015). The Bipolar Diffusion Charging of Nanoparticles: A Review and Development of Approaches for Non-Spherical Particles. *Aerosol Science and Technology*, 49(12):1181–1194.

Hagen, D. E. and Alofs, D. J. (1983). Linear Inversion Method to Obtain Aerosol Size Distributions from Measurements with a Differential Mobility Analyzer. *Aerosol Science and Technology*, 2(4):465–475.

Kulkarni, P., Baron, P. A., and Willeke, K. (2011). *Aerosol measurement: principles, techniques, and applications*. John Wiley & Sons.

Laborde, M., Schnaiter, M., Linke, C., Saathoff, H., Naumann, K.-H., Möhler, O., Berlenz, S., Wagner, U., Taylor, J. W., Liu, D., Flynn, M., Allan, J. D., Coe, H., Heimerl, K., Dahlkötter, F., Weinzierl, B., Wollny, A. G., Zanatta, M., Cozic, J., Laj, P., Hitzenberger, R., Schwarz, J. P., and Gysel, M. (2012). Single Particle Soot Photometer intercomparison at the AIDA chamber. *Atmospheric Measurement Techniques*, 5(12):3077–3097.

Liu, D., Whitehead, J., Alfarra, M. R., Reyes-Villegas, E., Spracklen, D. V., Reddington, C. L., Kong, S., Williams, P. I., Ting, Y.-C., Haslett, S., Taylor, J. W., Flynn, M. J., Morgan, W. T., McFiggans, G., Coe, H., and Allan, J. D. (2017). Black-carbon absorption enhancement in the atmosphere determined by particle mixing state. *Nature Geosci*, 10(3):184–188.

Maricq, M. M. (2007). Chemical characterization of particulate emissions from diesel engines: A review. *Journal of Aerosol Science*, 38(11):1079–1118.

Markowski, G. R. (1987). Improving Twomey's algorithm for inversion of aerosol measurement data. *Aerosol science and technology*, 7(2):127–141.

McMeeking, G. R., Hamburger, T., Liu, D., Flynn, M., Morgan, W. T., Northway, M., Highwood, E. J., Krejci, R., Allan, J. D., Minikin, A., and Coe, H. (2010). Black carbon measurements in the boundary layer over western and northern Europe. *Atmospheric Chemistry and Physics*, 10(19):9393–9414.

McMeeking, G. R., Morgan, W. T., Flynn, M., Highwood, E. J., Turnbull, K., Haywood, J., and Coe, H. (2011). Black carbon aerosol mixing state, organic aerosols and aerosol optical properties over the United Kingdom. *Atmospheric Chemistry and Physics*, 11(17):9037–9052.

Menon, S., Hansen, J., Nazarenko, L., and Luo, Y. (2002). Climate effects of black carbon aerosols in china and india. *Science*, 297(5590):2250–2253.

Momenimovahed, A. and Olfert, J. S. (2015). Effective Density and Volatility of Particles Emitted from Gasoline Direct Injection Vehicles and Implications for Particle Mass Measurement. *Aerosol Science and Technology*, 49(11):1051–1062.

Moosmüller, H., Chakrabarty, R. K., and Arnott, W. P. (2009). Aerosol light absorption and its measurement: A review . *Journal of Quantitative Spectroscopy and Radiative Transfer*, 110(11):844 – 878.

Moteki, N. and Kondo, Y. (2007). Effects of Mixing State on Black Carbon Measurements by Laser-Induced Incandescence. *Aerosol Science and Technology*, 41(4):398–417.

Moteki, N. and Kondo, Y. (2010). Dependence of Laser-Induced Incandescence on Physical Properties of Black Carbon Aerosols: Measurements and Theoretical Interpretation. *Aerosol Science and Technology*, 44(8):663–675.

Olfert, J. S. and Collings, N. (2005). New method for particle mass classificationthe Couette centrifugal particle mass analyzer . *Journal of Aerosol Science*, 36(11):1338 – 1352.

Parsons, M. T., Sydoryk, I., Lim, A., McIntyre, T. J., Tulip, J., Jäger, W., and McDonald, K. (2011). Real-time monitoring of benzene, toluene, and p-xylene in a photoreaction chamber with a tunable mid-infrared laser and ultraviolet differential optical absorption spectroscopy. *Applied optics*, 50(4):A90–A99.

Ramanathan, V. and Carmichael, G. (2008). Global and regional climate changes due to black carbon. *Nature geoscience*, 1(4):221–227.

Rawat, V. K., Buckley, D. T., Kimoto, S., Lee, M. H., Fukushima, N., and Hogan, C. J. (2016). Two dimensional size-mass distribution function inversion from differential mobility analyzer-aerosol particle mass analyzer (DMA-APM) measurements. *Journal of Aerosol Science*, 92:70–82.

Riemer, N., Vogel, H., and Vogel, B. (2004). Soot aging time scales in polluted regions during day and night. *Atmospheric Chemistry and Physics*, 4(7):1885–1893.

Ristimäki, J., Vaaraslahti, K., Lappi, M., and Keskinen, J. (2007). Hydrocarbon condensation in heavy-duty diesel exhaust. *Environmental science & technology*, 41(18):6397–6402.

Ruiz, P. A., Lawrence, J. E., Ferguson, S. T., Wolfson, J. M., and Koutrakis, P. (2006). A counter-current parallel-plate membrane denuder for the non-specific removal of trace gases. *Environmental science & technology*, 40(16):5058–5063.

Schnaiter, M., Linke, C., Mhler, O., Naumann, K.-H., Saathoff, H., Wagner, R., Schurath, U., and Wehner, B. (2005). Absorption amplification of black carbon internally mixed with secondary organic aerosol. *Journal of Geophysical Research: Atmospheres*, 110(D19):n/an/a.

Schwarz, J. P., Spackman, J. R., Fahey, D. W., Gao, R. S., Lohmann, U., Stier, P., Watts, L. A., Thomson, D. S., Lack, D. A., Pfister, L., Mahoney, M. J., Baumgardner, D., Wilson, J. C., and Reeves, J. M. (2008). Coatings and their enhancement of black carbon light absorption in the tropical atmosphere. *Journal of Geophysical Research: Atmospheres*, 113(D3):n/an/a.

Sedlacek, A. J., Lewis, E. R., Kleinman, L., Xu, J., and Zhang, Q. (2012). Determination of and evidence for non-core-shell structure of particles containing black carbon using the Single-Particle Soot Photometer (SP2). *Geophysical Research Letters*, 39(6):n/an/a.

Shiraiwa, M., Kondo, Y., Moteki, N., Takegawa, N., Miyazaki, Y., and Blake, D. R. (2007). Evolution of mixing state of black carbon in polluted air from Tokyo. *Geophysical Research Letters*, 34(16):n/an/a.

Slowik, J. G., Cross, E. S., Han, J.-H., Davidovits, P., Onasch, T. B., Jayne, J. T., Williams, L. R., Canagaratna, M. R., Worsnop, D. R., Chakrabarty, R. K., Moosmller, H., Arnott, W. P., Schwarz, J. P., Gao, R.-S., Fahey, D. W., Kok, G. L., Petzold, A., Moosmüller, H., Arnott, W. P., Schwarz, J. P., Gao, R.-S., Fahey, D. W., Kok, G. L., and Petzold, A. (2007). An Inter-Comparison of Instruments Measuring Black Carbon Content of Soot Particles. *Aerosol Science and Technology*, 41(3):295–314.

Stephens, M., Turner, N., and Sandberg, J. (2003). Particle identification by laser-induced incandescence in a solid-state laser cavity. *Appl. Opt.*, 42(19):3726–3736.

Stolzenburg, M. R. and McMurry, P. H. (2008). Equations Governing Single and Tandem DMA Configurations and a New Lognormal Approximation to the Transfer Function. *Aerosol Science and Technology*, 42(6):421–432.

Twomey, S. (1975). Comparison of constrained linear inversion and an iterative nonlinear algorithm applied to the indirect estimation of particle size distributions. *Journal of Computational Physics*, 18(2):188 – 200.

Wang, S. C. and Flagan, R. C. (1990). Scanning electrical mobility spectrometer. *Aerosol Science and Technology*, 13(2):230–240.

Wiedensohler, A. (1988). An approximation of the bipolar charge distribution for particles in the submicron size range. *Journal of Aerosol Science*, 19(3):387 – 389.

Chapter 3

Application of the CPMA-SP2 inversion to real world measurements

3.1 Application to real-world rBC particles

Chapter 2 has demonstrated the CPMA-SP2 inversion works for narrow distributions of uncoated, coated, and mixed populations of rBC aerosols. Now the inversion is applied to real-world data which was gathered via a 20 day CPMA-SP2 field campaign by Manchester University at the Chinese Academy of Sciences in Beijing, China. Manchester University shared their data for use in the inversion.

Beijing was chosen for an air quality study because of high levels of BC pollution. As seen in Chapter 1, eastern Asia accounts for a significant proportion of global anthropogenic BC emissions, and China alone may account for approximately 20% of the global total. Although such estimation has a large error, it is still clear China produces a significant proportion of global BC emissions. High error in these measurements are mainly due to lack of government statistics, significant and remote rural population, and relatively few direct measurements (Bond et al., 2004; Ni et al., 2014). The city of Beijing has high average levels of air pollution, including high concentrations of atmospheric BC particles, making it an ideal place for air quality studies. Beijing has a higher mean BC mass concentration of 8.7-10 μg m^{-3}, com-

pared to some European and North American cities such as: Barcelona (2.98 μg m^{-3}), St. Louis (0.71-1.75 μg m^{-3}), Toronto (0-6 μg m^{-3}), or Zürich (1.66 μg m^{-3}) (Ramachandran and Rajesh, 2007). Like global estimates, mean BC mass concentration in a city probably has a large error associated with it, however it is clear that Beijing is relatively more polluted than many major cities, and is a good place to test a novel BC measurement method.

The experimental setup is shown in Figure 3.1. Going downstream, the experimental setup consisted of an inlet port, a neutralizer, a CPMA, and then a SP2. The SP2 was calibrated upon arrival with the CPMA. During CPMA-SP2 sampling, a LABVIEW program (National Instruments, USA) was used to control the CPMA, and CPMA scans were started every half an hour, with each scan lasting approximately 16 minutes. The program additionally recorded CPMA data, including rotational speed, voltage, and time. The SP2 continuously recorded the mass of rBC in each individual particle and drew a flowrate of 1.61 L min^{-1}, therefore the flowrate through the CPMA was also 1.61 L min^{-1}. Unfortunately, due to technical difficulties, the ambient concentration of rBC was not measured directly with the SP2 after every CPMA-SP2 scan (*i.e.* no measurements were conducted without the CPMA upstream). However, in between CPMA scans there were periods of approximately 14 minutes where the SP2 recorded data with the CPMA off, meaning the CPMA was not rotating and classifying particles. Although it would be ideal to completely bypass the CPMA for correction of the two variable distribution, using $\bar{\epsilon}$, it is also reasonable to use data with the CPMA off to calculate the correction factor, $\bar{\epsilon}$. This will not completely characterize the rotational losses in the CPMA, but will allow correction of assumed particle mobility. Therefore, the amplitude of the one and two variable distributions will have some systemic error, but the shape is still representative of the actual rBC particle distributions. Considering the purpose of this chapter is to demonstrate the CPMA-SP2 inversion works on real-world data, the error in

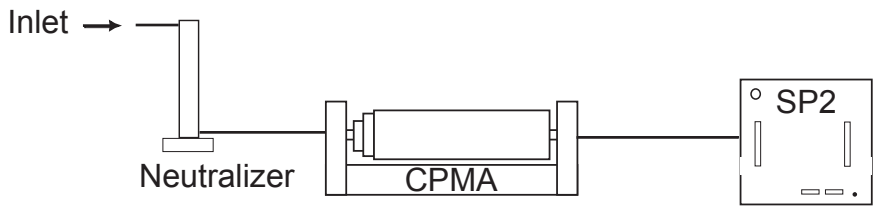

Figure 3.1: Experimental setup for the CPMA-SP2 field measurement campaign

amplitude of the distributions are acceptable.

3.2 Comparison of high, medium, and low pollution days

A vast quantity of data was gathered from the approximately 20 day field campaign in Beijing. From this data, three specific CPMA-SP2 scans were chosen to demonstrate the inversion. The cases were chosen based on ambient pollution, and had either high, medium, and low pollution levels, quantified by ambient rBC concentrations and subjective observations. The terms "high," "medium," and "low" refer to the total number concentration of rBC particles. The data from each case was processed using the inversion with smoothing, and the two variable distribution from the cases are seen in Figure 3.2. The two variable distribution can reveal information about the rBC population immediately by visual inspection, and an analysis is provided for each case.

In the low pollution case (Figure 3.2a), the particle distribution exists slightly offset from the one to one line. This indicates the particles are coated, and the distribution is more broad than laboratory experiments described in Chapter 2. The broader distribution reflects the fact that rBC in the real world is released from different sources at different times. For example, rBC particles emitted from biomass burning may have different coating mass than from diesel engines. Additionally, since coating acquisition in the atmosphere is time-dependent, then particles emitted at different times may acquire different quantities of coating mass. The data from

the low pollution case is relatively noisy, this is because of poor counting statistics, if more particles were counted at each CPMA setpoint the results would improve. For the medium pollution case (Figure 3.2b), the number concentration is higher than in the low pollution case. The main population of particles are more heavily coated, as seen by shifts towards higher total particle masses. The two variable distribution for the high pollution case (Figure 3.2c) reveals two distinct populations of rBC particles. The first is seen by the red pixels at high total particle masses, between approximately 10-15 fg. The second is represented by the green pixels near the one to one line below total particle masses of 4 fg. It is clear from observation the second population along the one to one line is more lightly coated than the first population, which is heavily coated. The implication of particles with a larger coating mass is the lensing effect increases, and thus absorption. Therefore these more heavily coated particles will have a more significant radiative forcing effect than similar uncoated or lightly coated particles.

It appears the population of heavily coated particles extends beyond the range of the CPMA-SP2 scan for the high pollution case. Therefore, the CPMA scan range should have been extended to above 15 fg and as a result the correction factor, $\bar{\epsilon}$, will have some additional error. When the CPMA is off, the SP2 will still measure a significant population of particles with a higher total mass than 15 fg, and some or most of these particles will have a rBC mass less than 15 fg. Therefore these particles of total mass greater than 15 fg will be present in direct SP2 measurement, but not CPMA-SP2 measurement. There is no way to correct for this error besides re-doing the experiment, since SP2 only measurement gives no information on total particle mass. This mistake in CPMA range was repeated for all instances of high pollution, meaning there are no CPMA-SP2 scans where the range is properly set. This error in the correction factor is regrettable, however, the purpose of this section is to demonstrate the inversion works on real world, so an error in amplitude is

acceptable.

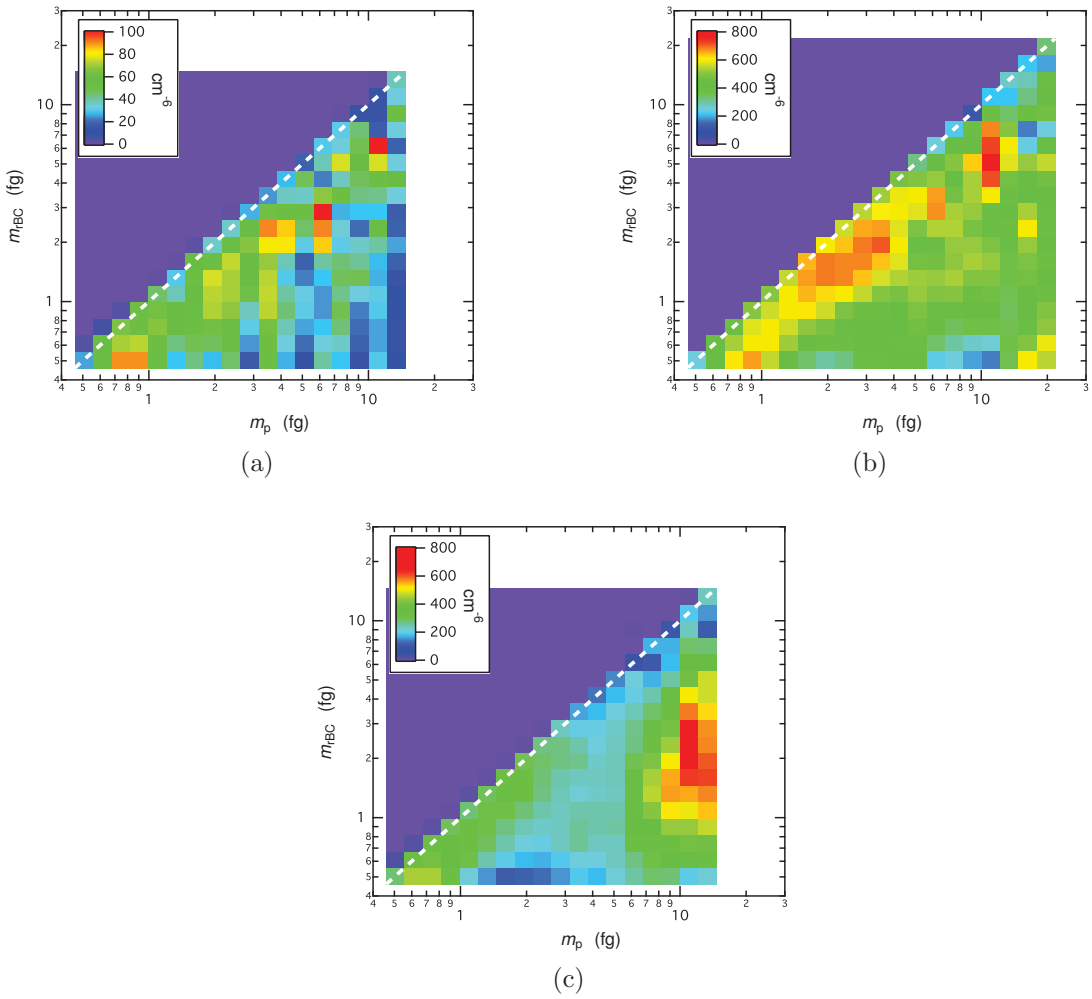

Figure 3.2: Two variable number concentration distribution as a function of both total and rBC particle mass from a) November 22$^{\text{nd}}$ at midnight (low pollution case) b) November 18$^{\text{th}}$ at 7pm (medium pollution case) c) December 3$^{\text{rd}}$ at 7pm (high pollution case) all in 2016.

The one variable number concentration distribution for each of the three cases are shown in Figure 3.3. From the two variable distributions it was observed the populations of rBC particles are all, on average, coated with non-rBC material. This is also observed in the one variable number concentration distributions because the median of $\dfrac{\mathrm{d}N}{\mathrm{d}\log m_{\mathrm{p}}}$ is greater than $\dfrac{\mathrm{d}N}{\mathrm{d}\log m_{\mathrm{rBC}}}$, indicating the populations are coated. By examining the one variable number concentration distribution for the highly polluted

case (Figure 3.3c), the two populations observed from the two variable distribution are visible. The inflection point at approximately 4 fg for $\frac{\mathrm{d}N}{\mathrm{d}\log m_{\mathrm{p}}}$ indicates the presence of the second, more heavily coated population.

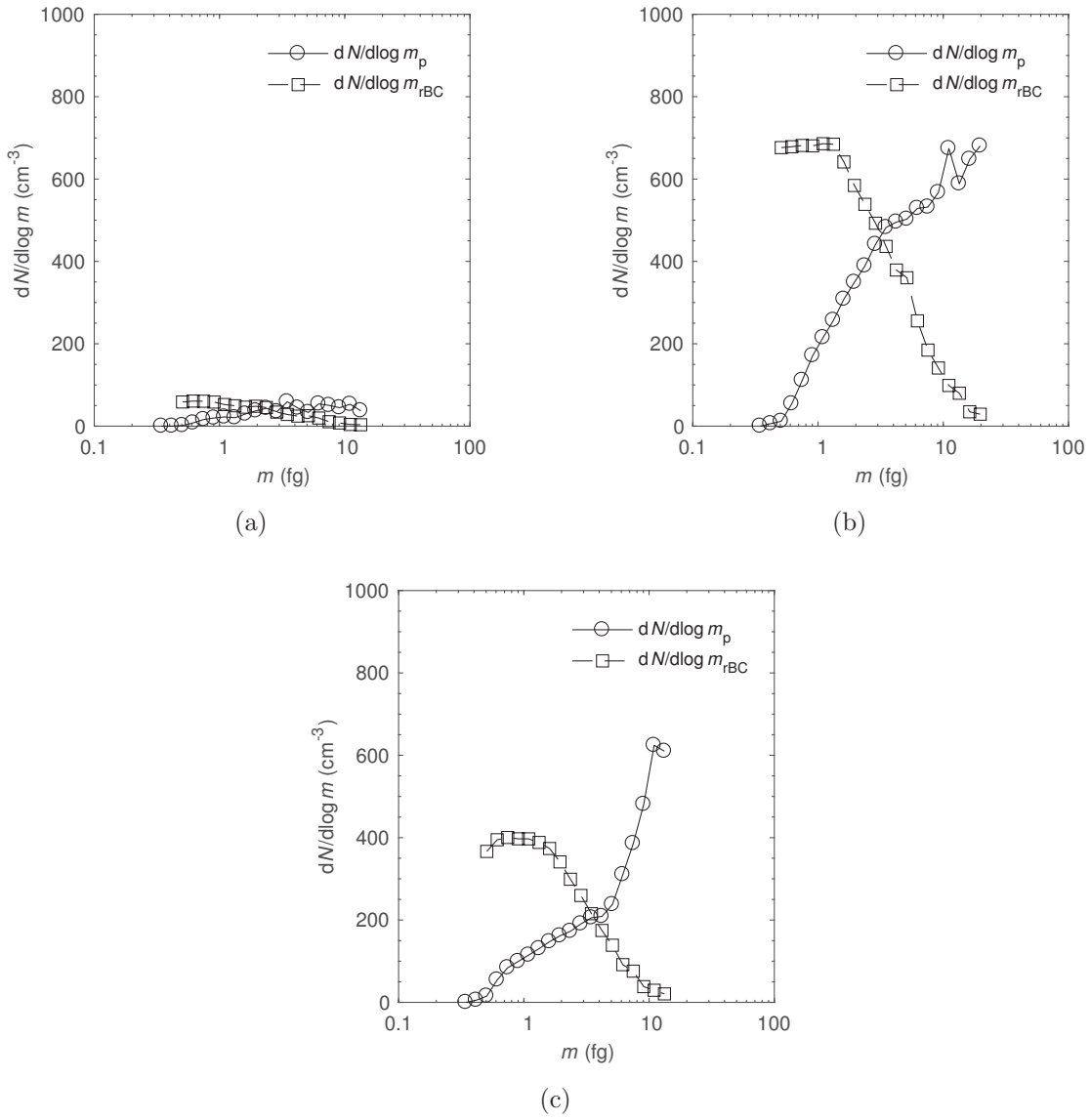

Figure 3.3: One variable number concentration distribution from a) November 22$^{\mathrm{nd}}$ at midnight (low pollution case) b) November 18$^{\mathrm{th}}$ at 7pm (medium pollution case) c) December 3$^{\mathrm{rd}}$ at 7pm (high pollution case) all in 2016.

The one variable mass concentration distributions as a function of rBC particle mass are shown in Figure 3.4. Observing the mass concentration distribution as a

function of m_{rBC} for the high pollution case (Figure 3.4c), the distribution $\frac{\mathrm{d}M}{\mathrm{d}\log m_{\mathrm{rBC}}}$ has a higher magnitude than $\frac{\mathrm{d}M_{\mathrm{rBC}}}{\mathrm{d}\log m_{\mathrm{rBC}}}$. The difference in amplitude between the two distributions is the average coating mass concentration on a given rBC particle mass. The particles with a smaller rBC mass are more heavily coated than larger rBC particles, which is to be expected. The trend of smaller rBC particles having a higher rBC particle mass is also observed for the medium (Figure 3.4b) and low (Figure 3.4a) pollution case. For the low pollution case the amplitude of both mass distributions are lower, and the ratio of $\frac{\mathrm{d}M}{\mathrm{d}\log m_{\mathrm{rBC}}}$ to $\frac{\mathrm{d}M_{\mathrm{rBC}}}{\mathrm{d}\log m_{\mathrm{rBC}}}$ is lower than the medium and high pollution cases. In other words, the ratio of non-rBC to rBC for a particular rBC mass is lower for the low pollution case than for the high and medium pollution case.

The mass concentration distribution as a function of total particle mass is shown in Figure 3.5. Despite smoothing, the low pollution distribution (Figure 3.5a) is noisy, resulting from the low rBC particle concentrations. Further smoothing would broaden the distribution unrealistically, and therefore conducting further smoothing iterations is not desirable. As expected, particles of higher total particle mass had on average both a higher rBC mass and non-rBC mass for all three cases.

3.3 Conclusion

The three cases above are a small sample of the approximately 400 CPMA-SP2 scans taken during the China field campaign. Three representative cases were shown where the rBC number concentration differed. The two variable distribution showed coating mass distributions for the populations of measured particles, and all three two variable number concentration distributions had a broader distribution than that seen in the lab.. The high pollution case is especially interesting, showing a population of heavily coated particles and a population of lightly coated particles. The difference in coating

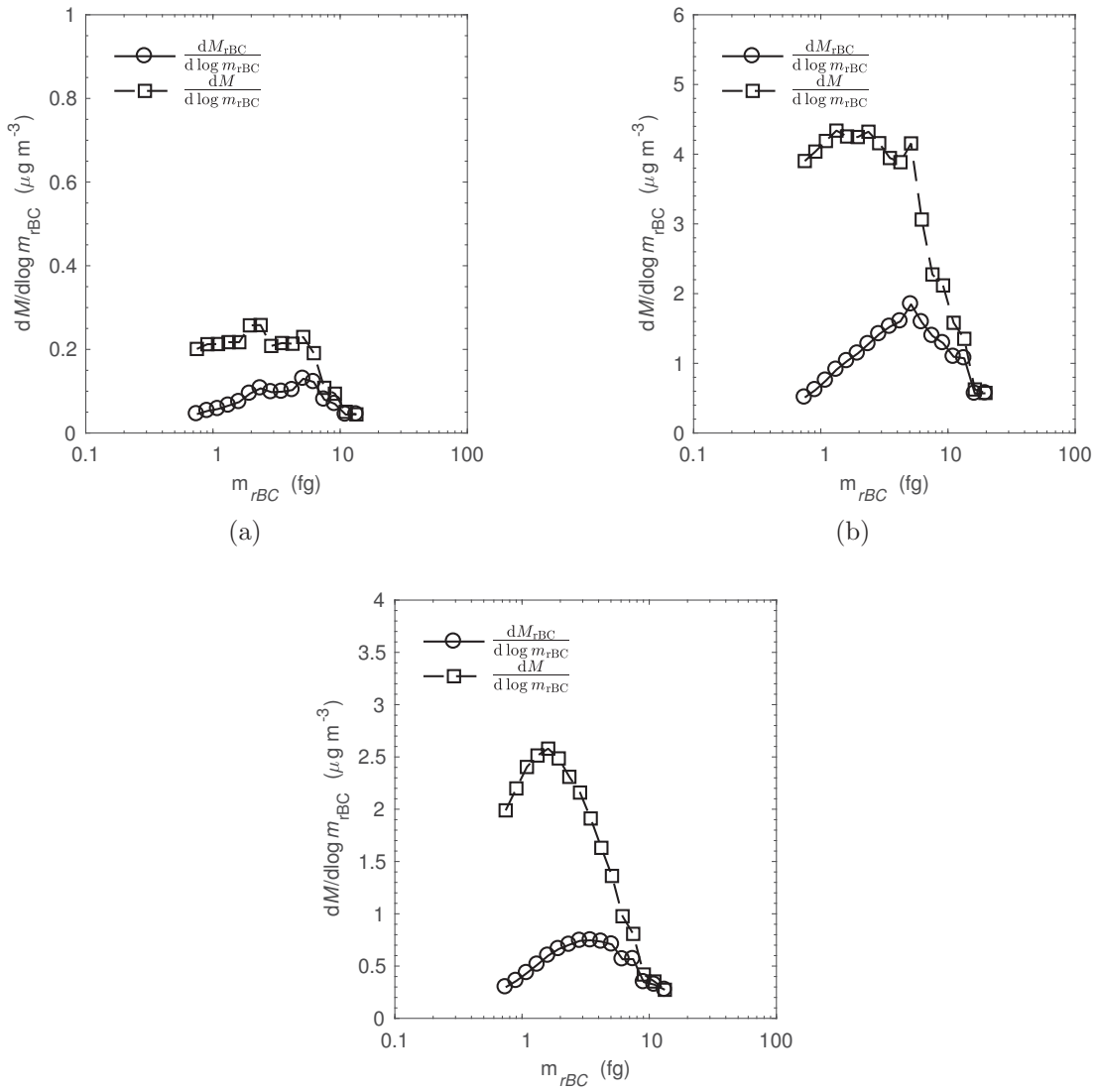

Figure 3.4: Mass concentration distribution as a function of rBC mass from a) November 22$^{\text{nd}}$ at midnight (low pollution case) b) November 18$^{\text{th}}$ at 7pm (medium pollution case) c) December 3$^{\text{rd}}$ at 7pm (high pollution case) all in 2016.

could be from two reasons: i) the rBC particles were emitted from different sources and therefore have different initial coating masses, or ii) they have different residence times in the atmosphere allowing more time for coating acquisition. Particle populations with a higher coating mass are expected to have higher radiative forcing than particles populations of the same rBC with a lower coating mass due to lensing effects. Thus,

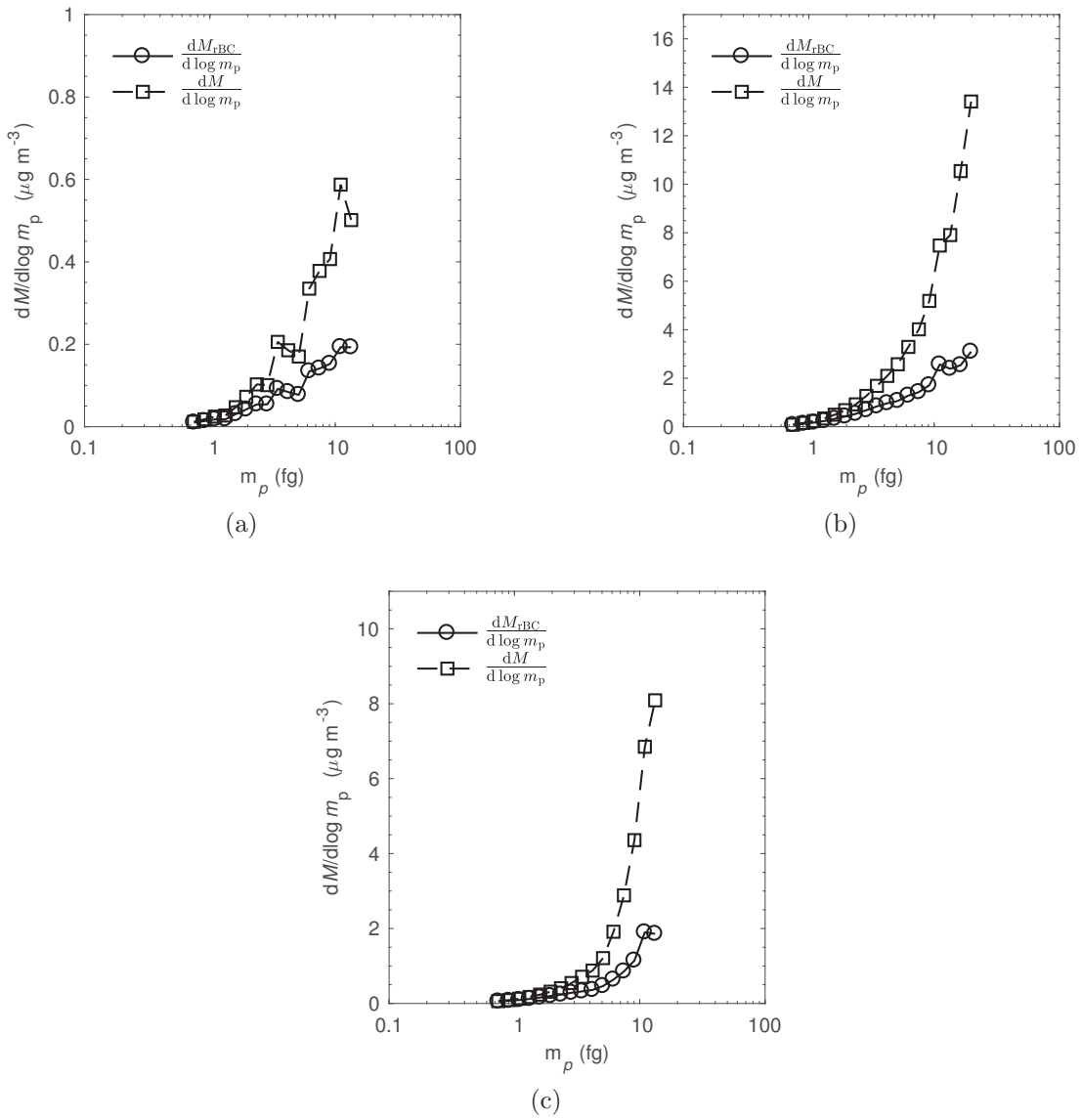

Figure 3.5: Mass concentration distribution as a function of total particle mass from a) November 22$^{\text{nd}}$ at midnight (low pollution case) b) November 18$^{\text{th}}$ at 7pm (medium pollution case) c) December 3$^{\text{rd}}$ at 7pm (high pollution case) all in 2016.

the two variable distribution can identify these populations. The next step in this project is to develop software which can be given to atmospheric scientists.

References

Bond, T. C., Streets, D. G., Yarber, K. F., Nelson, S. M., Woo, J.-H., and Klimont, Z. (2004). A technology-based global inventory of black and organic carbon emissions from combustion. *Journal of Geophysical Research: Atmospheres*, 109(D14).

Ni, M., Huang, J., Lu, S., Li, X., Yan, J., and Cen, K. (2014). A review on black carbon emissions, worldwide and in China. *Chemosphere*, 107:83–93.

Ramachandran, S. and Rajesh, T. A. (2007). Black carbon aerosol mass concentrations over Ahmedabad, an urban location in western India: comparison with urban sites in Asia, Europe, Canada, and the United States. *Journal of Geophysical Research: Atmospheres*, 112(D6).

Chapter 4

Conclusion

Black carbon is a significant driver of climate change, and the acquisition of coatings amplifies its warming effects. For scientists to further understand the negative effects of BC on climate, new tools are needed such as developed in this thesis. The previous chapters described a new method of quantifying the coating mass characteristics of atmospheric rBC particles. This method uses a CPMA and SP2, coupled with a novel inversion algorithm. This inversion is an improvement on SP2 only, SP-AMS, and DMA-CPMA methods, because the CPMA classifies particles by total mass. Inversion of CPMA-SP2 data is required to account for the CPMA transfer function and multiply charged particles. The result of CPMA-SP2 inversion is a two variable number concentration distribution which is a function of rBC mass and total particle mass. Integration of the distribution results in one variable mass and number concentration distributions, and total rBC mass concentration and total particle mass concentration of particles containing rBC.

The smog chamber experiments showed the inversion can resolve distributions of rBC particle populations with no coating, coating, and a mixture of coated and uncoated particles. The two variable distribution for uncoated particles showed all particles existing along the one-to-one line, while for coated particles the distribution shifted towards higher total particle mass. When fresh, uncoated rBC particles were

injected into the chamber, the two populations could be clearly resolved. It was shown that changing the assumption of rBC particle mobility did not affect the final results. After verification using the smog chamber, the inversion was applied to data gathered using an CPMA-SP2 from Shanghai, China. Three sample data sets were shown, roughly correlating to a low, medium, and high pollution time-frame. The distribution of rBC particles could be clearly resolved using the two variable distribution. For the low and medium pollution days, rBC particles were lightly coated, and for the high pollution day, the rBC particles were heavily coated.

The inversion was tested on real world data from ambient rBC measurements using a CPMA-SP2 taken in Beijing, China. Over 400 CPMA-SP2 scans over approximately 20 days were taken during the field campaign, and the inversion was applied to 3 representative cases with the results presented in Chapter 3. From analyzing the two variable number concentration distribution, the low and medium ambient pollution cases showed a single population of rBC particles which were relatively lightly coated. The high ambient pollution case showed two distinct populations, which were also resolved on the one variable mass and number concentration distributions. Smoothing during inversion was required because the distributions were very broad. The broad distributions were a result of rBC being emitted from different sources and having varying residence times in the atmosphere. Applying the inversion to real world data showed the utility of the method developed in this thesis.

Chapters 2 and 3 showed the CPMA-SP2 inversion method works, and now it requires optimization and packaging so it can be used by the atmospheric science community. Firstly, packaging the software into a commercially available package is required. The CPMA manufacturer, Cambustion is interested in developing this type of package. This package should also include using the SP2 scattering and incandescence channel to remove neutral particles needs to be added to existing SP2 signal processing toolkits. Secondly, a labview program to automate the CPMA-SP2

data gathering process should be developed. A partial automation program has been developed by the Mancunians. An automated valve is needed to remove manual valve switching for CPMA bypass scans.

Two future research projects could build on this work. Firstly, diameter information using the SP2 scattering channel can be investigated when the scattering channel gets more sensitive. The latest generation SP2 has an incandescence particle size range of 70-500 nm mass-equivalent diameter assuming rBC density of 1.8 g cm^{-3}, while the scattering channel has an optical scattering diameter range of 200-430 nm. Relating optical diameter of a fractal aggregate to a mass-equivalent diameter is problematic, however once the scattering detection range gets close to the incandescence detection range, further research can be conducted. For instance a two variable distribution could be constructed for optical scattering diameter versus total particle mass. Lastly, a similar inversion technique could be used for CPMA-DMA data, to give a two variable number concentration as a function of total particle mass and mobility diameter.

References

Andreae, M. and Gelencsér, A. (2006). Black carbon or brown carbon? the nature of light-absorbing carbonaceous aerosols. *Atmospheric Chemistry and Physics*, 6(10):3131–3148.

Bambha, R. P., Dansson, M. A., Schrader, P. E., and Michelsen, H. A. (2013). Effects of volatile coatings on the laser-induced incandescence of soot. *Applied Physics B*, 112(3):343–358.

Biswas, S., Verma, V., Schauer, J. J., Cassee, F. R., Cho, A. K., and Sioutas, C. (2009). Oxidative potential of semi-volatile and non volatile particulate matter (PM) from heavy-duty vehicles retrofitted with emission control technologies. *Environmental science & technology*, 43(10):3905–3912.

Bond, T. C. and Bergstrom, R. W. (2006). Light absorption by carbonaceous particles: An investigative review. *Aerosol science and technology*, 40(1):27–67.

Bond, T. C., Doherty, S. J., Fahey, D. W., Forster, P. M., Berntsen, T., Deangelo, B. J., Flanner, M. G., Ghan, S., Karcher, B., Koch, D., Kinne, S., Kondo, Y., Quinn, P. K., Sarofim, M. C., Schultz, M. G., Schulz, M., Venkataraman, C., Zhang, H., Zhang, S., Bellouin, N., Guttikunda, S. K., Hopke, P. K., Jacobson, M. Z., Kaiser, J. W., Klimont, Z., Lohmann, U., Schwarz, J. P., Shindell, D., Storelvmo, T., Warren, S. G., and Zender, C. S. (2013). Bounding the role of black

carbon in the climate system: A scientific assessment. *Journal of Geophysical Research Atmospheres*, 118(11):5380–5552.

Bond, T. C., Streets, D. G., Yarber, K. F., Nelson, S. M., Woo, J.-H., and Klimont, Z. (2004). A technology-based global inventory of black and organic carbon emissions from combustion. *Journal of Geophysical Research: Atmospheres*, 109(D14).

Cakmak, S., Dales, R. E., Gultekin, T., Vidal, C. B., Farnendaz, M., Rubio, M. A., and Oyola, P. (2009a). Components of particulate air pollution and emergency department visits in chile. *Archives of environmental & occupational health*, 64(3):148–155.

Cakmak, S., Dales, R. E., and Vida, C. B. (2009b). Components of particulate air pollution and mortality in chile. *International Journal of Occupational and Environmental Health*, 15(2):152–158.

Cappa, C. D., Onasch, T. B., Massoli, P., Worsnop, D. R., Bates, T. S., Cross, E. S., Davidovits, P., Hakala, J., Hayden, K. L., Jobson, B. T., and others (2012). Radiative absorption enhancements due to the mixing state of atmospheric black carbon. *Science*, 337(6098):1078–1081.

Collins, D. R., Flagan, R. C., and Seinfeld, J. H. (2002). Improved inversion of scanning dma data. *Aerosol Science & Technology*, 36(1):1–9.

Dastanpour, R. and Rogak, S. N. (2014). Observations of a Correlation Between Primary Particle and Aggregate Size for Soot Particles. *Aerosol Science and Technology*, 48(10):1043–1049.

Davis, D. L. (2002). A look back at the london smog of 1952 and the half century since. *Environmental health perspectives*, 110(12):A734.

DeCarlo, P. F., Slowik, J. G., Worsnop, D. R., Davidovits, P., and Jimenez, J. L. (2004). Particle morphology and density characterization by combined mobility and aerodynamic diameter measurements. Part 1 Theory. *Aerosol Science and Technology*, 38(12):1185–1205.

Dickau, M., Olfert, J., Stettler, M. E. J., Boies, A., Momenimovahed, A., Thomson, K., Smallwood, G., and Johnson, M. (2016). Methodology for quantifying the volatile mixing state of an aerosol. *Aerosol Science and Technology*, 50(8):759–772.

Dusek, U., Frank, G. P., Hildebrandt, L., Curtius, J., Schneider, J., Walter, S., Chand, D., Drewnick, F., Hings, S., Jung, D., Borrmann, S., and Andreae, M. O. (2006). Size matters more than chemistry for cloud-nucleating ability of aerosol particles. *Science*, 312(5778):1375–1378.

Frampton, M. W., Stewart, J. C., Oberdörster, G., Morrow, P. E., Chalupa, D., Pietropaoli, A. P., Frasier, L. M., Speers, D. M., Cox, C., Huang, L.-S., and others (2006). Inhalation of ultrafine particles alters blood leukocyte expression of adhesion molecules in humans. *Environmental Health Perspectives*, pages 51–58.

Gao, R., Schwarz, J., Kelly, K., Fahey, D., Watts, L., Thompson, T., Spackman, J., Slowik, J., Cross, E., Han, J.-H., et al. (2007). A novel method for estimating light-scattering properties of soot aerosols using a modified single-particle soot photometer. *Aerosol Science and Technology*, 41(2):125–135.

Ghazi, R. and Olfert, J. S. (2013). Coating Mass Dependence of Soot Aggregate Restructuring due to Coatings of Oleic Acid and Dioctyl Sebacate. *Aerosol Science and Technology*, 47(2):192–200.

Golub, G. H., Heath, M., and Wahba, G. (1979). Generalized cross-validation as a method for choosing a good ridge parameter. *Technometrics*, 21(2):215–223.

Gong Jr, H., Linn, W. S., Sioutas, C., Terrell, S. L., Clark, K. W., Anderson, K. R., and Terrell, L. L. (2003). Controlled exposures of healthy and asthmatic volunteers to concentrated ambient fine particles in Los Angeles. *Inhalation toxicology*, 15(4):305–325.

Gopalakrishnan, R., McMurry, P. H., and Christopher J. Hogan, J. (2015). The Bipolar Diffusion Charging of Nanoparticles: A Review and Development of Approaches for Non-Spherical Particles. *Aerosol Science and Technology*, 49(12):1181–1194.

Graves, B. M., Koch, C. R., and Olfert, J. S. (2016). Morphology and Volatility of Particulate Matter Emitted from a Gasoline Direct Injection Engine Fuelled on Gasoline and Ethanol Blends . *Journal of Aerosol Science*, pages –.

Gustafsson, . and Ramanathan, V. (2016). Convergence on climate warming by black carbon aerosols. *Proceedings of the National Academy of Sciences*, 113(16):201603570.

Hagen, D. E. and Alofs, D. J. (1983). Linear Inversion Method to Obtain Aerosol Size Distributions from Measurements with a Differential Mobility Analyzer. *Aerosol Science and Technology*, 2(4):465–475.

Hallquist, M., Wenger, J. C., Baltensperger, U., Rudich, Y., Simpson, D., Claeys, M., Dommen, J., Donahue, N. M., George, C., Goldstein, A. H., and others (2009). The formation, properties and impact of secondary organic aerosol: current and emerging issues. *Atmospheric Chemistry and Physics*, 9(14):5155–5236.

Hansen, P. C. (1992). Analysis of discrete ill-posed problems by means of the L-curve. *SIAM review*, 34(4):561–580.

Hansen, P. C. and OLeary, D. P. (1993). The use of the L-curve in the regularization

of discrete ill-posed problems. *SIAM Journal on Scientific Computing*, 14(6):1487–1503.

Henderson, S. B., Beckerman, B., Jerrett, M., and Brauer, M. (2007). Application of land use regression to estimate long-term concentrations of traffic-related nitrogen oxides and fine particulate matter. *Environmental Science & Technology*, 41(7):2422–2428. PMID: 17438795.

Hinds, W. C. (1999). *Aerosol technology: Properties, behavior, and measurement of airborne particles. 1999*. Wiley: New York.

Jacobson, M. Z. (2001). Strong radiative heating due to the mixing state of black carbon in atmospheric aerosols. *Nature*, 409(6821):695–697.

Janssen, N. A. H., Hoek, G., Simic-Lawson, M., Fischer, P., Van Bree, L., Ten Brink, H., Keuken, M., Atkinson, R. W., Anderson, H. R., Brunekreef, B., and others (2011). Black Carbon as an Additional Indicator of the Adverse Health Effects of Airborne Particles Compared with PMˆ sub 10ˆ and PMˆ sub 2.5ˆ. *Environmental health perspectives*, 119(12):1691.

Jayne, J. T., Leard, D. C., Zhang, X., Davidovits, P., Smith, K. A., Kolb, C. E., and Worsnop, D. R. (2000). Development of an aerosol mass spectrometer for size and composition analysis of submicron particles. *Aerosol Science and Technology*, 33(1-2):49–70.

Kandlikar, M. and Ramachandran, G. (1999). Inverse methods for analysing aerosol spectrometer measurements: a critical review. *Journal of Aerosol Science*, 30(4):413–437.

Knutson, E. O. and Whitby, K. T. (1975). Aerosol classification by electric mobility: apparatus, theory, and applications. *Journal of Aerosol Science*, 6(6):443–451.

Koch, D. and Del Genio, A. (2010). Black carbon semi-direct effects on cloud cover: review and synthesis. *Atmospheric Chemistry and Physics*, 10(16):7685–7696.

Kulkarni, P., Baron, P. A., and Willeke, K. (2011). *Aerosol measurement: principles, techniques, and applications*. John Wiley & Sons.

Laborde, M., Schnaiter, M., Linke, C., Saathoff, H., Naumann, K.-H., Möhler, O., Berlenz, S., Wagner, U., Taylor, J. W., Liu, D., Flynn, M., Allan, J. D., Coe, H., Heimerl, K., Dahlkötter, F., Weinzierl, B., Wollny, A. G., Zanatta, M., Cozic, J., Laj, P., Hitzenberger, R., Schwarz, J. P., and Gysel, M. (2012). Single Particle Soot Photometer intercomparison at the AIDA chamber. *Atmospheric Measurement Techniques*, 5(12):3077–3097.

Lack, D. A. and Cappa, C. D. (2010). Impact of brown and clear carbon on light absorption enhancement, single scatter albedo and absorption wavelength dependence of black carbon. *Atmospheric Chemistry and Physics*, 10(9):4207–4220.

Liu, D., Whitehead, J., Alfarra, M. R., Reyes-Villegas, E., Spracklen, D. V., Reddington, C. L., Kong, S., Williams, P. I., Ting, Y.-C., Haslett, S., Taylor, J. W., Flynn, M. J., Morgan, W. T., McFiggans, G., Coe, H., and Allan, J. D. (2017). Black-carbon absorption enhancement in the atmosphere determined by particle mixing state. *Nature Geosci*, 10(3):184–188.

Maricq, M. M. (2007). Chemical characterization of particulate emissions from diesel engines: A review. *Journal of Aerosol Science*, 38(11):1079–1118.

Markowski, G. R. (1987). Improving Twomey's algorithm for inversion of aerosol measurement data. *Aerosol science and technology*, 7(2):127–141.

McMeeking, G. R., Hamburger, T., Liu, D., Flynn, M., Morgan, W. T., Northway, M., Highwood, E. J., Krejci, R., Allan, J. D., Minikin, A., and Coe, H. (2010). Black

carbon measurements in the boundary layer over western and northern Europe. *Atmospheric Chemistry and Physics*, 10(19):9393–9414.

McMeeking, G. R., Morgan, W. T., Flynn, M., Highwood, E. J., Turnbull, K., Haywood, J., and Coe, H. (2011). Black carbon aerosol mixing state, organic aerosols and aerosol optical properties over the United Kingdom. *Atmospheric Chemistry and Physics*, 11(17):9037–9052.

Menon, S., Hansen, J., Nazarenko, L., and Luo, Y. (2002). Climate effects of black carbon aerosols in china and india. *Science*, 297(5590):2250–2253.

Mills, N. L., Miller, M. R., Lucking, A. J., Beveridge, J., Flint, L., Boere, A. J. F., Fokkens, P. H., Boon, N. A., Sandstrom, T., Blomberg, A., and others (2011). Combustion-derived nanoparticulate induces the adverse vascular effects of diesel exhaust inhalation. *European heart journal*, page ehr195.

Mills, N. L., Robinson, S. D., Fokkens, P. H. B., Leseman, D. L. A. C., Miller, M. R., Anderson, D., Freney, E. J., Heal, M. R., Donovan, R. J., Blomberg, A., and others (2008). Exposure to concentrated ambient particles does not affect vascular function in patients with coronary heart disease. *Environmental health perspectives*, 116(6):709.

Mills, N. L., Törnqvist, H., Robinson, S. D., Gonzalez, M., Darnley, K., MacNee, W., Boon, N. A., Donaldson, K., Blomberg, A., Sandstrom, T., and others (2005). Diesel exhaust inhalation causes vascular dysfunction and impaired endogenous fibrinolysis. *Circulation*, 112(25):3930–3936.

Momenimovahed, A. and Olfert, J. S. (2015). Effective Density and Volatility of Particles Emitted from Gasoline Direct Injection Vehicles and Implications for Particle Mass Measurement. *Aerosol Science and Technology*, 49(11):1051–1062.

Moosmüller, H., Chakrabarty, R. K., and Arnott, W. P. (2009). Aerosol light absorption and its measurement: A review . *Journal of Quantitative Spectroscopy and Radiative Transfer*, 110(11):844 – 878.

Moteki, N. and Kondo, Y. (2007). Effects of Mixing State on Black Carbon Measurements by Laser-Induced Incandescence. *Aerosol Science and Technology*, 41(4):398–417.

Moteki, N. and Kondo, Y. (2010). Dependence of Laser-Induced Incandescence on Physical Properties of Black Carbon Aerosols: Measurements and Theoretical Interpretation. *Aerosol Science and Technology*, 44(8):663–675.

Ni, M., Huang, J., Lu, S., Li, X., Yan, J., and Cen, K. (2014). A review on black carbon emissions, worldwide and in China. *Chemosphere*, 107:83–93.

Olfert, J. S. (2005). A Numerical Calculation of the Transfer Function of the Fluted Centrifugal Particle Mass Analyzer. *Aerosol Science and Technology*, 39(10):1002–1009.

Olfert, J. S. and Collings, N. (2005). New method for particle mass classificationthe Couette centrifugal particle mass analyzer . *Journal of Aerosol Science*, 36(11):1338 – 1352.

Onasch, T. B., Trimborn, A., Fortner, E. C., Jayne, J. T., Kok, G. L., Williams, L. R., Davidovits, P., and Worsnop, D. R. (2012). Soot Particle Aerosol Mass Spectrometer: Development, Validation, and Initial Application. *Aerosol Science and Technology*, 46(7):804–817.

Pachauri, R. K., Meyer, L., Plattner, G.-K., Stocker, T., and others (2015). *IPCC, 2014: Climate Change 2014: Synthesis Report. Contribution of Working Groups*

I, II and III to the Fifth Assessment Report of the Intergovernmental Panel on Climate Change. IPCC.

Parsons, M. T., Sydoryk, I., Lim, A., McIntyre, T. J., Tulip, J., Jäger, W., and McDonald, K. (2011). Real-time monitoring of benzene, toluene, and p-xylene in a photoreaction chamber with a tunable mid-infrared laser and ultraviolet differential optical absorption spectroscopy. *Applied optics*, 50(4):A90–A99.

Petzold, A., Ogren, J. A., Fiebig, M., Laj, P., Li, S.-M., Baltensperger, U., Holzer-Popp, T., Kinne, S., Pappalardo, G., Sugimoto, N., et al. (2013). Recommendations for reporting" black carbon" measurements. *Atmospheric Chemistry and Physics*, 13(16):8365–8379.

Ramachandran, S. and Rajesh, T. A. (2007). Black carbon aerosol mass concentrations over Ahmedabad, an urban location in western India: comparison with urban sites in Asia, Europe, Canada, and the United States. *Journal of Geophysical Research: Atmospheres*, 112(D6).

Ramanathan, V. and Carmichael, G. (2008). Global and regional climate changes due to black carbon. *Nature geoscience*, 1(4):221–227.

Rawat, V. K., Buckley, D. T., Kimoto, S., Lee, M. H., Fukushima, N., and Hogan, C. J. (2016). Two dimensional size-mass distribution function inversion from differential mobility analyzer-aerosol particle mass analyzer (DMA-APM) measurements. *Journal of Aerosol Science*, 92:70–82.

Riddervold, I. S., Bønløkke, J. H., Mølhave, L., Massling, A., Jensen, B., Grønborg, T. K., Bossi, R., Forchhammer, L., Kjærgaard, S. K., and Sigsgaard, T. (2011). Wood smoke in a controlled exposure experiment with human volunteers. *Inhalation toxicology*, 23(5):277–288.

Riemer, N., Vogel, H., and Vogel, B. (2004). Soot aging time scales in polluted regions during day and night. *Atmospheric Chemistry and Physics*, 4(7):1885–1893.

Riemer, N. and West, M. (2013). Quantifying aerosol mixing state with entropy and diversity measures. *Atmospheric Chemistry and Physics*, 13(22):11423–11439.

Ristimäki, J., Vaaraslahti, K., Lappi, M., and Keskinen, J. (2007). Hydrocarbon condensation in heavy-duty diesel exhaust. *Environmental science & technology*, 41(18):6397–6402.

Ruiz, P. A., Lawrence, J. E., Ferguson, S. T., Wolfson, J. M., and Koutrakis, P. (2006). A counter-current parallel-plate membrane denuder for the non-specific removal of trace gases. *Environmental science & technology*, 40(16):5058–5063.

Schnaiter, M., Linke, C., Mhler, O., Naumann, K.-H., Saathoff, H., Wagner, R., Schurath, U., and Wehner, B. (2005). Absorption amplification of black carbon internally mixed with secondary organic aerosol. *Journal of Geophysical Research: Atmospheres*, 110(D19):n/an/a.

Schnitzler, E. G., Dutt, A., Charbonneau, A. M., Olfert, J. S., and Jäger, W. (2014). Soot aggregate restructuring due to coatings of secondary organic aerosol derived from aromatic precursors. *Environmental Science & Technology*, 48(24):14309 – 14316.

Schwarz, J. P., Spackman, J. R., Gao, R. S., Perring, A. E., Cross, E., Onasch, T. B., Ahern, A., Wrobel, W., Davidovits, P., Olfert, J., and others (2010). The detection efficiency of the single particle soot photometer. *Aerosol Science and Technology*, 44(8):612–628.

Sedlacek, A. J., Lewis, E. R., Kleinman, L., Xu, J., and Zhang, Q. (2012). Determination of and evidence for non-core-shell structure of particles containing black

carbon using the Single-Particle Soot Photometer (SP2). *Geophysical Research Letters*, 39(6):n/an/a.

Seinfeld, J. H. and Pandis, S. N. (2016). *Atmospheric chemistry and physics: from air pollution to climate change*. John Wiley & Sons.

Shiraiwa, M., Kondo, Y., Moteki, N., Takegawa, N., Miyazaki, Y., and Blake, D. R. (2007). Evolution of mixing state of black carbon in polluted air from Tokyo. *Geophysical Research Letters*, 34(16):n/an/a.

Slowik, J. G., Cross, E. S., Han, J.-H., Davidovits, P., Onasch, T. B., Jayne, J. T., Williams, L. R., Canagaratna, M. R., Worsnop, D. R., Chakrabarty, R. K., Moosmller, H., Arnott, W. P., Schwarz, J. P., Gao, R.-S., Fahey, D. W., Kok, G. L., Petzold, A., Moosmüller, H., Arnott, W. P., Schwarz, J. P., Gao, R.-S., Fahey, D. W., Kok, G. L., and Petzold, A. (2007). An Inter-Comparison of Instruments Measuring Black Carbon Content of Soot Particles. *Aerosol Science and Technology*, 41(3):295–314.

Solomon, C., Balmes, J., Jenkins, B. M., and Kleinman, M. (2003). The effect of smoke from burning vegetative residues on airway inflammation and pulmonary function in healthy, asthmatic, and allergic individuals. *Final report to the California Air Resources Board and the California Environmental Protection Agency*.

Sorensen, C. (2011). The mobility of fractal aggregates: a review. *Aerosol Science and Technology*, 45(7):765–779.

Stephens, M., Turner, N., and Sandberg, J. (2003). Particle identification by laser-induced incandescence in a solid-state laser cavity. *Appl. Opt.*, 42(19):3726–3736.

Stolzenburg, M. R. and McMurry, P. H. (2008). Equations Governing Single and

Tandem DMA Configurations and a New Lognormal Approximation to the Transfer Function. *Aerosol Science and Technology*, 42(6):421–432.

Symonds, J. P. R., Reavell, K. S. J., Olfert, J. S., Campbell, B. W., and Swift, S. J. (2007). Diesel soot mass calculation in real-time with a differential mobility spectrometer. *Journal of Aerosol Science*, 38(1):52–68.

Tikhonov, A. N., Goncharsky, A. V., Stepanov, V. V., and Yagola, A. G. (1995). *Numerical methods for the solution of ill-posed problems*, volume 328. Springer Science & Business Media.

Twomey, S. (1975). Comparison of constrained linear inversion and an iterative nonlinear algorithm applied to the indirect estimation of particle size distributions. *Journal of Computational Physics*, 18(2):188 – 200.

Wahba, G. (1977). Practical approximate solutions to linear operator equations when the data are noisy. *SIAM Journal on Numerical Analysis*, 14(4):651–667.

Wang, S. C. and Flagan, R. C. (1990). Scanning electrical mobility spectrometer. *Aerosol Science and Technology*, 13(2):230–240.

Wiedensohler, A. (1988). An approximation of the bipolar charge distribution for particles in the submicron size range. *Journal of Aerosol Science*, 19(3):387 – 389.

World Health Organization (2012). *Health effects of black carbon*. WHO.

Young, H. D. and Freedman, R. A. (2008). *University Physics: with modern physics*. Pearson: San Fancisco.

Zhang, J. and Chen, D. (2014). Differential Mobility Particle Sizers for Nanoparticle Characterization. *Journal of Nanotechnology in Engineering and Medicine*, 5(2):20801.

Appendix A

Chapter 2 Supplemental Information

A.1 SP2 calibration

A.1.1 Counting efficiency of the SP2

The actual number concentration of rBC particles will be lower than the number concentration measured by the SP2; known as the counting efficiency, η_{SP2}. The SP2 counting efficiency will decrease for lower-mass rBC particles with mass near the lower end of the SP2's range. The relationship between rBC mass and efficiency depends on a number of variables such as: laser power, laser and particle beam alignment, particle morphology, ambient pressure, or coating thickness (Laborde et al., 2012). Counting efficiency was determined by comparing the total number concentration measured by the SP2 to a CPC, defined as,

$$\eta_{\mathrm{SP2}} = \frac{N_{\mathrm{SP2}}}{N_{\mathrm{CPC}}}, \tag{A.1}$$

where N_{SP2} is the number concentration measured by the SP2, and N_{CPC} is the number concentration measured by the CPC—for the size range measured by the SP2, the CPC counting efficiency is close to 100%. The SP2 counting efficiency was determined for uncoated rBC particles as a function of CPMA setpoint for the expected range of setpoints used during smog chamber experiments. The experimental setup is

shown in Figure A.1, and is similar to that shown in the main paper. The difference is the smog chamber is not used. Bare, uncoated particles were produced as described in the main paper. Then, the CPMA reduced the poly-disperse aerosol into a mono-disperse aerosol (of single mass-to-charge ratio). The mono-disperse aerosol number concentration was measured by the CPC and SP2 connected in parallel. The flow rates of the CPC and SP2 were 1.0 L min^{-1} and 0.12 L min^{-1} respectively, therefore the flow through the CPMA was 1.12 L min^{-1}.

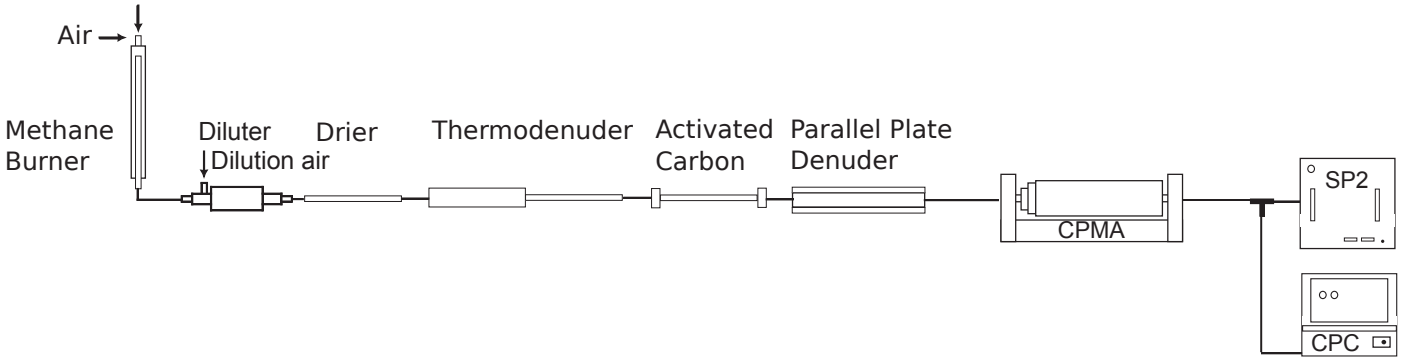

Figure A.1: Experimental set-up

When the uncoated particle counting efficiency is plotted versus CPMA setpoint as seen in Figure A.2, it is clear the counting efficiency is less than unity for CPMA setpoints below 0.9 fg. The decrease in counting efficiency is rapid. Consequently this efficiency loss means data below approximately 0.9 fg is unrepresentative of the actual mass and number concentration. As shown by Liu et al. (2017), when the laser is adjusted, nearly 100% efficiency can be observed down to 0.3 fg, and maintain greater than 80% efficiency down to approximately 0.1 fg. Throughout this paper data has not been shown below 0.9 fg due to this effect although data was gathered below that point. An unexpected result is for CPMA setpoints greater than about 1 fg, the calculated efficiency can be over 100%, indicating the SP2 was counting more particles than the CPC. This may be due to poor flow calibration in the SP2 or CPC, and/or possible co-incidence errors. Since the purpose of this paper is to only

demonstrate the CPMA-SP2 inversion it is inconsequential the SP2 was apparently over-counting above 1 fg. The particle concentrations may be systematically 20% higher that the actually concentrations but this only scales the amplitude of the two-variable distribution and does not fundamentally affect demonstration of the inversion. In the future, by comparing the CPC and SP2 the effective range of the SP2 could be extended below 0.9 fg by optimizing the laser power and alignment, and would be required if quantitative data is required at lower particle masses. Since the purpose of this paper is to prove the inversion, absolute data is not needed. Additionally, the range could be further extended by interpolating the efficiency curve and incorporating the efficiency factor into a mass-dependant correction factor (*e.g.* $\epsilon(m_{\mathrm{p}})$).

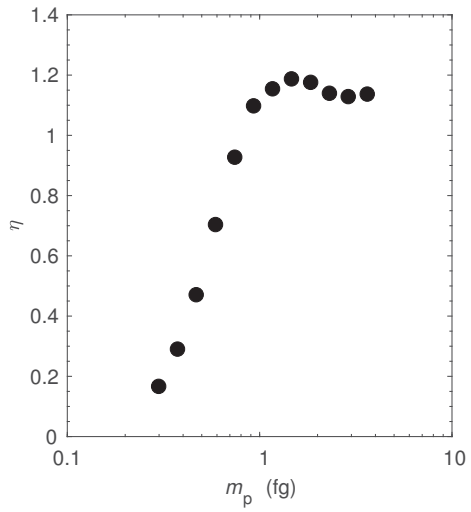

Figure A.2: Comparison of number concentration measured by the CPC and SP2 for given CPMA setpoints

A.1.2 Mass Calibration of SP2

The SP2 was calibrated to correlate rBC particle mass to incandescence peak height before each day of experiments using bare, uncoated rBC particles. Refractory BC particles were produced from a methane burner and conditioned to remove secondary organic aerosol coatings using methods described previously. A mass was selected on the CPMA, and uncoated, bare rBC particles were sampled using the CPMA-SP2. Thirteen mass setpoints were selected using the CPMA and the peak heights were calibrated to mass using PSI SP2 toolkit version 4.100a. All peak height fits were double-checked visually for accuracy. An example of the calibration curve developed each day for the broadband high gain (BBHG) and broadband low gain (BBLG) calibration curves are seen in Figure A.8a and A.8b respectively. The particle mass is a linear function of incandescence peak height as expected, and the PSI SP2 Toolkit fits a spline to the calibration curve.

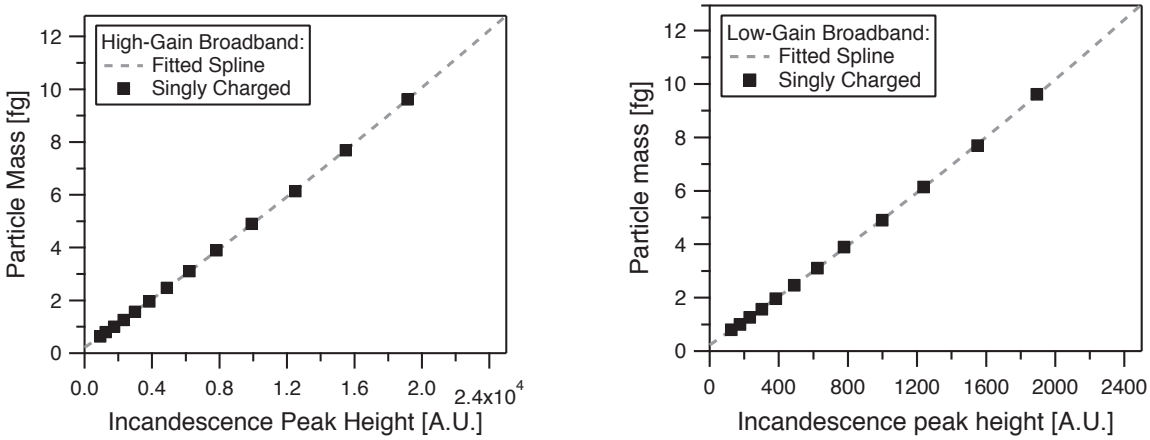

Figure A.3: a) Broad band high gain as a function of rBC mass b) Broad band low gain as a function of rBC mass

A.2 Solving for the two variable distribution

A.2.1 Overview

Solving for the two variable distribution involves the following steps i) calculating an initial guess ii) smoothing the initial guess iii) solving the equation using a Twomey deconvolution scheme iv) smoothing the final solution after all iterations are completed. An overview is provided in Figure A.4.

A.2.2 Initial Guess

Before executing the Twomey solver, an initial guess for the two variable distribution $\frac{\partial^2 N}{\partial \log m_{\mathrm{p}} \partial \log m_{\mathrm{rBC}}}$ is calculated. The calculation is analogous to the exact solution of number distribution with a CPMA transfer function as seen in section A.3.1 only extended to two variables. The response of the CPMA-SP2 system is divided by $\hat{\beta}$, and charge fraction assuming a charge state of one. The variable $\hat{\beta}$ is the analytical solution to the integral of the triangular CPMA transfer function assuming a single charge state, and is described in Section A.3.1. This gives an estimate of the shape of the two variable distribution $\frac{\partial^2 N}{\partial \log m_{\mathrm{p}} \partial \log m_{\mathrm{rBC}}}$, however the amplitude of this distribution is incorrect due to the existence of multiply charged particles. The initial guess contains some particles which exist in bins where mass of rBC is greater than total particle mass, an obvious impossibility. Therefore the concentration in these bins was set to zero. The removal of particles and improper amplitude of the initial guess is adjusted for later in the Twomey solver. The initial guess is calculated using,

$$\left.\frac{\partial^2 N_{\mathrm{guess}}}{\partial \log m_{\mathrm{p}} \partial \log m_{\mathrm{rBC}}}\right|_i = \frac{\left.\frac{\mathrm{d}N_{\mathrm{Response}}}{\mathrm{d}\log m_{\mathrm{rBC}}}\right|_i}{\bar{f}(m_{\mathrm{p},i}, \Phi = 1)\hat{\beta}}, \tag{A.2}$$

where $\left.\frac{\partial^2 N_{\mathrm{guess}}}{\partial \log m_{\mathrm{p}} \partial \log m_{\mathrm{rBC}}}\right|_i$ is the guess for the two variable distribution at the i$^{\mathrm{th}}$

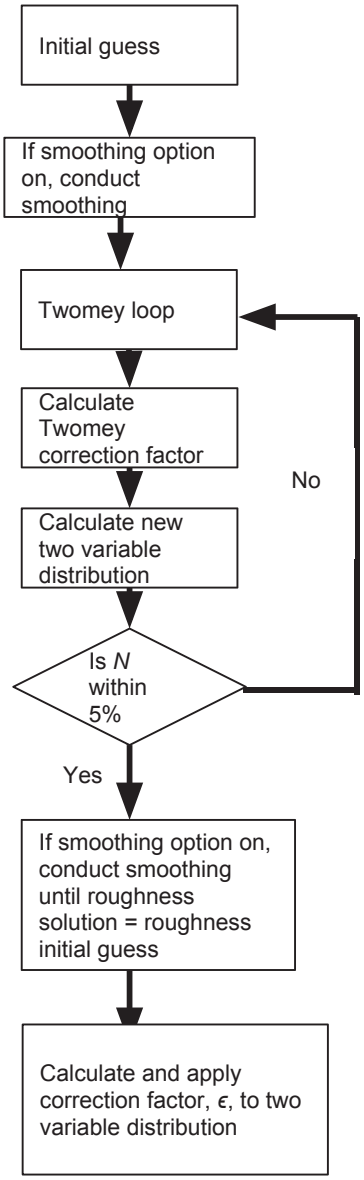

Figure A.4: Graphical representation of the Twomey method

CPMA setpoint, $\frac{\mathrm{d}N_{\mathrm{Response}}}{\mathrm{d}\log m_{\mathrm{rBC}}}$ is the number distribution of the CPMA-SP2 system response at the i$^{\mathrm{th}}$ CPMA setpoint, and $f(m_{\mathrm{p}}, \Phi = 1)$ is the charge fraction at the CPMA setpoint assuming one charge state.

A.2.3 Twomey method

Solving for the two variable distribution was accomplished with a Twomey algorithm. The Twomey algorithm was originally described by Twomey (1975). The method was modified in this paper to solve for a two variable distribution, and is similar to methods described in Rawat et al. (2016). The system of equations for solving the two variable distribution is defined as,

$$\mathbf{R} = \mathbf{Q}\boldsymbol{\Gamma}, \tag{A.3}$$

where $\mathbf{Q}$ is the two variable distribution $\frac{\partial^2 N}{\partial \log m_{\mathrm{p}} \partial \log m_{\mathrm{rBC}}}$, Γ is the Kernel function defined in Equation 6 of the main paper, and $\mathbf{R}$ is the number distribution of the instrument response measured by the SP2, $\frac{\mathrm{d}N_{\mathrm{Response}}}{\mathrm{d}\log m_{\mathrm{rBC}}}$. Using the initial guess the Twomey loop can begin. Firstly, a new instrument response is calculated based on the k^{th} guess for $\frac{\partial^2 N}{\partial \log m_{\mathrm{p}} \partial \log m_{\mathrm{rBC}}}$,

$$\left.\frac{\mathrm{d}N}{\mathrm{d}\log m_{\mathrm{rBC}}}\right|_k = \left.\frac{\partial^2 N}{\partial \log m_{\mathrm{p}} \partial \log m_{\mathrm{rBC}}}\right|_k \Gamma. \tag{A.4}$$

The ratio between the new instrument response and the measured instrument response is calculated by dividing element wise,

$$a_{i,j,k} = \frac{\left.\frac{\mathrm{d}N}{\mathrm{d}\log m_{\mathrm{rBC}}}\right|_{i,j,k}}{\left.\frac{\mathrm{d}N}{\mathrm{d}\log m_{\mathrm{rBC}}}\right|_{i,j,\mathrm{measured}}}. \tag{A.5}$$

A new correction factor is then calculated which will multiply $\left.\frac{\partial^2 N}{\partial \log m_{\mathrm{p}} \partial \log m_{\mathrm{rBC}}}\right|_k$ in order to calculate a new guess $\left.\frac{\partial^2 N}{\partial \log m_{\mathrm{p}} \partial \log m_{\mathrm{rBC}}}\right|_{k+1}$. The correction factor involves matrix multiplying the ratio of instrument responses less one by the kernel function and then adding one,

$$C_k = \left[1 + (a_k - 1)\Gamma\right] \tag{A.6}$$

Then the new guess is calculated by multiplying the correction factor by the old guess for the two variable distribution element-wise,

$$\left.\frac{\partial^2 N}{\partial \log m_{\mathrm{p}} \partial \log m_{\mathrm{rBC}}}\right|_{i,j,k+1} = C_{i,j,k} \left.\frac{\partial^2 N}{\partial \log m_{\mathrm{p}} \partial \log m_{\mathrm{rBC}}}\right|_{i,j,k} \tag{A.7}$$

The Twomey iteration continually compares the number concentration of the newest iteration of the two variable distribution to that measured by the SP2. The Twomey loop stops when the new two variable distribution is within 5%. The Twomey solver converges slowly so in the interest of efficiency a value an error or 5% was chosen. The loop also exits if roughness increases, or over 100 iterations are reached. Roughness is determined by taking the absolute value of the average roughness of the two variable distribution, where the second derivative derivative is calculated using finite difference methods. The second derivative was calculated using a fourth order central differencing and around the edges of the two variable distribution, right and left handed second order differencing was used. The two variable distribution was interpolated for calculation of the second derivative because finite difference schemes require a constant spacing, Δx. The fourth order central difference scheme was calculated using,

$$\left.\frac{\partial^2 u}{\partial x^2}\right|_{i,j} = \frac{-u_{i-2,j} + 16u_{i-1,j} - 30u_{i,j} + 16u_{i+1,j} - u_{i+2,j}}{12(\Delta x)^2} + O(\Delta x)^4 \tag{A.8}$$

$$\left.\frac{\partial^2 u}{\partial y^2}\right|_{i,j} = \frac{-u_{i,j-2} + 16u_{i,j-1} - 30u_{i,j} + 16u_{i,j+1} - u_{i,j+2}}{12(\Delta y)^2} + O(\Delta y)^4. \tag{A.9}$$

Along the edges second order forward or backward difference formulas were used, with backward difference being calculated using,

$$\left.\frac{\partial^2 u}{\partial x^2}\right|_{i,j} = \frac{2u_{i,j} - 5u_{i-1,j} + 4u_{i-2,j} - u_{i-3,j}}{12(\Delta x)^2} + O(\Delta x)^2 \tag{A.10}$$

$$\left.\frac{\partial^2 u}{\partial y^2}\right|_{i,j} = \frac{2u_{i,j} - 5u_{i,j-1} + 4u_{i,j-2} - u_{i,j-3}}{12(\Delta y)^2} + O(\Delta y)^2, \tag{A.11}$$

and forward difference calculated using,

$$\left.\frac{\partial^2 u}{\partial x^2}\right|_{i,j} = \frac{2u_{i,j} - 5u_{i+1,j} + 4u_{i+2,j} - u_{i+3,j}}{12(\Delta x)^2} + O(\Delta x)^2 \tag{A.12}$$

$$\left.\frac{\partial^2 u}{\partial y^2}\right|_{i,j} = \frac{2u_{i,j} - 5u_{i,j+1} + 4u_{i,j+2} - u_{i,j+3}}{12(\Delta y)^2} + O(\Delta y)^2. \tag{A.13}$$

A.2.4 Smoothing algorithm

Solving a system of equations using the Twomey algorithm induces oscillations in the solution to the two variable distribution. Additionally, distributions with low rBC particle concentrations may require smoothing. The oscillations can be reduced by Markowski smoothing (Markowski, 1987). Markowski smoothing involves using a moving average to reduce the amplitude of the oscillations, and is typically used in solutions for one variable number distributions (*e.g.* DMA or impactor inversions). Markowski smoothing was modified in order to smooth a two variable distribution, and has previously been demonstrated by Rawat et al. (2016). Smoothing was applied to both the initial guess and the final solution of $\frac{\partial^2 N}{\partial \log m_{\mathrm{p}} \partial \log m_{\mathrm{rBC}}}$. The algorithm was designed to preserve number concentration and preserve the non-real bins (i.e. where $m_{\mathrm{rBC}} > m_{\mathrm{p}}$) at a value of zero.

The algorithm works by taking the i^{th} and j^{th} point and calculating the smoothed

value by averaging the values of α neighbours. For each point in the local smoothing region, H, which is defined by the number of neighbours to the smoothed point, smoothing weights are assigned according to a Gaussian distribution. For points in the local smoothing region that exists in bins where $m_{\mathrm{rBC}} > m_{\mathrm{p}}$ the weighting factor was assigned to be zero, the same with points outside the domain of the two variable distribution. Since some points were forced to zero, the weighting matrix was normalized by its sum in order to preserve total number concentration of the two variable distribution. The local smoothing matrix calculated using Gaussian weights can be represented as,

$$L(v,l) = \frac{\exp\left(-\frac{v^2+l^2}{2\sigma^2}\right)}{2\pi\sigma^2} \frac{1}{\sum_{v=1}^{\alpha}\sum_{l=1}^{\alpha} L(v,l)}, \tag{A.14}$$

where $L(v,l)$ is the smoothing coefficient of the value in the local smoothing region, v and l are the distance of each point to the point to be smoothed (i.e. point i,j), and σ is the standard deviation of the Gaussian distribution. The standard deviation was chosen to be 0.6, an arbitrary decision which provided good results. Next, the matrix of smoothing values then multiplies the local region on the two variable distribution to be smoothed, and the smoothed point in the two variable distribution is calculated by summing the values of the smoothing region,

$$\frac{\partial^2 N}{\partial \log m_{\mathrm{p}} \partial \log m_{\mathrm{rBC}}}_{i,j} = \sum_{v=1}^{v_{\max}} \sum_{l=1}^{l_{\max}} LH. \tag{A.15}$$

It was found only selecting one point around each bin to be smoothed (*i.e.* $\alpha = 1$) provided the most sensible results, when $\alpha > 1$ the distribution became overly broad. This smoothing method was compared to median averaging and Wiener filter methods. This method was found to be superior because the median averaging and Wiener methods were found to broaden the two variable distribution unrealistically and did

not preserve total number distribution. The decision to assign weighting according to a Gaussian distribution was arbitrary, in Markowski (1987) and Rawat et al. (2016) the weights were constant. An advantage of assigning a Gaussian distribution is the distance between bins is accounted for.

Smoothing was conducted on the initial guess and after solving with a Twomey loop. The initial guess was smoothed for 10 iterations, and the final solution smoothed until roughness either increased or 10 iterations was reached. The roughness of the two variable solution was determined in the m_{p} and m_{rBC} directions using finite difference methods as described previously.

A.2.5 Correction factor

The final step of the algorithm is to apply the correction factor, $\bar{\epsilon}$, to the two variable distribution. A brief description was provided in the main paper, and the full equation to calculate the correction factor is described by,

$$\bar{\epsilon} = \frac{N_{\mathrm{SP2}}}{N} = \frac{\int_{m_{\min}}^{m_{\max}} \frac{\mathrm{d}N}{\mathrm{d}\log m_{\mathrm{rBC\,SP2}}} \mathrm{d}\log m_{\mathrm{rBC}}}{\int_{m_{\min}}^{m_{\max}} \int_{m_{\min}}^{m_{\max}} \frac{\partial^2 N}{\partial \log m_{\mathrm{p}} \partial \log m_{\mathrm{rBC}}} \partial \log m_{\mathrm{rBC}} \partial \log m_{\mathrm{p}}}, \tag{A.16}$$

where N is the total number concentration of the two-variable distribution and N_{SP2} is the number concentration of particles through direct SP2 measurement (*i.e.* no CPMA upstream of the SP2) over the same m_{rBC} range as the two-variable distribution. The variable $\int_0^{\infty} \frac{\mathrm{d}N}{\mathrm{d}\log m_{\mathrm{rBC\,SP2}}} \mathrm{d}\log m_{\mathrm{rBC}}$ is the number concentration distribution from direct SP2 measurement integrated over the range of CPMA setpoints, from the lowest setpoint, $m_{\min}$ to the highest, $m_{\max}$. This assumes the CPMA scan range is high enough to cover the vast majority of total particle masses.

A.3 Model Validation

Several methods of model validation are explored: i) comparing an analytically model to the CPMA-SP2 inversion assuming a single charge state and triangular transfer function, ii) comparing the mass and number concentration distributions from corrected, uncorrected, and direct SP2 measurement data, and iii) comparing total number concentration of the two variable distribution and direct SP2 measurement.

A.3.1 Comparison to analytical solution of $\frac{\mathrm{d}N}{\mathrm{d}\log m_{\mathrm{rBC}}}$ for a CPMA-SP2 system assuming single charging only

Recovery of a number distribution for a DMA using an analytical model has been previously described (Stolzenburg and McMurry, 2008). Using a similar method an analytical solution to the number distribution can be calculated for a triangular CPMA transfer function. The analytical solution should be equal to the solution using the numerical CPMA-SP2 inversion assuming a maximum charge state of 1 ($\Phi = 1$) and a triangular transfer function. Variables are defined as follows: β is the inverse of the CPMA resolution in mass space; f^* is the charge fraction evaluated at the set point and a charge state of 1; and variables with a * indicate they are evaluated at the CPMA set point (*e.g.* m_{p}^* is the mass setpoint of the CPMA, compared to m_{p} which is particle mass). CPMA resolution is the full width half maximum of the triangular transfer function.

When the CPMA is held at one mass setpoint, the number concentration of rBC particles measured by the SP2 is,

$$N^* = \int \mathrm{d}N^* = \sum_{\Phi=1}^{\Phi} \int \epsilon(m_{\mathrm{p}}) f(m_{\mathrm{p}}, \Phi) \Omega(m_{\mathrm{p}}, m_{\mathrm{p}}^*, B, \Phi) \mathrm{d}N \tag{A.17}$$

where

$$\mathrm{d}N = \frac{\mathrm{d}N}{\mathrm{d}\ln m_\mathrm{p}}\mathrm{d}\ln m_\mathrm{p} = \frac{\mathrm{d}N}{\mathrm{d}\ln m_\mathrm{p}}\frac{\mathrm{d}m_\mathrm{p}}{m_\mathrm{p}}. \tag{A.18}$$

Assuming the efficiency, charge fractions, and distribution are constant over the range of the transfer function, and that the fraction of multiply-charged particles is zero, this can be simplified:

$$N^* = \epsilon^* f^* \left[\frac{\mathrm{d}N}{\mathrm{d}\ln m_\mathrm{p}}\right]^* \int \Omega(m_\mathrm{p}, m_\mathrm{p}^*, B, \Phi = 1)\frac{\mathrm{d}m_\mathrm{p}}{m_\mathrm{p}}. \tag{A.19}$$

With the assumptions of single charging, a unique relationship between size and mass, and the distribution is approximately uniform over the width of the transfer function, we can eliminate charge and size dependency and assume a triangular transfer function in mass space:

$$\Omega(m_\mathrm{p}^*, \beta, m_\mathrm{p}) = \begin{cases} \dfrac{m_\mathrm{p} - (1-\beta)m_\mathrm{p}^*}{\beta m_\mathrm{p}^*} & \text{if } (1-\beta)m_\mathrm{p}^* < m_\mathrm{p} < m_\mathrm{p}^*, \\ \dfrac{(1+\beta)m_\mathrm{p}^* - m_\mathrm{p}}{\beta m_\mathrm{p}^*} & \text{if } m_\mathrm{p}^* < m_\mathrm{p} < (1+\beta)m_\mathrm{p}^* \end{cases} \tag{A.20}$$

and $\Omega = 0$ elsewhere.

Then, defining $\tilde{m}_\mathrm{p} = \dfrac{m_\mathrm{p}}{m_\mathrm{p}^*}$, the integral can be evaluated,

$$\begin{aligned} \int \Omega\frac{\mathrm{d}m_\mathrm{p}}{m_\mathrm{p}} &= \int_{1-\beta}^{1} \frac{\tilde{m}_\mathrm{p} - (1-\beta)}{\beta}\frac{\mathrm{d}\tilde{m}_\mathrm{p}}{\tilde{m}_\mathrm{p}} + \int_{1}^{1+\beta} \frac{(1+\beta) - \tilde{m}_\mathrm{p}}{\beta}\frac{\mathrm{d}\tilde{m}_\mathrm{p}}{\tilde{m}_\mathrm{p}} \\ &= (1+\frac{1}{\beta})\ln(1+\beta) - (1-\frac{1}{\beta})\ln(1-\beta). \end{aligned} \tag{A.21}$$

This equation is valid for $\beta < 1$. For brevity define this integral as $\hat{\beta}$,

$$\int \Omega \, \mathrm{d} \ln m_\mathrm{p} = (1 + \frac{1}{\beta}) \ln(1 + \beta) - (1 - \frac{1}{\beta}) \ln(1 - \beta) = \hat{\beta}, \tag{A.22}$$

where $\hat{\beta} \approx \beta$ when $\beta << 1$.

Therefore,

$$N^* = \epsilon^* f^* \left[\frac{\mathrm{d}N}{\mathrm{d} \ln m_\mathrm{p}} \right]^* \hat{\beta} \tag{A.23}$$

$$\left[\frac{\mathrm{d}N}{\mathrm{d} \ln m_\mathrm{p}} \right]^* = \frac{N^*}{\epsilon^* f^* \hat{\beta}} \approx \frac{N^*}{\epsilon^* f^* \beta}. \tag{A.24}$$

This is analogous to Stolzenburgs' equation for the DMA. For high resolution, we get:

$$\left[\frac{\mathrm{d}N}{\mathrm{d} \ln m_\mathrm{p}} \right] = \frac{N^*}{\epsilon^* f^* \beta} \approx \frac{R_m N^*}{\epsilon^* f^*}, \tag{A.25}$$

where $R_\mathrm{m} = \dfrac{1}{\beta}$. This shows the distribution over the natural logarithm of mass is approximately equal to the number concentration measured at the set point, multiplied by the resolution. Conversion to logarithm with base of 10 is possible by conducting the same analysis above, but with logarithms with base of 10. Change of logarithm basis from base 10 to base e can be conducted using,

$$\left[\frac{\mathrm{d}N}{\mathrm{d} \log m_\mathrm{p}} \right]^* \frac{1}{\ln 10} = \left[\frac{\mathrm{d}N}{\mathrm{d} \ln m_\mathrm{p}} \right]^*. \tag{A.26}$$

Now that an exact solution to a triangular CPMA transfer function has been developed, it can be compared to the CPMA-SP2 inversion method used in this paper. The inversion as described in the main text will be equivalent to the exact solution of a triangular CPMA transfer function when $\Phi_\mathrm{max} = 1$ and Ω is the triangular CPMA transfer function. Particle losses must be ignored for equivalency (*i.e.* $\bar{\epsilon}$ is ignored). Additionally, the impossible particles are not removed, as is usually done in the inversion. This is because such particles are also not removed in the analytic

model, giving a fair comparison between the analytic and numeric models. As seen in Figure A.5, plotting the analytic and numeric solutions show that they are equivalent for this simple case as expected. The figure shows solutions using uncoated rBC particles, with $C = 0.069$ kg m$^{-2.49}$ and $D_{\mathrm{m}} = 2.49$, and 10 iterations of the Twomey loop were executed before stopping. The Twomey loop was stopped because the total number concentration of the solution approached the total number concentration of the raw CPMA-SP2 measurement. No smoothing was conducted.

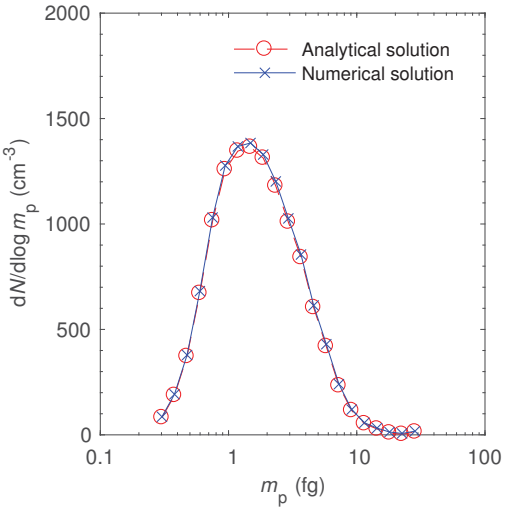

Figure A.5: Using simplified conditions, a comparison of the inversion against an exact solution to $\dfrac{\mathrm{d}N}{\mathrm{d}\log m_{\mathrm{p}}}$ shows they give approximately equal results

A.3.2 One variable number and mass distributions from corrected, uncorrected, and direct SP2 measurement data

As described in the main paper, $\bar{\epsilon}$, is calculated to correct the two variable distribution for assumption of particle mobility and particle losses. As seen in Figure A.6, the effect of correction can be visualized by viewing the number concentration distribution, $\dfrac{\mathrm{d}N}{\mathrm{d}\log m_{\mathrm{rBC}}}$ for the direct SP2 measurement scan, along with uncorrected and corrected distributions. The direct SP2 measurement refers to when the CPMA

was bypassed, and the uncorrected distribution refers to the results of the inversion of the CPMA-SP2 data. The corrected distribution refers to after applying the correction factor $\bar{\epsilon}$ to the distribution. The amplitude of the corrected distribution is similar to that of direct SP2 measurement, indicating the losses in the CPMA and the assumptions of particle density and morphology have been corrected for. In this work, a single constant was used to correct the distribution, and as shown in the figure the corrected distribution is slightly higher or lower than the SP2 distribution depending on the rBC particle mass. More sophisticated correction schemes could be used (*i.e.* a rBC mass-dependent correction function) to exactly match the distributions; however, the single correction factor was deemed reasonable.

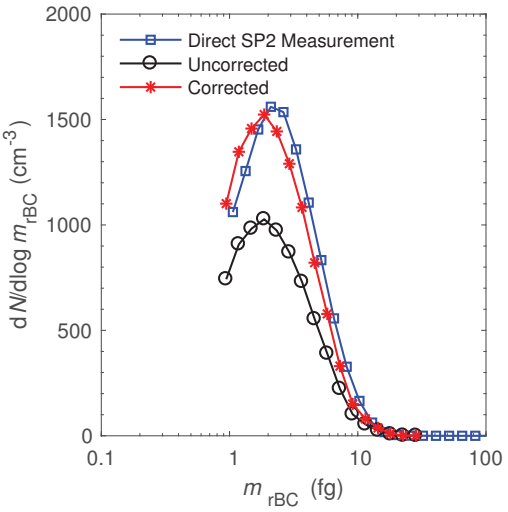

Figure A.6: Comparison of one variable distribution for direct SP2 measurement, uncorrected distribution, and corrected distribution

The direct SP2 measurement, along with uncorrected and corrected mass concentration distribution as a function of rBC mass for bare, uncoated rBC particles is shown in Figure A.6. The amplitude of the corrected two variable distribution is not equal to the amplitude of the distribution from direct SP2 measurement. However, it would be easy to use a correction factor based on total mass concentration instead of total number concentration, which would mean the total particle mass concentration

of direct SP2 measurement would match the total particle mass concentration of the corrected distribution.

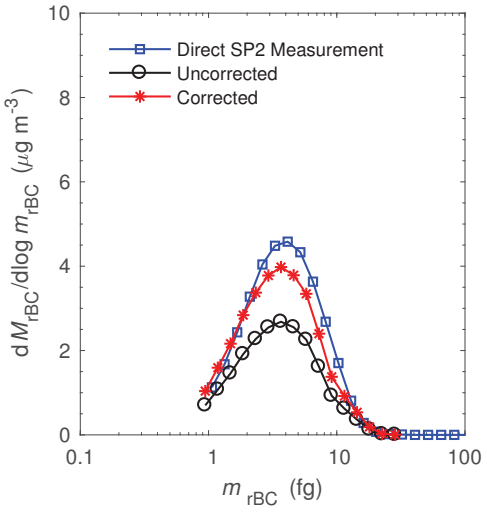

Figure A.7: Comparison of one variable distribution for a direct SP2 measurement scan, uncorrected distribution, and corrected distribution

A.3.3 Demonstration showing different mobility assumptions do not significantly change the final results of the inversion

An initial guess of mobility must be provided for the inversion. The sensitivity of the results to density assumptions were tested on data from the smog chamber where the particles were bare rBC. Two cases were studied, characterized by differing prefactors, C and mass-mobility exponent,D_{m}, for the mass-mobility relationship,

$$m = C d_{\mathrm{m}}^{D_{\mathrm{m}}}, \tag{A.27}$$

where d_{m} is mobility. The two limiting cases were studied namely i) assuming the particles had similar density to those emitted from combustion engines ($C = 0.069$ kg m$^{-2.49}$, $D_{\mathrm{m}} = 2.49$) (Graves et al., 2016) and ii) assuming particles had a heavy coating ($C = 733$ kg m^{-3}, $D_{\mathrm{m}} = 3.00$) (Schnitzler et al., 2014). Clearly assum-

ing heavily coated particles is incorrect since we are looking at uncoated particles, however testing using an obviously incorrect assumption of mobility can give confidence that correcting the distribution returns a reasonable result. The total number concentration and the single variable distributions can be determined for both cases.

Firstly, since the inversion is corrected on a number concentration basis, the total number concentration should be identical between the two cases. Double integration of the two variable distribution yields the total number concentration of the aerosol population containing rBC, calculated using,

$$N = \int_0^\infty \int_0^\infty \frac{\partial^2 N}{\partial \log m_{\mathrm{p}} \partial \log m_{\mathrm{rBC}}} \partial \log m_{\mathrm{rBC}} \partial \log m_{\mathrm{p}}. \tag{A.28}$$

As expected, there was negligible difference between the two examined cases; the total number concentration and rBC mass concentration changed less than 1% between the two cases.

Secondly, the shape of the one variable number and mass concentration distributions can be examined for both cases. Mobility change should only affect the amplitude of the distribution, therefore correcting the distribution should ensure both cases are approximately equal after correction. Figure A.8 shows the corrected and uncorrected number and mass concentration distributions for assuming two different mobilities compared to direct SP2 measurement. Even though the initial assumption of the mass-mobility relationship is different shown by different uncorrected distributions, the corrected number and mass distributions are identical. This shows the mobility assumption primarily affects amplitude of the two variable distribution, and not the width.

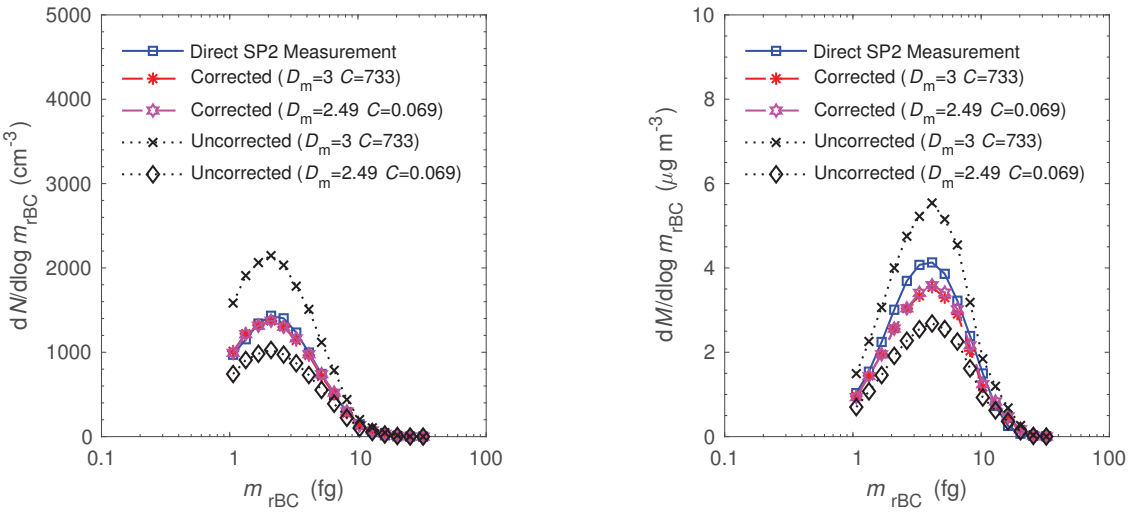

(a) (b)

Figure A.8: a) corrected and uncorrected number concentration distributions for assuming two different mobility's compared to direct SP2 measurement b) corrected and uncorrected mass concentration distributions for assuming two different mobility's compared to direct SP2 measurement

A.4 CPMA Transfer Function

A transfer function describes the proportion of particles of a certain mass which pass through the CPMA. There have been three models of the CPMA transfer function developed (Olfert and Collings, 2005; Olfert, 2005), namely the i) the triangular transfer function, ii) the non-diffusion transfer function, and iii) the diffusion transfer function. The triangular transfer function can be calculated analytically, while the other transfer functions require a numerical solution. In Figure A.9a each transfer function was compared, where the fraction of particles let through the classifier, Ω, is plotted as a function of mass. It is clear that the triangular transfer function differs significantly from the non-diffusion and diffusion transfer function. The diffusion transfer function is superior because it includes diffusion effects, and since it has approximately the same computational cost as the non-diffusion model, it was used in the inversion calculations (unless otherwise noted). As seen in Figure A.9b, when

solving for $\frac{\mathrm{d}N}{\mathrm{d}\log m_\mathrm{p}}$ using the three different transfer function models it is clear the triangular model under-counts relative to the non-diffusion and diffusion models. The under counting is apparent from the lower amplitude of the triangular transfer function compared to the diffusion and non-diffusion variants. This difference is relatively small, and would be corrected by $\bar{\epsilon}$ if the triangular transfer function was used in inversion calculations instead of the diffusion model.

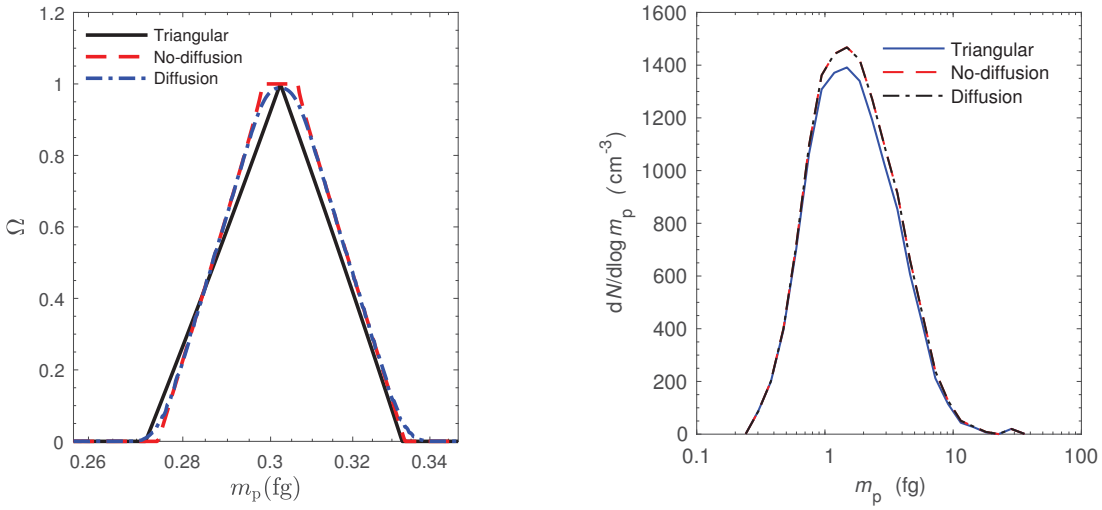

Figure A.9: a) The difference in transfer function models are shown for a setpoint of 0.33 fg, assuming a particle density of 0.069 kg m$^{-2.49}$ b) Comparison of solution to $\frac{\mathrm{d}N}{\mathrm{d}\log m_\mathrm{p}}$ using different transfer function models

A.5 Additional results

A.5.1 Number distribution

In the main paper the number distributions $\frac{\mathrm{d}N}{\mathrm{d}\log m_\mathrm{p}}$ and $\frac{\mathrm{d}N}{\mathrm{d}\log m_\mathrm{rBC}}$ for uncoated and coated particles were shown. The number distribution of a mixed coated and lightly coated population can also be recovered by integration of the two variable distribution. As seen in Figure A.10, the two populations can be clearly distinguished

when the dependent variable is total particle mass, as seen by this distribution having two peaks.

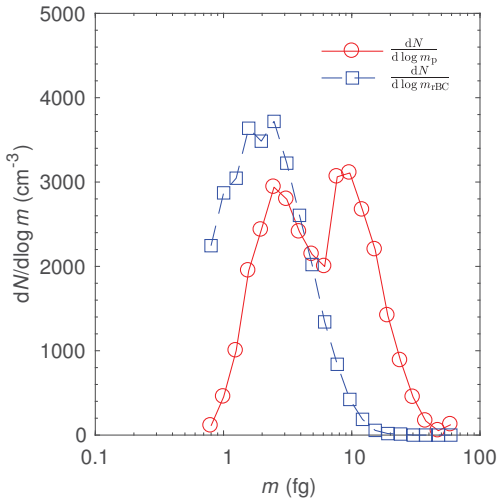

Figure A.10: Number distribution of a mixture of coated and uncoated particles

A.5.2 Mass distribution

One variable mass distribution can be plotted either as a function of rBC mass or total particle mass resulting in $\frac{\mathrm{d}M}{\mathrm{d}\log m_\mathrm{p}}$, $\frac{\mathrm{d}M_\mathrm{rBC}}{\mathrm{d}\log m_\mathrm{p}}$, $\frac{\mathrm{d}M}{\mathrm{d}\log m_\mathrm{rBC}}$, or $\frac{\mathrm{d}M_\mathrm{rBC}}{\mathrm{d}\log m_\mathrm{rBC}}$. Select distributions were plotted in the main paper for uncoated, coated, and mixed coated and lightly coated populations. Here more distributions are shown to demonstrate how the inversion can show the growth of coating on the bare rBC particles using one variable mass distributions evolving over a period of time. Figure A.11 shows mass distribution with the dependent variable being total mass, with sub-figure A.11a measured after 1 hour of lights on, and sub-figure A.11d occurring 6 hours after lights on. As time progresses and the coating thickness increases, the median of the distributions $\frac{\mathrm{d}M}{\mathrm{d}\log m_\mathrm{p}}$ and $\frac{\mathrm{d}M_\mathrm{rBC}}{\mathrm{d}\log m_\mathrm{p}}$ increase, reflecting the increased total mass of the population due to coating growth. Additionally the increase in coating thickness is shown by the increasing amplitude of $\frac{\mathrm{d}M}{\mathrm{d}\log m_\mathrm{p}}$ relative to $\frac{\mathrm{d}M_\mathrm{rBC}}{\mathrm{d}\log m_\mathrm{p}}$.

A similar representation of coating growth evolving over time can be shown for mass concentration distributions with the dependent variable as rBC mass as seen in figure A.12. Each figure shows $\frac{\mathrm{d}M}{\mathrm{d}\log m_\mathrm{rBC}}$, and $\frac{\mathrm{d}M_\mathrm{rBC}}{\mathrm{d}\log m_\mathrm{rBC}}$. The key difference from the previous representation is the median of the rBC mass distribution does not significantly change because rBC particles only acquire organic coating mass. However a similar relationship between the increasing amplitude of $\frac{\mathrm{d}M}{\mathrm{d}\log m_\mathrm{rBC}}$ relative to $\frac{\mathrm{d}M_\mathrm{rBC}}{\mathrm{d}\log m_\mathrm{rBC}}$ is observed reflecting the increase of coating mass.

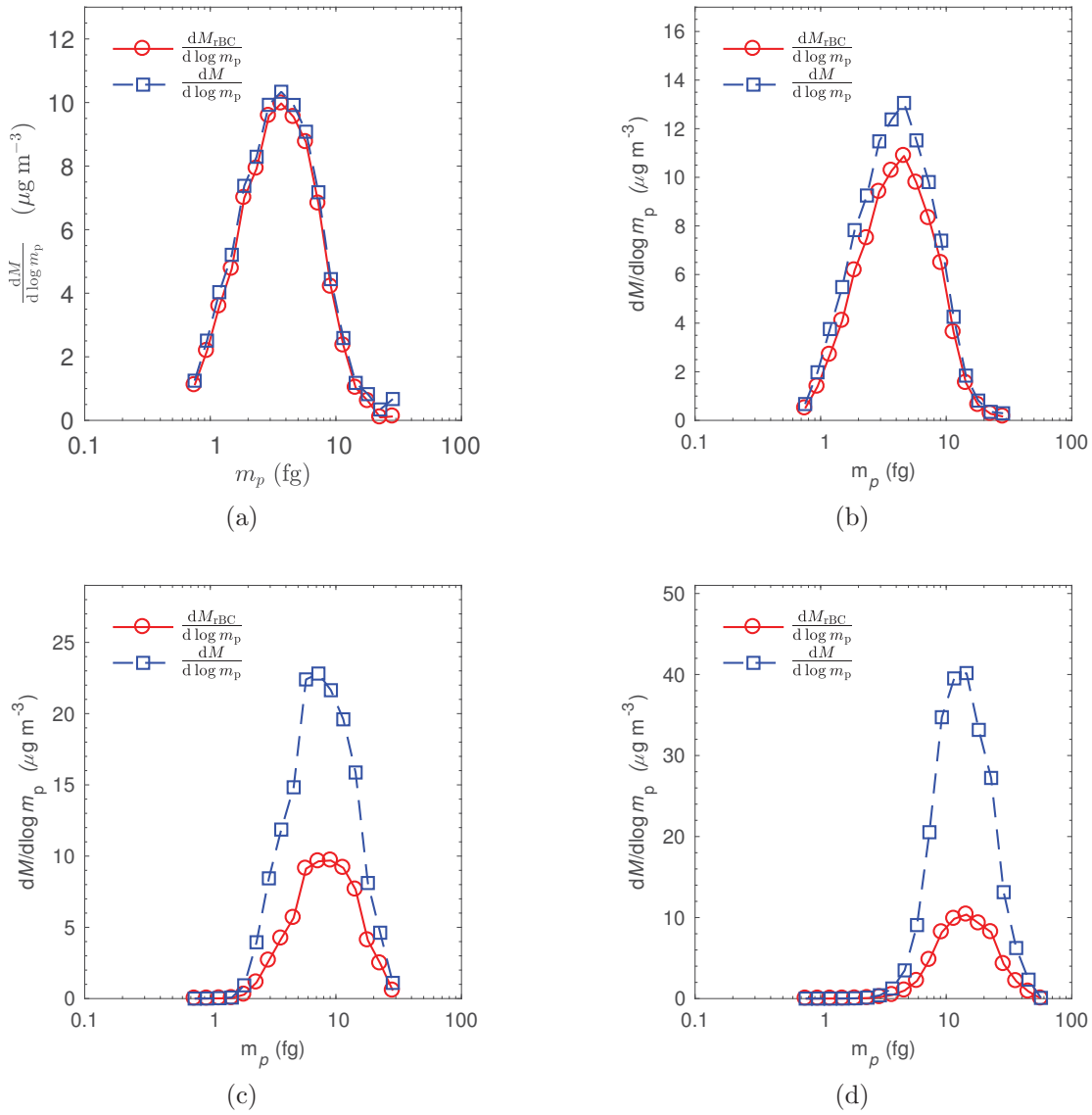

Figure A.11: $\frac{\mathrm{d}M}{\mathrm{d}\log m_\mathrm{p}}$ and $\frac{\mathrm{d}M_\mathrm{rBC}}{\mathrm{d}\log m_\mathrm{p}}$ for CPMA-SP2 scans with start times after turning on UV lights of a) 1.3 hours b) 2.2 hours c) 4.6 hours and d) 6.8 hours.As time progresses the coating mass increase is reflected in the increase of median total mass and increase of amplitude of $\frac{\mathrm{d}M}{\mathrm{d}\log m_\mathrm{p}}$ relative to $\frac{\mathrm{d}M_\mathrm{rBC}}{\mathrm{d}\log m_\mathrm{p}}$

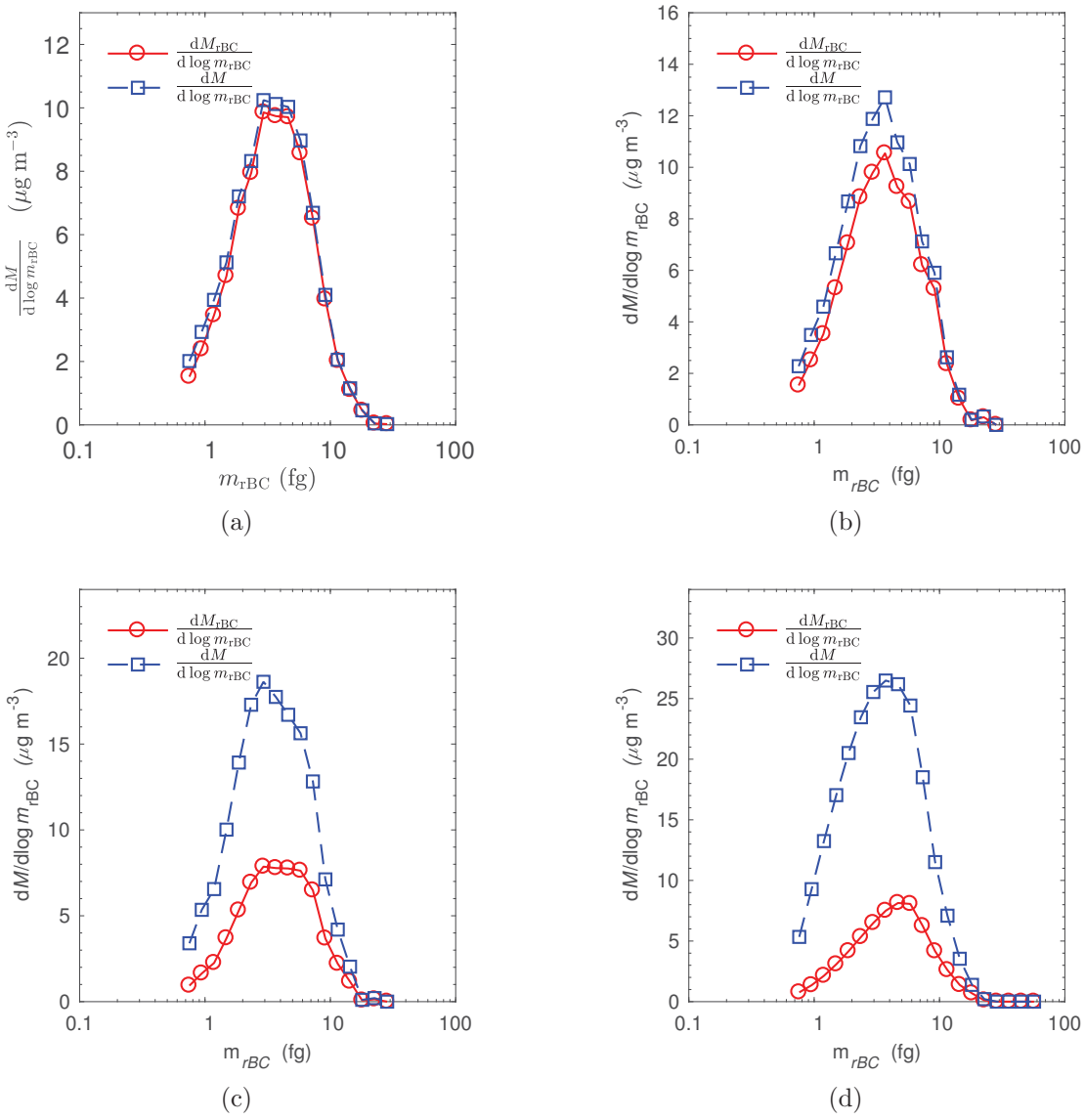

Figure A.12: $\frac{\mathrm{d}M}{\mathrm{d}\log m_{\mathrm{rBC}}}$ and $\frac{\mathrm{d}M_{\mathrm{rBC}}}{\mathrm{d}\log m_{\mathrm{rBC}}}$ for CPMA-SP2 scans with start times after turning on UV lights of a) 1.3 hours b) 2.2 hours c) 4.6 hours and d) 6.8 hours. As time progresses the coating mass increase is reflected in the increase of median total mass and increase of amplitude of $\frac{\mathrm{d}M}{\mathrm{d}\log m_{\mathrm{rBC}}}$ relative to $\frac{\mathrm{d}M_{\mathrm{rBC}}}{\mathrm{d}\log m_{\mathrm{rBC}}}$

References

Graves, B. M., Koch, C. R., and Olfert, J. S. (2016). Morphology and Volatility of Particulate Matter Emitted from a Gasoline Direct Injection Engine Fuelled on Gasoline and Ethanol Blends . *Journal of Aerosol Science*, pages –.

Laborde, M., Schnaiter, M., Linke, C., Saathoff, H., Naumann, K.-H., Möhler, O., Berlenz, S., Wagner, U., Taylor, J. W., Liu, D., Flynn, M., Allan, J. D., Coe, H., Heimerl, K., Dahlkötter, F., Weinzierl, B., Wollny, A. G., Zanatta, M., Cozic, J., Laj, P., Hitzenberger, R., Schwarz, J. P., and Gysel, M. (2012). Single Particle Soot Photometer intercomparison at the AIDA chamber. *Atmospheric Measurement Techniques*, 5(12):3077–3097.

Liu, D., Whitehead, J., Alfarra, M. R., Reyes-Villegas, E., Spracklen, D. V., Reddington, C. L., Kong, S., Williams, P. I., Ting, Y.-C., Haslett, S., Taylor, J. W., Flynn, M. J., Morgan, W. T., McFiggans, G., Coe, H., and Allan, J. D. (2017). Black-carbon absorption enhancement in the atmosphere determined by particle mixing state. *Nature Geosci*, 10(3):184–188.

Markowski, G. R. (1987). Improving Twomey's algorithm for inversion of aerosol measurement data. *Aerosol science and technology*, 7(2):127–141.

Olfert, J. S. (2005). A Numerical Calculation of the Transfer Function of the Fluted Centrifugal Particle Mass Analyzer. *Aerosol Science and Technology*, 39(10):1002–1009.

Olfert, J. S. and Collings, N. (2005). New method for particle mass classificationthe Couette centrifugal particle mass analyzer . *Journal of Aerosol Science*, 36(11):1338 – 1352.

Rawat, V. K., Buckley, D. T., Kimoto, S., Lee, M. H., Fukushima, N., and Hogan, C. J. (2016). Two dimensional size-mass distribution function inversion from differential mobility analyzer-aerosol particle mass analyzer (DMA-APM) measurements. *Journal of Aerosol Science*, 92:70–82.

Schnitzler, E. G., Dutt, A., Charbonneau, A. M., Olfert, J. S., and Jäger, W. (2014). Soot aggregate restructuring due to coatings of secondary organic aerosol derived from aromatic precursors. *Environmental Science & Technology*, 48(24):14309 – 14316.

Stolzenburg, M. R. and McMurry, P. H. (2008). Equations Governing Single and Tandem DMA Configurations and a New Lognormal Approximation to the Transfer Function. *Aerosol Science and Technology*, 42(6):421–432.

Twomey, S. (1975). Comparison of constrained linear inversion and an iterative nonlinear algorithm applied to the indirect estimation of particle size distributions. *Journal of Computational Physics*, 18(2):188 – 200.